

# **STUDY OF SiC-BASED NEUTRON DETECTOR FOR APPLICATIONS IN THE HARSH ENVIRONMENT OF FAST REACTORS**

*By*

**SHIVANG TRIPATHI**

(Enrolment No. ENGG02201304012)

**Indira Gandhi Centre for Atomic Research, Kalpakkam**

*A thesis submitted to the  
Board of Studies in Engineering Sciences  
In partial fulfillment of requirements  
for the Degree of*

**DOCTOR OF PHILOSOPHY**

*of*

**HOMI BHABHA NATIONAL INSTITUTE**






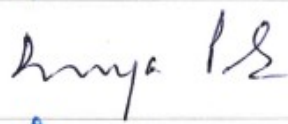


**May, 2019**



# Homi Bhabha National Institute

## Recommendations of the Viva Voce Committee

As members of the Viva Voce Committee, we certify that we have read the dissertation prepared by **Shivang Tripathi** entitled "**Study of SiC-based neutron detector for applications in the harsh environment of Fast Reactors**" and recommend that it may be accepted as fulfilling the thesis requirement for the award of Degree of Doctor of Philosophy.


Chairman - Dr. K. Velusamy		Date: 20/12/2019
Guide / Convener - Dr. K. Devan		Date: 20/12/2019
Examiner - Dr. Seema Sharma (IISER, Pune)		Date: 20/12/19
Member 1- Dr. B. K. Panigrahi		Date: 20/12/19
Member 2- Dr. Anish Kumar		Date: 20/12/2019
Technology Advisor- Shri. Nagaraj C.P.		Date: 20/12/2019

Final approval and acceptance of this thesis is contingent upon the candidate's submission of the final copies of the thesis to HBNI.

I/We hereby certify that I/we have read this thesis prepared under my/our direction and recommend that it may be accepted as fulfilling the thesis requirement.

Date: 20/12/19

Place: IGCAR, Kalpakkam


  
Dr. K. Devan  
(Guide)



## STATEMENT BY AUTHOR

This dissertation has been submitted in partial fulfillment of requirements for an advanced degree at Homi Bhabha National Institute (HBNI) and is deposited in the Library to be made available to borrowers under rules of the HBNI.

Brief quotations from this dissertation are allowable without special permission, provided that accurate acknowledgement of source is made. Requests for permission for extended quotation from or reproduction of this manuscript in whole or in part may be granted by the Competent Authority of HBNI when in his or her judgment the proposed use of the material is in the interests of scholarship. In all other instances, however, permission must be obtained from the author.

  
(Shivang Tripathi)



## DECLARATION

I, hereby declare that the investigation presented in the thesis has been carried out by me.

The work is original and has not been submitted earlier as a whole or in part for a degree / diploma at this or any other Institution / University.



(Shivang Tripathi)





## List of Publications arising from the thesis

### Journal

1. “The performance simulation of the LiH-SiC-based Fast Neutron Detector for harsh environment monitoring using Geant4 and TCAD”, **Shivang Tripathi**, C. Upadhyay, C.P. Nagaraj, A. Venkatesan, K. Devan, *Nucl. Instrum. Methods Phys. Res. A.*, **2019**, 916, 246–256.
2. “Effect of High energy electron and proton irradiation on the electrical characteristics of Ni/4H-SiC-based SBD”, **Shivang Tripathi**, Chandra Kant Upadhyay, C.P. Nagaraj, A. Venkatesan, K. Devan, *J. Instrum.*, **2019**, 14, P02002.
3. “Towards radiation hard converter material for SiC-based fast neutron detectors”, **Shivang Tripathi**, Chandra Kant Upadhyay, C.P. Nagaraj, A. Venkatesan, K. Devan, *J. Instrum.*, **2018**, 13, P05026.
4. “Investigation of enhancement in planar fast neutron detector efficiency with the stacked structure using Geant4”, **Shivang Tripathi**, Chandra Kant Upadhyay, C.P. Nagaraj, K. Devan, A. Venkatesan, K. Madhusoodanan, *Nucl. Sci. Tech.*, **2017**, 28, 154.

### Manuscript under preparation

1. “Survey of advancements in fast neutron detection”, **Shivang Tripathi**, C. Upadhyay, C.P. Nagaraj, A. Venkatesan and K. Devan.

### Book Chapter

1. “Investigation of Perylene as a Converter Material for Fast Neutron Detection and Spectroscopy Using GEANT4 Monte Carlo Simulations”, **Shivang Tripathi**, C. Upadhyay, C.P. Nagaraj, A. Venkatesan, K. Devan, K. Madhusoodanan, in: A. Konkani, R. Bera, S. Paul (Eds.), *Adv. Syst. Control Autom.*, Springer Singapore, **2018**: pp. 189–197.

## Conferences

1. “Effect of gamma-irradiation on the electrical characteristics of SiC-based FNDs”, **Shivang Tripathi**, C. Upadhyay, C.P. Nagaraj, A. Venkatesan, K. Devan, *HBNI RSM-MSENM-2018*, IGCAR, Kalpakkam, May 7-9, **2018** (*Oral presentation*).
2. “LiH-SiC-based Fast Neutron Detector for harsh environment”, **Shivang Tripathi**, C. Upadhyay, C. P. Nagaraj, K. Devan, A. Venkatesan, B. K. Panigrahi, *IARPIC-2018*, HBNI, BARC, Mumbai, Jan 16-20, **2018** (*Oral presentation*).
3. “TCAD assisted analysis of Silicon Carbide based Fast Neutron Detector for nuclear applications”, **Shivang Tripathi**, C. Upadhyay, C. P. Nagaraj, K. Devan, A. Venkatesan, B. K. Panigrahi, *12th IEEE NMDC*, Holiday Inn Atrium, Singapore, October 2-4, **2017** (*Oral presentation*).
4. “Geant4 simulations of semiconductor detectors (SiC) for fast neutron spectroscopy”, **Shivang Tripathi**, C. Upadhyay, C.P. Nagaraj, K. Devan, K. Madhusoodanan, S. A. V. Satya Murty, *INDICON, IEEE*, New Delhi, **2015** (*Poster presentation*).

  
(Shivang Tripathi)

*DEDICATED*

*TO*

*ALL THE NEUTRONS*



## ACKNOWLEDGEMENTS

I would like to express my sincere gratitude and appreciation to all those who have been with me during the pursuit of my research and helped me to successfully complete this thesis. First, I want to express my deepest thanks and appreciation to my parents for their never-ending supports and kindness. Neither this work, nor any success in my life could be achieved without their shine of wisdom and warmth of love.

I wish to express my best gratitude and thanks to my advisor, **Dr. K. Devan**, Head, Reactor Neutronics Division, Reactor Design Group, IGCAR for his persistent encouragement, everlasting patience, very caring nature and insightful guidance, which in all the ways led to the completion of my thesis. I am extremely grateful for having the privilege to work with him and learn from his expertise.

I sincerely thank my former technology adviser **Shri K. Madhusoodanan**, former group director, EIG, IGCAR and present technology adviser **Shri C.P. Nagaraj**, Head, Nuclear Instrumentation Section, EIG, IGCAR for valuable guidance and support in technical as well as in administrative issues.

I would like to acknowledge **Shri Chandrakant Upadhyay**, SO/E, EIG, IGCAR for his endless patience, detailed guidance and continued encouragement throughout the course of preparing for and conducting the research. The joy and enthusiasm he has for this research was contagious and motivational for me, even during tough times. It was a pleasure to talk with him about work and life.

I convey my heartiest appreciation to my Doctoral Committee (DC) chairman, **Dr. K. Velusamy**, DC members **Dr. S. Sivakumar**, **Dr. B. K. Panigrahi** and **Dr. Anish Kumar** for their valuable inputs, continuous monitoring of my progress and valuable support throughout the course of my research.

My sincere gratitude to, Dr. A.K. Bhaduri, Director, IGCAR and Dr. S.A.V. Satya Murty, and Dr. P.R. Vasudeva Rao, former Directors, IGCAR for providing excellent environment to carry out research work.

I sincerely thank Dr. B. K. Panigrahi, Director, EIG, Dr. M. Sai Baba, former Dean of students' affairs, Dr. Lakshmi Narasimhan, Dr. G. Sasikala, former Dean of Engineering Sciences, Dr. Anish Kumar, present Dean of Engineering Sciences for their care and support.

My special thanks to Shri. A.Venkatesan Head ICD, Shri. M. Manimaran Head PIS, Mrs. K. Kameshwari, Head FHCS, Mrs. Somavathi, Mrs. Varuna, Mrs. Nisha, Mr. Deendhayalan, Mr. Ananda Kumar, Mr. Pradeesh, Mr. Ankit, Mr. Subramanian, Mr. G.K. Mishra, Mr. RajKumar, Mr. Balasundaram and all members of ICD for their support and creating a homely environment at the work place during this period. I also thank Mr. Jehadeeshan, Mr. Sujith and Computer Division staff for HPC facilities.

I am grateful for the financial support provided by research fellowship scheme (JRF/SRF/ and partial financial support during extension) from Indira Gandhi Centre for Atomic Research, Department of Atomic Energy, Govt. of India, for the duration of the work. I thank HBNI for providing the international travel grant to attend the IEEE Nanotechnology Materials and Devices Conference (NMDC-2017), held in Singapore.

I endow my special gratitude to Dr. P. Vigneshwara, Post Doctoral Research at IIT-Madras for his kind help in the TCAD simulations. I specially acknowledge Mr. Manoj Kumar Parida, SRF, IGCAR for all the technical discussion related to GEANT4 simulations.

I endow my special gratitude to my Engineering Sciences batch-mates Dr. Vikas Kumar, Mr. Nidhin, Mr. Sriram and Dr. V. Sumathi for all the memories beginning from Training School till now.

It is my pleasure to thank all my friends and seniors Dr. Sravanthi. S, Dr. Chandan Bhagat, Dr. Sumathi. G, Dr. Prema. S, Dr. Santhosh, Dr. Varun Hassija, Dr. Nilakantha, Dr. Radhikesh, Dr. Irshad, Dr. Vairavel, Dr. Lakshmanan, Dr. Padmolochoan, Mr. Amit Kumar Mishra, Mr. Revanth, Mr. Sarvajith, Mr. Darpan, Mr. Abhishek, Mr. Balram and all enclavians including Cricket and Badminton team-mates for making my days at Kalpakkam very colorful.

I endow my special gratitude to Mr. Shashwat Swain and Mrs. Uma who were always available on the next door for anything. Their presence never let us feel that we are away from home.

It has been a great honor for me to work in IGCAR and to be surrounded with some of the brightest and loving people, I have met. To all, I say Thank you from the bottom of my heart.

I should also be very grateful to my sister Dr. Shambhavi and brother, Mr. Amar for their consistent support and understanding. A special mention for my wife, Shivangi, for her patience and presence whenever I needed.

  
(Shivang Tripathi)





# CONTENTS

<b>SYNOPSIS</b>	<b>i</b>
<b>LIST OF FIGURES</b>	<b>v</b>
<b>LIST OF TABLES</b>	<b>xi</b>
<b>LIST OF ABBREVIATIONS</b>	<b>xiii</b>
<b>CHAPTER 1: INTRODUCTION</b>	<b>1</b>
1.1 Preamble	1
1.2 Motivation	4
1.3 Silicon Carbide- Literature Survey	6
1.3.1 SiC: salient features and properties	6
1.3.2 SiC as a neutron detector	9
1.4 Objectives and Studies Performed	11
1.5 Organization of the thesis	13
<b>CHAPTER 2: BASICS OF NEUTRON DETECTION</b>	<b>15</b>
2.1 Preamble	15
2.2 Mechanisms of neutron interaction with matter	15
2.2.1 Scattering interaction	16
2.2.2 Absorption interaction	19
2.2.3 Neutron interaction cross-section	20
2.2.4 Charged particle interaction with matter	23
2.3 Types of neutron detectors	24
2.3.1 Gas-filled detectors	24
2.3.2 Scintillation detectors	25
2.3.3 Semiconductor Detectors	26
2.4 Metal-Semiconductor (M-S) Junction	31
2.4.1 Schottky contacts	31
2.4.2 Ohmic contacts	33
2.4.3 Current transport mechanism	34
2.4.4 Current-Voltage ( $I$ - $V$ ) relationship	35
2.4.5 Capacitance-Voltage ( $C$ - $V$ ) relationship	36
2.5 Defects in semiconductors	38
2.5.1 Primary Defects	38
2.5.2 Secondary defects	39
2.5.3 Defects in SiC	42
2.5.4 Effects of irradiation induced defects	43
2.6 Summary	44

<b>CHAPTER 3: MODELING TOOLS</b>	<b>45</b>
3.1 Preamble	45
3.2 Monte-Carlo (MC) Method	45
3.2.1 Monte-Carlo in Nuclear and Particle Physics	46
3.3 GEANT4 simulation toolkit	47
3.3.1 GEANT4 class categories	48
3.3.2 GEANT4 simulation flow for present work	51
3.3.3 System information where GEANT4 simulations were performed	55
3.4 Semiconductor device simulation using TCAD	56
3.4.1 Silvaco: TCAD simulation suite	56
3.4.2 Basic Semiconductor Equations	59
3.4.3 Models for SiC device description in TCAD	60
3.4.4 Irradiation-induced defect definition in TCAD	64
3.5 Summary	66
<b>CHAPTER 4: CONVERTER OPTIMIZATION AND EFFICIENCY ENHANCEMENT</b>	<b>67</b>
4.1 Preamble	67
4.2 Simulation Methodologies in GEANT4	68
4.2.1 Methodology for converter thickness optimization	68
4.2.2 Methodology for study of effect of background discrimination	70
4.2.3 Methodology for study of efficiency improvement	71
4.3 Benchmarking Simulations	72
4.3.1 Probability of Interaction for 1 MeV neutrons in HDPE	72
4.3.2 HDPE thickness optimization for <sup>239</sup> Pu-Be neutron source	74
4.3.3 HDPE thickness optimization for 2.5 MeV D-D neutron source	77
4.4 Simulation Results and Discussions	78
4.4.1 Nuclear reactions in Direct and Indirect conversion SiC-based detectors	79
4.4.2 HDPE as a converter (HDPE-SiC-based detector)	83
4.4.3 Study of other hydrogenous converters for harsh environments	90
4.4.4 LiH as a converter (LiH-SiC-based detector)	92
4.4.5 Comparison of Energy deposition in SiC through LiH & HDPE	99
4.4.6 Perylene as a converter (perylene-SiC-based detector)	102
4.4.7 Dependence of Efficiency on source distribution	104
4.5 Summary	107

<b>CHAPTER 5: EFFECT OF DEEP LEVELS ON THE CHARACTERISTICS OF SiC-BASED SBDS</b>	<b>109</b>
5.1 Preamble	109
5.2 Device simulation methodology in SILVACO TCAD	110
5.3 Simulation Results & Discussions	113
5.3.1 Characteristics of as-grown (not-irradiated) Ni/4H-SiC SBD detector	113
5.3.2 Characteristics of Gamma-irradiated (dose=100 Mrad) Ni/4H-SiC SBD detector	115
5.3.3 Characteristics of 8.2 MeV Electron-irradiated Ni/4H-SiC SBD detector	119
5.3.4 Characteristics of 6.5 MeV proton-irradiated Ni/4H-SiC SBD detector	122
5.3.5 Characteristics of Neutron-irradiated Ni/4H-SiC SBD detector	125
5.4 Summary	129
<b>CHAPTER 6: SUMMARY, CONCLUSIONS AND FUTURE DIRECTIONS</b>	<b>131</b>
6.1 Summary & Conclusions	131
6.2 Scope for the future work	136
<b>REFERENCES</b>	<b>137</b>



# SYNOPSIS

---

Neutron detectors are an inevitable component of a Neutron Flux Monitoring System (NFMS) in a nuclear power plant. They measure neutron flux at various core locations by which distinct signals such as absolute power, rate of change of power (period), and change in reactivity are generated to enable control of the reactor power and also to initiate safety action on crossing threshold. Hence, the Instrumentation and Control (I&C) system of a nuclear power plant is necessary to have a reliable and fast acting neutron flux monitoring system for ensuring its safe operation in all states of operation. The state-of-the-art gas-filled neutron detectors such as fission chambers,  $^{10}\text{B}$  and  $\text{BF}_3$  proportional counters, and  $^{10}\text{B}$  based Compensated Ion Chambers (CICs) are generally deployed for this purpose.

In the recent past, particularly after Fukushima accident, more emphasis has been given to core safety in the design of nuclear reactors with the aim of practically eliminating the core disruptive accidents. For this to happen, I&C system design demands improved reliability. To meet this objective, more redundant and diverse design of neutron detectors is essential in the NFMS. In India, developing a miniature detector system which can withstand harsh-environments with comparable performance of gas-filled detectors is the need of the day, for usage in future fast reactors. The works carried out towards the development of such a diverse neutron detector is presented in this thesis. After detailed and systematic review, a wide band-gap semiconductor, i.e., Silicon Carbide (SiC) has been chosen for developing a diverse neutron detector for harsh-environments of fast reactors.

The primary objective of this thesis is to provide the theoretical basis for the optimization of semiconductor detectors and ensuring the harsh-environment operability before its costly and time consuming fabrication process.

Towards the development of a SiC-based fast neutron detector, the following important works are carried out and presented in this thesis:

**a) Development of a suitable computational model to study the physics of SiC-based detectors and to perform Monte-Carlo based simulation towards optimization of converter layer**

A planar structure of SiC-based semiconductor neutron detector is modeled using the Monte-Carlo tool, i.e., **GEANT4 (GEometry AND Tracking)**. It's benchmarking and validation has been carried out with the published results. The performance of several hydrogenous converter materials has been studied in the harsh-environments of Fast Breeder Reactors (FBRs) by juxtaposing with SiC detector. This study provides the optimization of several converter materials for different energy neutron sources and the corresponding efficiency offered by SiC-based detectors.

**b) Study for improving the detector performance in terms of background discrimination and efficiency**

One of the major issues with the neutron detectors is the spurious counts from the background irradiation such as  $\gamma$ -rays. This study involves the discrimination of the background radiations and its effect on the neutron detection efficiency. Furthermore, it is desirable to achieve efficiency equivalent to or better than gas-filled detectors.

**c) Device simulation and assessing the system performance in harsh environments**

This work involves the modeling of the SiC-based Schottky Barrier Diode (SBD) in the device simulation tool, i.e., **Technology Computer-Aided Design (TCAD)** from Silvaco<sup>TM</sup>, and its validation with the literature. Further work involves introducing deep-levels due to gamma, proton, electron, and neutron irradiations, and studying its

effect on the device characteristics to predict the degradation with respect to increasing radiation fluence.

*In summary, a novel LiH-SiC-based stacked neutron detector has been optimized and the effects of irradiation on the SiC device characteristics have been assessed for its applications in the harsh environment of fast reactors.*





# LIST OF FIGURES

---

Figure 1.1 Tetrahedral bonding of (a) Si-atom with the four nearest C-atoms, and (b) C-atom with the four nearest Si-atoms [22]	7
Figure 2.1 Types of neutron interactions with materials.	16
Figure 2.2 Neutron elastic scattering interaction diagram.	18
Figure 2.3 Total neutron cross-sections for $^3\text{He}$ , $^6\text{Li}$ , and $^{10}\text{B}$ isotopes [58].	22
Figure 2.4 Schematic diagram of a typical Gas-filled detector.	25
Figure 2.5 Schematic diagram of a scintillation detector with PMT setup [60].	26
Figure 2.6 Schematic of a semiconductor diode detector.	27
Figure 2.7 Schematic of detector electronics.	27
Figure 2.8 Representation of (a) Direct (b) Indirect-Conversion Neutron Detectors.	28
Figure 2.9 Schematic of the (a) planar structure of SD; few 3D structures (b) Stacked SD (c) single side trench structure (d) double side trench structure [64].	29
Figure 2.10 Sketch of planar SD illustrating various possibilities of secondary charged particles movement which reflects whether the neutron is detected or undetected.	30
Figure 2.11 Energy band diagram of metal n-type semiconductor contact with $\Phi_M$ $> \Phi_S$ .	32
Figure 2.12 Basic current transport mechanisms across the M-S junction.	35
Figure 2.13 The schematic diagram of point defects in semiconductors, taken from [72].	39
Figure 2.14 The schematic diagram of different carrier transitions between deep- levels and the energy bands.	41
Figure 3.1 An illustration of the GEANT4 process flow.	54
Figure 3.2 ATLAS inputs and outputs [92].	58
Figure 3.3 Simulated reverse $J$ - $V$ -characteristics of Ni/4H-SiC SBD with and without the barrier lowering and tunneling models.	63
Figure 3.4 Simulated $(1/C^2)$ - $V$ and $C$ - $V$ curve at 523 K with low (1 kHz) and high (1 MHz) frequency ac signals.	64

Figure 4.1 (a) Schematic of the Planar detector configuration (b) Screenshot from GEANT4 simulation.	69
Figure 4.2 Spectrum of the source used for simulating the mixed neutron-gamma source	70
Figure 4.3 Stacked detector schematic.	71
Figure 4.4 GEANT4 vs. Analytical calculation of $P(I)$ .	73
Figure 4.5 (a) Detector and source setup as described by K. Sedlackova et al. [46], (b) The neutron spectrum of the $^{239}\text{Pu}$ -Be source.	75
Figure 4.6 Range of proton in HDPE and SiC material (computed using SRIM software).	76
Figure 4.7 Optimization of HDPE thickness for $^{239}\text{Pu}$ -Be neutron source and estimation of neutron detection efficiency with the help of Monte-Carlo simulation tools: GEANT4 (this work) and MCNPX (K. Sedlackova et al. [46]).	76
Figure 4.8 Neutron detection efficiency vs. HDPE converter thickness for 2.5 MeV D-D neutron source and comparison with the GEANT4 simulation work by Cortesi <i>et al.</i> , [96].	77
Figure 4.9 Energy deposited in SiC by all particles (★), recoil protons (o), and other charged particles (dotted line).	83
Figure 4.10 Spectrum of (a) $^{252}\text{Cf}$ and (b) $^{241}\text{Am}$ -Be neutron sources [100].	84
Figure 4.11 Optimization of HDPE thickness for (a) $^{252}\text{Cf}$ and $^{241}\text{Am}$ -Be (b) various mono-energetic ( $E_n = 0.5$ to 10, and 14 MeV) neutron sources.	85
Figure 4.12 Efficiency of neutron detector with a 400 $\mu\text{m}$ thick HDPE converter for different mono-energetic neutron sources.	86
Figure 4.13 Comparison of energy deposition in detector's active region (histograms) due to gamma ( $E_{\text{mean}} = \sim 148$ keV) and neutron ( $E_{\text{mean}} = \sim 3.2$ MeV) events.	87
Figure 4.14 Effect of LLD on HDPE-SiC-based detector efficiency.	87
Figure 4.15 Increment in the efficiency of HDPE-SiC-based detector with various stacked layers.	89
Figure 4.16 Efficiency variation with respect to converter thicknesses for a stacked detector with different number of stacked layers viz., 5, 10, 15, 20 and 50.	90

Figure 4.17 Comparison of detection efficiency offered by selected converter materials.	92
Figure 4.18 Range of protons and $^7\text{Li}$ ion in LiH converter material (calculated using SRIM package).	94
Figure 4.19 Efficiency vs. LiH thickness for different mono-energetic neutron sources.	95
Figure 4.20 Efficiency vs. LiH thickness for $^{241}\text{Am}$ -Be neutron source.	95
Figure 4.21 Comparison of energy deposition (histograms) in the detector active region due to gamma ( $E_{\text{mean}} = \sim 150 \text{ keV}$ ) and neutron ( $E_{\text{mean}} = \sim 3.5 \text{ MeV}$ ) events.	97
Figure 4.22 Effect of various LLD threshold values on the neutron detection efficiency of the LiH-SiC-based detector.	98
Figure 4.23 Increment in the detection efficiency of LiH-SiC-based detector with various stacked layers.	100
Figure 4.24 Efficiency variation with respect to converter thicknesses for a stacked detector with a different number of stacked layers viz., 5, 10, 15, 20 and 50.	101
Figure 4.25 The histogram of the total energy deposited in the active region of SiC by the secondary charged particles generated due to the neutron interaction in the HDPE and LiH converters.	101
Figure 4.26 The histogram of energy deposition by the recoil-protons (generated in LiH and HDPE) in SiC active region.	102
Figure 4.27 Efficiency versus perylene thickness for various mono-energetic neutrons.	104
Figure 4.28 Perylene thickness optimization for $^{241}\text{Am}$ -Be Neutron source.	105
Figure 4.29 GEANT4 simulation in Real World Scenario.	106
Figure 4.30 Efficiency vs. LiH converter thickness of LiH-SiC-based FND for planar and multiple sources	106
Figure 5.1 (a) Schematic of $n$ -type 4H-SiC 2D-structure simulated in TCAD (b) 2D-structure generated in DEVEDIT module.	110
Figure 5.2 Simulated forward $J$ - $V$ - $T$ -characteristics of as-grown Ni/4H-SiC-based SBD. (Inset: forward $\ln(J)$ - $V$ - $T$ curve).	114
Figure 5.3 Simulated reverse $J$ - $V$ - $T$ -characteristics of as-grown Ni/4H-SiC-based SBD.	114

Figure 5.4 Reverse $J$ - $V$ -characteristics of Ni/4H-SiC-based SBD prior to and after the gamma irradiation of dose equivalent to 100 Mrad.	117
Figure 5.5 Electric field strength at the Ni-Schottky contact and SiC interface of the SBD prior to and after the $\gamma$ -irradiation (dose = 100 Mrad), obtained from the cutline of Electric-Field contour from the simulated structure.	117
Figure 5.6 Simulated forward $J$ - $V$ -characteristics of Ni/4H-SiC-based SBD prior to and after the $\gamma$ -irradiation (dose=100 Mrad). (Inset: Reverse $\ln(J)$ - $V$ plot).	118
Figure 5.7 Simulated $(1/C^2)$ - $V$ and $C$ - $V$ -characteristics of Ni/4H-SiC SBD prior to and after the $\gamma$ -irradiation.	118
Figure 5.8 Forward characteristics ( $\ln J$ - $V$ plot) of Ni/4H-SiC SBD before and after the 8.2 MeV high energy electron (HEE) irradiation at various fluence levels.	121
Figure 5.9 Reverse characteristics of Ni/4H-SiC SBD before and after the 8.2 MeV high energy electron irradiation at different fluence levels.	121
Figure 5.10 Simulated $C$ - $V$ -characteristics of Ni/4H-SiC SBD before and after the 8.2 MeV high energy electron (HEE) irradiation at different fluence levels. Due to flat $C$ - $V$ -curve at the fluence of $10^{16}$ electrons/cm <sup>2</sup> , the $(1/C^2)$ - $V$ plot for that fluence level could not be estimated.	122
Figure 5.11 Forward characteristics ( $\ln J$ - $V$ plot) of Ni/4H-SiC SBD before and after the 6.5 MeV proton irradiation at various fluence levels.	123
Figure 5.12 Reverse characteristics of Ni/4H-SiC SBD before and after the 6.5 MeV proton irradiation at different fluence levels.	124
Figure 5.13 Simulated $C$ - $V$ -characteristics of Ni/4H-SiC SBD before and after the 6.5 MeV proton irradiation at different fluence levels.	124
Figure 5.14 Simulated forward $J$ - $V$ -characteristics of Ni/4H-SiC SBD prior to and after the neutron irradiation of various fluences ( $0, 10^{11} - 10^{16}$ neutrons/cm <sup>2</sup> ) (Inset: $\ln(J)$ - $V$ plot).	127
Figure 5.15 Simulated forward and reverse current density as a function of neutron fluence, calculated at +2 V and -100 V, respectively.	127
Figure 5.16 Simulated reverse $J$ - $V$ -characteristics of Ni/4H-SiC SBD prior to and after the neutron irradiation at various fluences ( $\Phi_n = 10^{12} - 10^{16}$ neutrons/cm <sup>2</sup> ).	128

Figure 5.17 Simulated $(1/C^2)$ - $V$ and $C$ - $V$ -characteristics of Ni/4H-SiC SBD prior to and after the neutron-irradiation of various fluences.	128
Figure 5.18 Breakdown simulation of Ni/4H-SiC SBD before and after the neutron irradiations.	129



# LIST OF TABLES

---

Table 1.1 Properties of several semiconductor materials.	5
Table 1.2 Comparisons of properties of common SiC polytypes with Si [29]–[31].	7
Table 2.1 Types of neutron interactions.	20
Table 2.2 Converter materials for thermal neutron detection.	22
Table 2.3 Work-function of several metals for Schottky contact formation on SiC [73].	33
Table 3.1 Details of GEANT4 C++ files for modeling neutron detector.	51
Table 3.2 Description of modules and I/O files of Silvaco TCAD used in this thesis.	58
Table 4.1 List of nuclear reactions in SiC material for $10^6$ incident neutrons.	79
Table 4.2 List of generated particles in SiC with their mean kinetic energy for $10^6$ incident neutrons.	80
Table 4.3 List of nuclear reactions in HDPE converter for $10^6$ incident neutrons.	82
Table 4.4 List of generated particles in HDPE with their mean kinetic energy for $10^6$ incident neutrons.	82
Table 4.5 Properties of various neutron converter materials.	91
Table 4.6 List of Nuclear reactions happening in LiH material for $10^6$ incident neutrons.	93
Table 4.7 Optimized thickness and efficiency of the LiH-SiC detector for different energy neutrons.	96
Table 4.8 Optimized thickness and efficiency of the perylene-SiC detector for different energy neutrons.	104
Table 5.1 TCAD model parameter values for the modeling of SiC-based devices.	111
Table 5.2 Trap signatures introduced in as-grown Ni/4H-SiC SBD detector model [59].	113
Table 5.3 Trap signatures introduced in gamma-irradiated (dose = 100 Mrad) Ni/4H-SiC SBD detector model [59].	116
Table 5.4 Properties of traps introduced in 8.2 MeV electron-irradiated SiC-based SBD (Fluence = $9.5 \times 10^{14}$ electrons/cm <sup>2</sup> ) [55].	119
Table 5.5 Properties of traps introduced in 6.5 MeV proton-irradiated SiC-based SBD (Fluence = $3.2 \times 10^{13}$ protons/cm <sup>2</sup> ) [55].	123

Table 5.6 Trap signatures introduced in 1 MeV equivalent neutron-irradiated Ni/4H-SiC SBD detector model at the fluence of $1 \times 10^{11}$ neutrons/cm <sup>2</sup> [29], [56], [58].	125
Table 5.7 Device parameters determined from the I-V & C-V simulations of the Ni/4H-SiC SBD.	130



# LIST OF ABBREVIATIONS

---

FBRs	Fast Breeder Reactor
FNDs	Fast Neutron Detectors
GEANT4	Geometry And Tracking (A Monte-Carlo based code)
GPS	General Particle Source
HDPE	High Density Polyethylene
I&C	Instrumentation and Control
K.E.	Kinetic Energy
keV	Kilo-Electron Volts
LiH	Lithium Hydride
LLD	Low Level Discriminator
meV	Milli-Electron Volts
MeV	Mega-Electron Volts
M-S	Metal-Semiconductor junction
MW	Mega Watts
NFMS	Neutron Flux Monitoring System
NIEL	Non-Ionizing Energy Loss
PDF	Probability Distribution Function
SBDs	Schottky Barrier Diodes
SBH	Schottky Barrier Height
SiC	Silicon Carbide
SDs	Semiconductor Detectors
TCAD	Technology Computer-Aided Design
TE	Thermionic Emission



# 1

## INTRODUCTION

---

### 1.1 PREAMBLE

The neutron is a subatomic neutral particle which makes it pivotal for a variety of applications. For instance, neutrons play key role in neutron scattering experiments for studying the different physical properties of materials [1]; in Neutron Activation Analysis for determining the concentrations of elements [2]; in neutron capture therapy for treating the cancer patients [3]; in neutron tomography for 3D-imaging [4]; and another important application is in the nuclear reactors where neutrons are responsible for sustaining fission chain reaction [5]. All these applications require an indispensable sensor, generally referred as “*Neutron Detectors*” to detect or count the presence of neutrons. The zero electric charge, empowers neutrons to penetrate deeper and traverse considerable distance in the medium without undergoing any interaction, hence without being detected. Additionally, unlike charged particles (e.g.,  $\alpha$ , proton, heavy ions), neutrons do not ionize the atoms directly. Therefore, their detection is quite challenging and rely on the measurement of secondary charged particles that are generated as a result of complex nuclear (neutron-nucleus) reactions [6].

In nuclear applications, neutron detectors are the most crucial components in Neutron Flux Monitoring System (NFMS). They measure neutron flux ( $\Phi$ ), i.e., number of neutrons/cm<sup>2</sup>/s, at various core locations. The neutron flux in a reactor is approximately expressed by Equation (1.1) [7]:

$$\Phi = 3.125 \times 10^{12} \times \frac{P \text{ (MW)}}{\Sigma_f} \quad (1.1)$$

where  $\Sigma_f$  is the macroscopic cross-section ( $\text{cm}^{-1}$ ) for the fission reaction in the reactor core. The reactor power (megawatts) is proportional to the neutron flux. It is apparent that for control and monitoring of the nuclear reactor, the information regarding the neutron population is exceptionally essential. Based on the neutron flux information, the NFMS generates various signals such as absolute power, rate of change of power (period), change in reactivity, etc., to enable control of the reactor power, and also initiate safety action on crossing their threshold values. Hence, Instrumentation and Control (I&C) system of a nuclear power plant is necessary to have a reliable and fast acting neutron flux monitoring system for ensuring its safety for all the states of operation, i.e., start-up, intermediate and power ranges, shutdown, fuel handling, and during all design basis events [8].

Neutron detectors are broadly categorized as gas-filled detectors, scintillators, and thin-film-coated semiconductor diodes, elucidated in Chapter 2. For nuclear applications, state-of-the-art gas-filled neutron detectors such as fission chambers,  $^{10}\text{B}$  and  $\text{BF}_3$  proportional counters, and  $^{10}\text{B}$  based Compensated Ion Chambers (CICs) are generally deployed. In gas-filled detectors, the incident neutrons interact with the neutron sensitive material coated on the inner wall of a gas-filled chamber and generate secondary charged particles (e.g.,  $\alpha$ -particles or highly charged fission fragments) which initiate ionization or/and excitation in the filled gas. The electron-ion pairs generated in this process are collected on the electrodes by applying a high voltage supply. The corresponding electrical signal indicates the presence of neutrons. The limitations of these gas-filled detectors include large dimension, requirement of high voltage supply and need of pure gas for their efficient operation. Additionally, they require relatively high energy ( $\sim 25\text{--}30$  eV) to create

electron-ion pairs in the filled gas which results in a reduced number of charge pairs and eventually low output signal [9].

In medium sized sodium cooled pool type Fast Breeder Reactors (FBRs) [10], [11], since the core is designed not in the most reactive configuration, the online reactivity monitoring is generally adapted to detect and initiate safety action at the incipient stage itself even for small changes in the core state. It is very challenging to have a single detector system to monitor neutron flux over ten orders of magnitude, spanning shutdown to full power, particularly in a pool type reactor such as the Indian 500 MWe sodium cooled pool type Prototype Fast Breeder Reactor (PFBR) [8]. Due to the provision of thick radial and axial shielding in the design to protect the reactor core components, the neutron flux is highly attenuated at the ex-core, and ex-vessel detector locations. Hence, combination of different detectors (for different states of operation) working in different modes (pulse mode, Campbell mode and pulse mode with linear count rate meters) are deployed at both in-vessel and out-vessel locations [8]. The presence of harsh environments such as high temperature ( $\sim 500^\circ\text{C}$ ), high gamma dose (100 Mrad), and high neutron fluxes ( $\sim 10^{15} \text{ n/cm}^2/\text{s}$ ) within the vessel and very low neutron flux at ex-vessel locations, dictates the designing aspects of the high-temperature fission chambers (HTFCs) [8]. The challenges involved in the designing of HTFC detectors are:

- Unavailability of enriched uranium to achieve higher sensitivities.
- Disintegration of uranium coating due to thermal shocks.
- Chemical cleaning of the gas is required to the extent of parts per billion (ppb) levels.
- Welding/brazing joints, metal-ceramic seals must withstand high pressure and temperature fluctuations.
- Increase in the leakage currents due to decrease in the insulation resistance of ceramic materials in the vessel at high temperature.

### 1.2 MOTIVATION

In the recent past, particularly after the Fukushima accident, the core safety aspect in designing of nuclear reactors has gained a revised emphasis and increased attention, with an aim of practically eliminating the core disruptive accidents. For this to happen, I&C system design demands improved reliability. To meet this objective, redundant and diverse design of neutron detectors is essential in the neutron flux monitoring system. Redundant gas-filled detectors are already deployed for this purpose. The common mode of failures can further be minimized through implementation of diverse detectors in the system. Hence, developing a miniature detector system which can withstand harsh-environments with comparable performance of gas-filled detectors is the need of the day, for usage in future indigenous fast reactors. Feasibility studies carried out towards the development of such a diverse neutron detector is presented in this thesis.

Neutron detection techniques other than gas-filled detectors have to be considered for implementing the diversity factor. The alternatives could be scintillators or semiconductor-based detectors. The scintillators are not considered for this study as they cease to withstand the harsh-environment of fast reactors and are poor in terms of gamma-discrimination. They also require heavy and delicate Photo Multiplier Tubes for their operation. On the other hand, semiconductor detectors (SDs) have inherent advantages such as the requirement of low power for its operation, mass production can lead to cost reduction, and compact size eases the handling and installation of the detector. Most importantly, they require relatively lower energy  $\sim 3\text{--}10$  eV per electron-hole pair created, which results in a large number of charge carriers and eventually better signal and resultant high energy resolution. High mobility of electrons and a smaller area to cover, further, enhances the charge-collection, counting rate, and much improved signal to noise ratio of the SDs. However, devices based on conventional semiconductors such as Si and Ge are

unable to withstand high temperature due to their low band-gap, and are also quite prone to radiation induced damages [12], [13]. Hence, conventional semiconductor-based detectors are limited to low temperature ( $< 300$  K) applications having adequate cooling provisions [14], [15]. The high doses of radiation causing the following effects: a) increases the leakage current which leads to device failure, b) decreases the depletion width which results in higher dark currents c) changes the effective doping concentration which eventually leads to type inversion, d) affects the charge collection properties of the device which degrades the detection efficiency, etc. These limitations of Si-based devices have motivated the evolution of radiation hard semiconductor devices based on wide band-gap semiconductor materials such as Silicon Carbide (SiC), Aluminum Nitride (AlN), Boron Nitride (BN), Gallium Arsenide (GaAs) and Gallium Nitride (GaN) [16]–[20]. Their wider band-gaps make them suitable for operating in harsh environments. Table 1.1 shows the properties of several semiconductor materials.

**Table 1.1 Properties of several semiconductor materials.**

Properties	Si	Ge	GaAs	4H-SiC	Diamond	GaN	Cd(Zn)Te
Atomic Number (Z)	14	32	31/33	14/6	6	31/7	48/52
Band-gap $E_g$ (eV)	1.12	0.67	1.43	3.25	5.5	3.39	1.4-1.6
Density (g-cm <sup>-3</sup> )	2.33	5.323	5.3	3.23	3.5	5.3	5.9
e-h pair creation energy (eV)	3.6	2.96	4.3	7.8	13	8.9	4.4
Electron mobility (cm <sup>2</sup> /V-s)	1450	3900	8500	1000	1800	440	1100
Hole mobility (cm <sup>2</sup> /V-s)	450	1900	400	115	1200	200	100
Electron lifetime (s)	$>10^{-3}$	$>10^{-3}$	$10^{-8}$	$5 \times 10^{-7}$	$> 10^{-6}$	$10^{-9}$	$10^{-6}$
Melting point (°C)	1412	938	1238	2827	3500	3200	1092
Dielectric constant	11.7	16	12.8	9.7	5.5	8.9	10.9
Displacement threshold (eV)	13	20	10	21.8	43	19.5	-
Breakdown voltage, (MV/cm)	0.5	0.1	0.4	4	10	5	-

In particular, SiC, with a wide band-gap of  $\sim 3.25$  eV and displacement threshold\* energy of 21.8 eV [16], [21], has shown great potential to become a future material of choice for harsh environment radiation detectors. Si and C atoms in SiC can directly undergo elastic and inelastic scattering reactions, discussed in Chapter 2, upon interaction with fast neutrons [22], [23]. In addition to that, a layer of neutron sensitive hydrogenous converter material (for which fast neutrons have relatively high cross-section for elastic scattering interaction) can further enhance the detection efficiency [24], [25]. Thus, neutron detectors of both configurations viz., direct and indirect (discussed in section 2.3.3), can be built using SiC.

### 1.3 SILICON CARBIDE- LITERATURE SURVEY

#### 1.3.1 SiC: salient features and properties

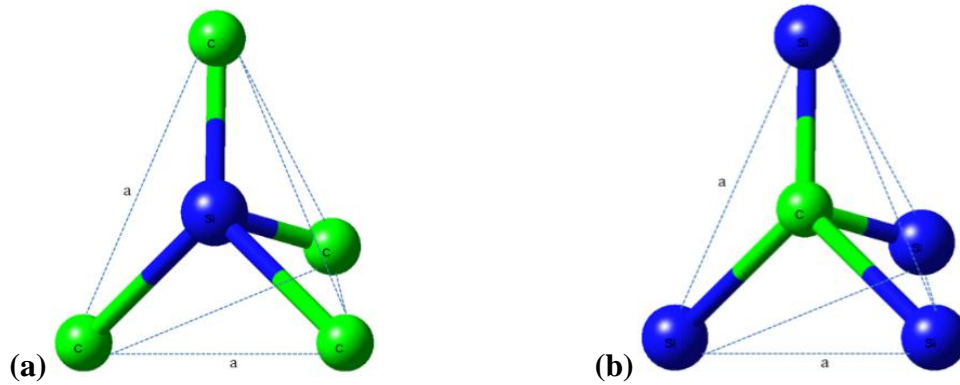
SiC is an indirect and wide band-gap compound semiconductor material with a rigid stoichiometry of 50% silicon (Si) and 50% of carbon (C). Both Si and C atoms are tetravalent elements which contain four valence electrons in their outermost shells. A carbon atom is tetrahedrally bonded with covalent bonds to four neighboring atoms of silicon that are placed in the corner and vice-versa as shown in Figure 1.1 [26]. The bond length between Si and C atoms is  $\sim 1.89$  Å, whereas, between two atoms of the same species (Si–Si or C–C), it is  $\sim 3.08$  Å [27], [28].

One property that makes SiC a compelling and distinctive semiconductor is its ability to form several crystallographic configurations called *polytypes*. The *polytypism* is the phenomenon where material can adopt different crystal structures which vary in one dimension (i.e., in stacking sequence) without changes in chemical composition [29].

---

\* Minimum kinetic energy that an atom in solid needs to get permanently displaced from its lattice site to defect position.





**Figure 1.1 Tetrahedral bonding of (a) Si-atom with the four nearest C-atoms, and (b) C-atom with the four nearest Si-atoms [26]**

The polytypism is the main characteristic of SiC that makes it challenging to study. For SiC, more than 200 different types of polytypes are known. They have distinct physical, electrical, and optical properties. It is owing to this reason; some polytypes are preferred over others. To this date, the 4H-, 6H- and 3C- polytypes of SiC have been most extensively studied and are being widely used in the electronics industry [27], [29]. The names of different polytypes are assigned as per Ramsdell Notation: <number> <letter>; where the number indicates the number of layers before the sequence repeats and the letter denotes the crystal structure. For example, 4H-SiC means four different layers are repeated throughout the material, and the structure is hexagonal. Table 1.2 provides a comparison of the electrical properties of these common SiC polytypes with Si.

**Table 1.2 Comparisons of properties of common SiC polytypes with Si [29]–[31].**

Properties	4H-SiC	6H-SiC	3C-SiC	Si
Band-gap (eV) (300K)	3.26	3.02	2.36	1.12
Relative dielectric constant	9.7	9.7	9.3	11.9
Breakdown field (MV/cm)	3.0	3.2	>1.5	0.6
Thermal conductivity (W/cm-K)	3–5	3–5	3–5	1.5
Electron Mobility ( $\text{cm}^2\text{V}^{-1}\text{s}^{-1}$ )	800	800	750	1200
Electron saturation velocity ( $10^7 \text{ cm/s}$ )	2.0	2.0	2.5	1.0
Electron affinity (eV)	3.1	3.3	3.8	4.05
Intrinsic Carrier concentration ( $\text{cm}^{-3}$ ) (300 K)	$\sim 10^{-7}$	$\sim 10^{-5}$	$\sim 10$	$10^{10}$

The wide band-gap, which is approximately three times that of Si, and low intrinsic carrier concentration make SiC-based devices suitable for high-temperature operations in comparison to Si-based devices [26]. These features restrict the leakage currents that would arise from thermal ionization of electrons from the valence band [27], [32]. Therefore, in theory, SiC-based devices can operate at temperatures as high as 700–1000 °C [26], [27], [32], [33]. However, the practical limit is much lower (~ 250 °C) due to several factors such as thermal runaway, poor packaging technology, contact annealing and ageing of the device [33]–[36]. Funaki *et al.* [36] had shown that the electrical characteristics of SiC Schottky diodes deteriorate significantly when the temperature exceeds 200 °C.

SiC is naturally available as a rare mineral ‘*moissanite*’. On the commercial scale, it is available as a bulk and epitaxial crystal. Physical Vapor Transport (PVT) technique and High-Temperature Chemical Vapor Deposition (HTCVD) are used for the industrial scale manufacturing of bulk SiC. In PVT, a solid source of silicon carbide is evaporated at high temperatures, and the vapors re-crystallize at a colder part of the furnace. The epitaxial growth of SiC is performed using the Chemical Vapor Deposition (CVD) technique [26], [27]. In CVD, gas-phase silicon and carbon containing precursors react in a furnace, and silicon carbide is solidified on the target. Detailed information on SiC growth, the manufacturing process can be found elsewhere [26], [27], [29], [37], [38].

An intrinsic SiC is made *n*-type or *p*-type through doping so that it can be employed for current conduction applications. Nitrogen and Phosphorus are used as a dopant for making *n*-type SiC and aluminum is employed for making *p*-type SiC. Nitrogen substitutes at the C sub-lattice site, while phosphorus and aluminum substitute at the Si sub-lattice site.

### 1.3.2 SiC as a neutron detector

SiC is an ideal semiconductor for fabricating high frequency, high power and high-temperature devices, owing to its high breakdown field; high electron saturated drift velocity and good thermal conductivity. In the past decade, SiC has become an attractive material in the field of nuclear automobiles and aerospace engineering. Due to excellent electronic, chemical and heat transfer properties, SiC is being utilized for a wide range of applications, e.g., as blanket structural material for fusion power plants [39], and as a neutron detector for nuclear reactor power monitoring [16], [21], [40] and special nuclear material detection at sea/air-ports. SiC-based neutron detectors works on the same principle as other semiconductor-based detectors. The working principle of a typical semiconductor based neutron detector is described in Section 2.3.3.

Seshadri *et al.* [16], [21] and Dullo *et al.* [40], [41] have demonstrated the potential of SiC to be used as a thermal neutron ( $E_n = 25$  meV) detector with suitable neutron converter foil (LiF) for harsh environments. Dullo *et al.* [41] have shown that the thermal-neutron response of the irradiated SiC Schottky Barrier Diode (SBD) was unchanged even after fast ( $E_n > 1$  MeV) neutron fluence of  $1.3 \times 10^{15}$  n/cm<sup>2</sup>. Sciortino *et al.* [42] and Ruddy *et al.* [43], [44] have shown that SiC-based detectors provide excellent response to the  $\alpha$ -particle detection and spectroscopy even after the heavy irradiation of proton and gamma-rays, respectively. Ruddy *et al.* [45] have used SiC-based fast neutron detector for power monitoring application in space reactors. They have reported that the SiC-based detector can sustain neutron fluence of  $4.2 \times 10^{17}$  n/cm<sup>2</sup> and gamma dose of  $2.1 \times 10^8$  rad. Jang *et al.* [46] have reported a self-biased fast neutron detector based on 4H-SiC PIN-type diode. They have obtained the neutron detection efficiency of  $5.1 \times 10^{-4}$  for <sup>241</sup>Am-Be neutron source having flux intensity of  $1.1 \times 10^6$  n/cm<sup>2</sup>/s. They have also achieved the charge collection efficiency (CCE) of 65% at zero biased voltage. In other work, Jang *et al.* [47]

have shown a self-biased neutron detector based on SiC-based SBDs with  $^6\text{LiF}$  and  $^{10}\text{B}_2\text{O}_3$  neutron sensitive thin films. They were able to achieve the CCE of over 80% at zero bias voltage and  $\sim 100\%$  at 25 V biasing. They have also investigated and reported negligible effect of  $\gamma$ -irradiation (dose = 120 kGy) and  $^{252}\text{Cf}$  neutron-irradiation (fluence= $10^8$  n/cm<sup>2</sup>) on electrical characteristics of these detectors. Alessandro *et al.* [48] have tested a  $^6\text{LiF}$  equipped 4H-SiC Schottky diode for neutron measurement in TAPIRO fast reactor (at 5kW reactor power) for Boron Neutron Capture Therapy (BNCT) applications. They have observed the decrease in count rate by 0.3% following the neutron fluence of  $10^{13}$  n/cm<sup>2</sup>. Manfredotti *et al.* [49] have demonstrated the advantage of SiC-based detector over Si or GaAs-based detectors with  $^6\text{LiF}$  and  $^{10}\text{B}$  converter materials. Flammang *et al.* [24] have discussed the capability of SiC-based detector to detect the neutrons from 2.5 MeV D-D neutron source with polyethylene converter material. They have experimentally optimized the thickness of polyethylene for 2.5 MeV D-D neutron source. Katarina *et al.* [50] have detected the neutrons from  $^{239}\text{Pu}$ -Be neutron source by coating High-Density Polyethylene (HDPE) converter layer on top of SiC. They have optimized the thickness of HDPE using the Monte-Carlo simulation tool, i.e., MCNPX (version 2.7).

It is noted that as the thickness of converter increases, the probability of neutron interaction increases (discussed elaborately in section 4.3.1). However, larger thickness limits the number of secondary charged particles reaching the SiC region (due to continuous energy loss in the converter followed by absorption in the converter). **Hence, the optimization of converter thickness is a vital aspect in the design of semiconductor neutron detectors.**

It is a well known fact that high dose of irradiation on any semiconductor device creates several kinds of defects. Majority of these defects are electrically active and introduce deep-levels (trap centers) in the band-gap of the semiconductor. They can

significantly modify the electrical properties of the semiconductor devices [29]. There are several studies which report on the radiation-induced damages on the SiC-based devices [42], [51]–[56]. They have reported the defects generated in SiC that are subjected to a particular dose or fluence level of specific particles such as electron, proton, gamma, or neutron, etc. Nava *et al.* [57] and Raja *et al.* [58], [59] had reported effects on electrical characteristics of SiC-based detectors which are subjected to neutron and gamma-irradiations, respectively. There are enough evidences which evince the radiation hardness of SiC-based detectors. However, surprisingly there are very few literature that reports on the effect of irradiation on electrical characteristics of SiC-based devices, and those are also limited to a specific fluence or dose levels. **Hence, it is desirable to study the performance of the SiC-based detectors which are subjected to a high fluence of irradiations.**

#### **1.4 OBJECTIVES AND STUDIES PERFORMED**

The primary objective of this thesis is to provide a theoretical basis for the optimized design of SDs for applications in harsh-environments of fast reactors before its fabrication process. Towards the development of a SiC-based fast neutron detector, the following important investigations are envisaged:

- a) Development of a suitable computational model to study the physics of SiC-based detectors and to perform Monte-Carlo based simulation towards optimization of converter layer**

The optimization studies of the SDs are not viable through experiments. Moreover, neutron transport in matter is random which can be studied effectively by using Monte-Carlo methods with exact geometrical models. Therefore, a Monte-Carlo toolkit, i.e., **GEANT4 (GEometry AND Tracking)** is employed in this study. The

performance of several hydrogenous converter materials, juxtaposed with SiC, has to be studied in the harsh-environments of FBRs. This study provides the optimization of several converter materials for different energy neutron sources and the corresponding efficiency offered by the detectors. Further, the **GEANT4** modeling of a neutron detector is benchmarked against the published results with HDPE as a converter material.

**b) Study for improving the detector performance in terms of background discrimination and efficiency**

One of the major issues with the neutron detectors is the spurious counts from the background radiations such as  $\gamma$ -rays. This study involves the discrimination of the background radiations and its effect on the neutron detection efficiency. Furthermore, it is desirable to achieve efficiency equivalent to or better than gas-filled detectors.

**c) Device simulation and assessing the system performance in harsh environments**

This work involves the modeling of SiC-based SBDs in the device simulation tool, i.e., **Technology Computer-Aided Design (TCAD)** from Silvaco<sup>TM</sup>, and its validation with the literature. Further work involves introducing deep-levels due to gamma, proton, electron, and neutron irradiations, and studying its effect on the device characteristics to predict the degradation with respect to increasing radiation fluence.

## 1.5 ORGANIZATION OF THE THESIS

To achieve the above set of objectives, various studies have been performed. Results of these studies are presented in the following chapters:

**Chapter 1** introduces the need for neutron detectors in nuclear reactor application and provides the motivation for this work. This chapter also contains the literature survey of SiC- semiconductor based neutron detectors.

**Chapter 2** provides the theoretical background of neutron interactions and working principle of several kinds of neutron detectors and their limitations. This chapter also briefly discusses the metal-semiconductor junctions, current transport mechanism in Schottky diodes,  $I$ - $V$  and  $C$ - $V$  characterization theory, and defects in semiconductors.

**Chapter 3** introduces the state-of-the-art design simulation tools used for this work. It presents the challenges involved in modeling and simulation of the particle transport. The needs for Monte-Carlo techniques for such problems are also highlighted. The development of a detector model using the features provided by GEANT4 and flow of the simulation are also discussed. This chapter also includes a brief introduction about Silvaco TCAD and its modules, simulation methodology, crucial physical model and their parameters necessary for modeling SiC-based devices.

**Chapter 4** presents the detailed GEANT4 simulation studies for the design optimization of the neutron sensitive converter layer for several mono-energetic as well as standard neutron sources. This chapter covers the validation of the detector modeled using GEANT4 toolkit with published results. Furthermore, the effect of background discrimination on the neutron detection efficiency and efficiency enhancement studies are also presented in this chapter.

**Chapter 5** deals with the TCAD simulation study of the irradiation effects on the electrical characteristics of a SiC-based SBD detector. This study is performed to predict the ageing of the SDs that are subjected to high doses of irradiations.

**Chapter 6** summarizes the results and conclusions derived from the works performed in this thesis. The scopes for future works are also highlighted in this chapter.

\*\*\*\*\*



# 2

## BASICS OF NEUTRON DETECTION

---

### 2.1 PREAMBLE

Theoretical aspects of neutron interaction with matter, Schottky device operation and defects in semiconductors with special emphasis on SiC, are presented in this chapter.

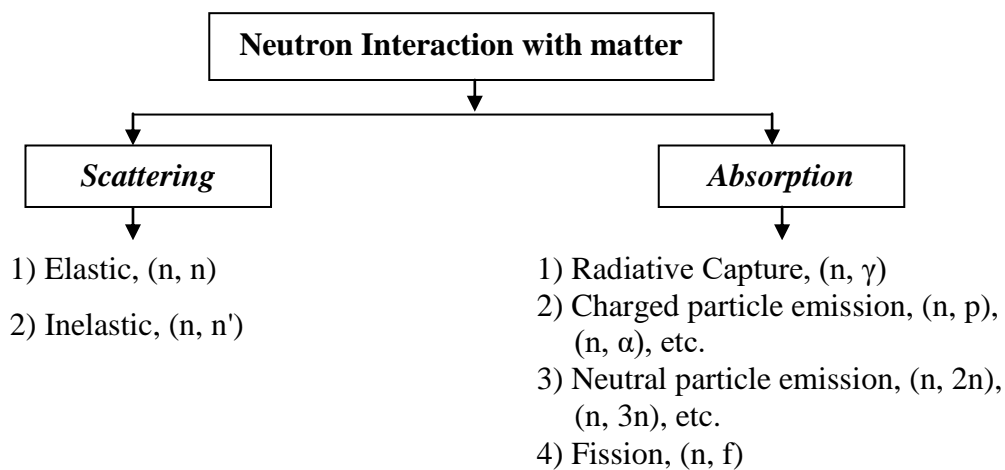
Section 2.2 briefly presents the details of various types of neutron interactions with material. Section 2.3 briefly discusses the working principle of several kinds of neutron detectors and their limitations. Particular emphasis has been given to semiconductor based neutron detectors. Section 2.4 describes the theoretical aspects of metal-semiconductor interface, Schottky and ohmic contacts, current conduction mechanism, and  $I$ - $V$ / $C$ - $V$  relationships. In Section 2.5, several kinds of defects in semiconductors with special emphasis to the deep levels that are reported to be found in 4H-SiC are outlined.

### 2.2 MECHANISMS OF NEUTRON INTERACTION WITH MATTER

Due to zero electric charge, neutrons do not interact by Columbic force with the orbital electrons of the matter in which they traverse [60]. In other words, neutrons do not create ionization directly in the material. Therefore, they can travel a considerable distance in the material without interacting [6]. As a consequence, they can be invisible to general-purpose charged particle detectors. However, neutrons can interact directly with the nuclei of the matter by the strong nuclear forces and can generate secondary charged particles [60]. These secondary charged particles can easily be detected to enable indirect detection

of neutrons [9], [61]. Hence, it is imperative to understand the various neutron interaction mechanisms before studying several types of neutron detectors.

A neutron can interact with the nucleus of the material in several ways (Figure 2.1), which can be mainly categorized into two types of mechanisms viz., scattering and absorption.



**Figure 2.1 Types of neutron interactions with materials.**

### 2.2.1 Scattering interaction

In the event of scattering, the incident neutron interacts with the nucleus of the target material and gets scattered in other direction after imparting part of its kinetic energy (K.E.) to the nucleus. The resultant nucleus with specific kinetic energy is termed as *recoil nucleus*. An incident particle may undergo two types of scattering reactions namely, *elastic* and *inelastic*.

During **elastic scattering**, the total kinetic energy of the neutron and nucleus is conserved. The incident neutron transfers a fraction of its kinetic energy to the nucleus, complying with the conservation laws of energy and linear momentum. The elastic scattering interaction occurs with a zero threshold. Thus it does not depend on the energy of

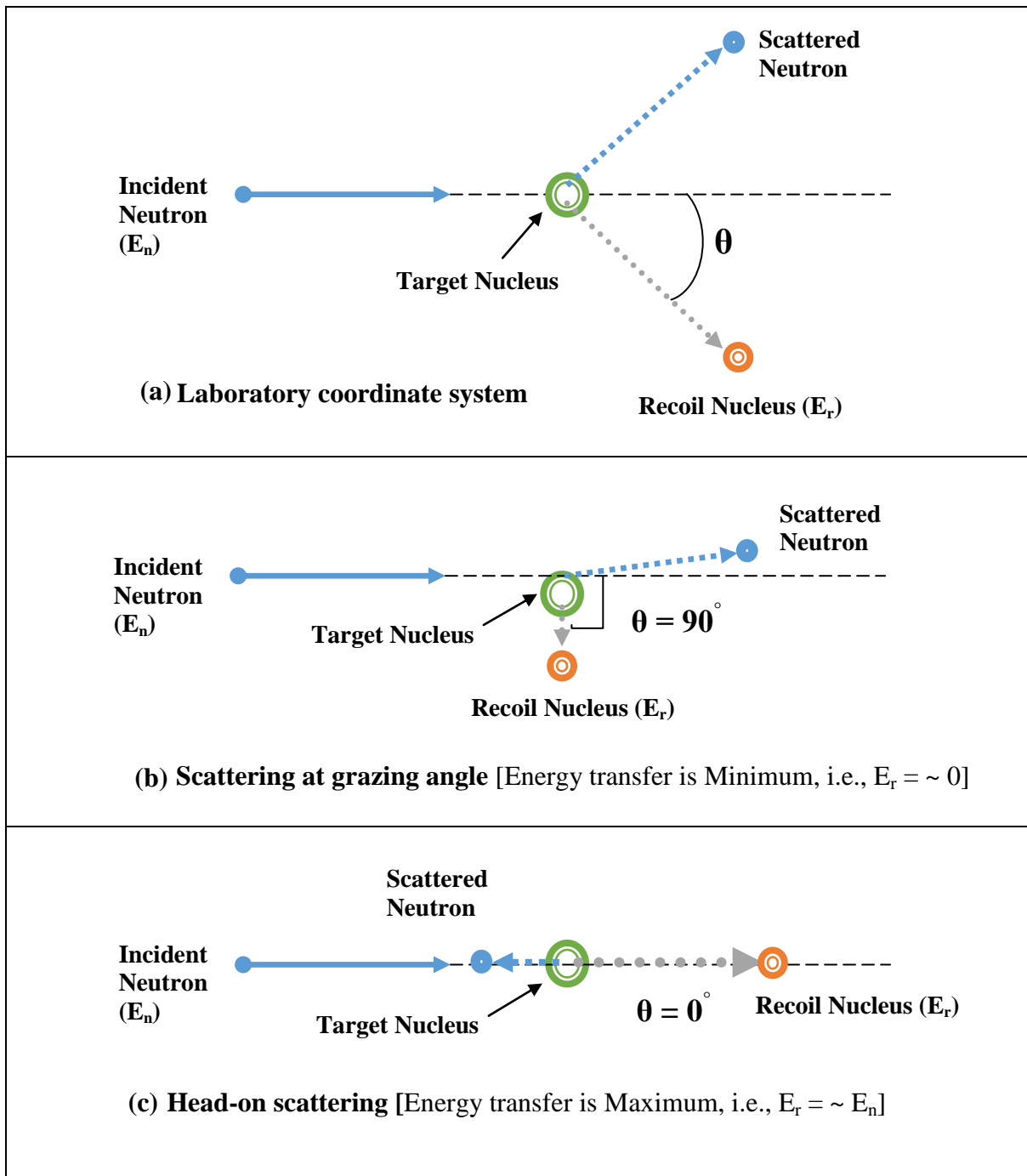
the incident neutron. From kinematics point of view, the energy transferred to the recoil nucleus ( $E_r$ ) of mass number  $A$ , undergoing a single collision with the incident neutron of energy ( $E_n$ ), is given by equation 2.1 in the laboratory coordinate system (see Figure 2.2 (a)) [6], [9], [60]:

$$E_r = E_n \left\{ \frac{4A}{(1+A)^2} \right\} \cos^2 \theta \quad (2.1)$$

where,  $\theta$  is the scattering angle (see Figure 2.2). It is evident from the expression that to get higher energy transfer from the incident neutrons to the recoil nucleus, a target with small  $A$  (or light nuclei) should be utilized. Therefore, during an elastic scattering interaction with hydrogen ( $A=1$ ), the energy transfer is maximum. Additionally, the recoil energy also depends on the scattering angle ( $\theta$ ). A neutron interaction at a grazing angle with the target nucleus in which neutron deflects only slightly, results in a recoil nucleus in almost perpendicular to the incident neutron direction (as shown in Figure 2.2 (b)), i.e., at  $\theta = 90^\circ$ . This situation corresponds to a minimum or no energy transfer to the recoil nucleus, i.e.,  $E_r = 0$ . A head-on collision of an incident neutron with the target nucleus leads to a recoil in the same direction (as shown in Figure 2.2 (c)), i.e., at  $\theta = 0^\circ$ . This situation results in a maximum energy transfer to the recoil nucleus and is given as:

$$E_{r_{max}} = E_n \left\{ \frac{4A}{(1+A)^2} \right\} \quad (2.2)$$

Hence, whenever an incident neutron undergoes a head-on collision ( $\theta = 0^\circ$ ) with the hydrogen atom ( $A=1$ ), the resultant recoil hydrogen nucleus, also known as *recoil proton*, will have maximum energy equivalent to the incident neutron energy ( $E_r = E_n$ ). The detectors which utilize this elastic scattering reaction with the hydrogenous material are often referred to as *proton recoil detectors*. The symbolic form to represent the elastic scattering interaction is:  $(n, n)$ .



**Figure 2.2 Neutron elastic scattering interaction diagram.**

During **inelastic scattering**, part of the incident neutron kinetic energy is given to the nucleus as excitation energy. After the collision, the excited nucleus immediately returns to the ground state by ejecting one or more  $\gamma$ -rays. The total kinetic energy, in this case, is not conserved. The total kinetic energy of the outgoing neutron and nucleus is less than the kinetic energy of the incoming neutron because part of the original kinetic energy is used to

place the nucleus into the excited state. A point worth to note here is that the inelastic scattering is not possible if all the excited state of the nucleus are at higher energy levels than the incident neutron energy. Since the hydrogen nucleus does not have an excited state, it would always undergo elastic scattering reaction. Symbolically, the inelastic scattering reactions can be represented as:  $(n, n')$ .

### 2.2.2 Absorption interaction

In the absorption reaction, the incident neutron is captured or absorbed in the target nucleus and one or more particles are emitted. Absorption reactions can be further subdivided into two main categories: radiative capture and non-radiative capture.

In **radiative capture**  $(n, \gamma)$ , the target nucleus captures the incident neutron and moves into an excited state. The excited nucleus decays abruptly emitting single or cascade of  $\gamma$ -rays.

In **non-radiative capture**, the target nucleus captures the incident neutron and emits one or more neutrons  $(n, 2n)$ ,  $(n, 3n)$ ; charged particles such as protons  $(n, p)$ , alpha  $(n, \alpha)$ , deuterons  $(n, d)$ , tritons  $(n, t)$ , etc. Majority of these interactions are endothermic, hence neutrons above specific threshold energies can only trigger them. However, there are few isotopes such as  $^3\text{He}$ ,  $^6\text{Li}$ ,  $^{10}\text{B}$ , and  $^{157}\text{Gd}$  that can endure exothermic interactions. Materials based on the aforementioned isotopes have the potential to be used as neutron detectors.

**Fission**  $(n, f)$  is another type of neutron interaction, which occurs when the neutron interacts with a heavy nucleus ( $Z \geq 92$ ). As a result of the fission due to neutron capture, fissioning compound nucleus splits into two smaller nuclei (known as *fission fragments*), along with the release of two or more free neutrons, few  $\gamma$ -rays, and neutrinos.

A summary of several interaction types is tabulated in Table 2.1.

**Table 2.1 Types of neutron interactions.**

Type (Nomenclature)	Nuclear Reaction
Elastic Scattering ( $n, n$ )	${}^A_ZX + n \rightarrow {}^A_ZX + n$
Inelastic Scattering ( $n, n'$ )	${}^A_ZX + n \rightarrow {}^A_ZX + n + \gamma$
Radiative Capture ( $n, \gamma$ )	${}^A_ZX + n \rightarrow {}^{A+1}_ZX + \gamma$
Charged Particle Emission ( $n, \alpha$ )	${}^A_ZX + n \rightarrow {}^{A-3}_{Z-1}X + \alpha$
Charged Particle Emission ( $n, p$ )	${}^A_ZX + n \rightarrow {}^A_{Z-1}Y + p$
Neutral Particle Emission ( $n, 2n$ )	${}^A_ZX + n \rightarrow {}^{A-1}_ZX + 2n$
Fission ( $n, f$ )	${}^A_ZX + n \rightarrow Y + Z + \gamma + n$

### 2.2.3 Neutron interaction cross-section

All the possible interactions of a neutron with the matter, discussed in the previous section, have a certain probability of occurrence which is generally explained through the concept of cross-section. The probability of a particular interaction ( $i$ ) between a neutron and a single nucleus is expressed by the microscopic cross-section ( $\sigma_i$ ). It depends on the target material (isotopes), type of interaction, incident particle and its energy. Its unit is barn ( $b$ ) ( $1 b$  equals to  $10^{-24} \text{ cm}^2$ ). An incident neutron may experience a variety of interactions while moving in a medium. Total cross-section is the sum of all the individual cross-sections:

$$\sigma_{total} = \sigma_{elastic} + \sigma_{n,\gamma} + \sigma_{n,n'} + \sigma_{n,2n} + \sigma_{n,\alpha} + \dots \dots \dots \quad (2.3)$$

The microscopic cross-section describes the neutron interaction with a single nucleus. However, in general, a neutron beam interacts with a thick sample which may contain several elements. Such scenarios can be explained by the macroscopic cross-section ( $\Sigma$ ) ( $\text{cm}^{-1}$ ), and it is expressed by equation (2.4):

$$\Sigma = N_i \cdot \sigma_i \quad (2.4)$$

where  $N_i$  is the atom density given as:

$$N_i = \rho \frac{N_A \cdot n_i}{M} \quad (2.5)$$

where,  $\rho$  is the density of the material ( $\text{kg/m}^3$ ),  $N_A$  is the Avogadro constant ( $N_A = 6.022 \times 10^{23}$  atoms/mol), and  $M$  is the molar mass of the material ( $\text{kg/mol}$ ).

Another important concept is the mean-free-path ( $\lambda = 1/\Sigma$ ), which represents the average distance traveled by neutron between two successive interactions. The  $\lambda$  depends on the type of material and energy of the incident neutron. After each interaction, the energy decreases, thereby changing the value of  $\lambda$ .

The relationship between energy ( $E$ ) and velocity ( $v$ ) of the neutron is expressed as:

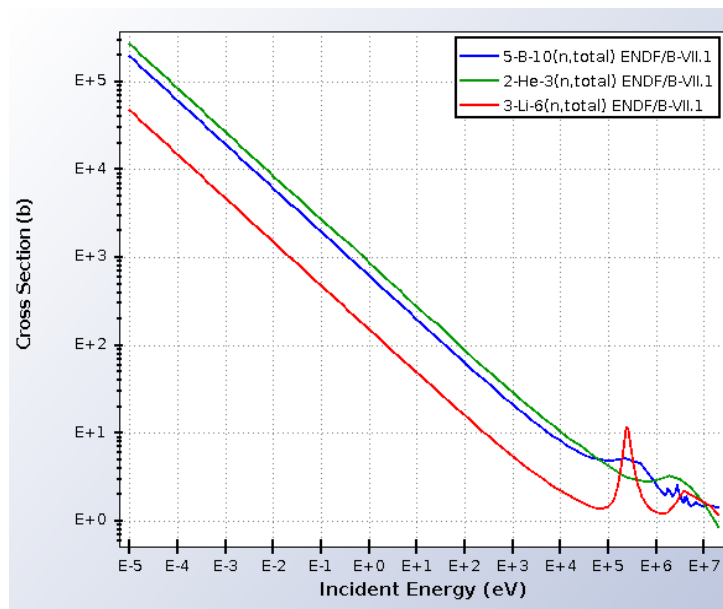
$$v = 1.383 \times 10^7 \cdot E^{1/2} \quad (2.6)$$

Fast neutrons of energy 1 MeV travel with a velocity of  $1.383 \times 10^7$  m/s whereas thermal neutrons (energy = 25 meV) traverse with a velocity of 2187 m/s. Therefore, thermal neutrons (slow neutrons) tend to spend more considerable time in the medium than the fast (high energy) neutrons. That is the reason why slow neutrons have a higher probability of interaction with the material in comparison to the fast neutrons. Figure 2.3 shows the typical neutron total cross-section plot for the  $^3\text{He}$ ,  $^{10}\text{B}$ , and  $^6\text{Li}$  isotopes. It can be observed that the cross-section generally decreases with neutron energy. As can be seen, the cross-section for the fast neutron is relatively quite low. Thus, the detection of fast neutrons is quite challenging in comparison to slow neutrons. Considering the neutron cross-sections, the detection of neutrons is subdivided into two groups viz., (a) slow neutron detection (b) fast neutron detection.

- **Slow or Thermal ( $E_n = 25$  meV) Neutron detection**

Slow neutrons have very small K.E., therefore they transfer very little energy to the target nucleus through elastic scattering reaction. The recoil nucleus will have very low energy to create significant ionization. Moreover, slow neutrons have comparatively higher cross-section for absorption reaction, which results in a secondary charged particle

generation. The K.E. of these charged particles depends on the reaction Q-value. These charged particles lose their K.E. through ionization mechanisms which in turn generate electron-hole or electron-ion pairs in the detector sensitive region. Now, these charge pairs are collected to form the detector signal. Table 2.2 lists out a few of the slow neutron converter materials of interest along with the secondary particles generated as a result of neutron interaction and their cross-sections. Note that these converter materials can be coupled with all the detector types such as gas-filled, scintillators or solid-state detectors (briefly explained in section 2.3) [9].



**Figure 2.3** Total neutron cross-sections for  $^3\text{He}$ ,  $^6\text{Li}$ , and  $^{10}\text{B}$  isotopes [62].

**Table 2.2** Converter materials for thermal neutron detection.

Thermal neutron reactions	Reaction Q-value (MeV)	Cross-section (barn)
$n + ^3\text{He} \rightarrow ^3\text{H} + p$	0.765	5330
$n + ^{10}\text{B} \rightarrow ^7\text{Li} + \alpha$ (6.3%)	2.79	3840
$n + ^{10}\text{B} \rightarrow ^7\text{Li} + \alpha$ (93.7%)		
$n + ^6\text{Li} \rightarrow ^3\text{H} + \alpha$	4.78	940
$n + ^{155}\text{Gd} \rightarrow ^{156}\text{Gd} + \gamma + e^-$	0.59	60791
$n + ^{157}\text{Gd} \rightarrow ^{158}\text{Gd} + \gamma + e^-$	0.54	255011



- **Fast Neutron detection**

Fast neutrons can be detected mainly by two methods viz., neutron moderation or elastic scattering interaction. In the first method, fast neutrons are moderated or slowed down to thermal energy region via elastic and inelastic scatterings with suitable moderator material; the resultant slow neutrons can then be detected by any slow neutron detection method. The second method relies on the relatively high cross-section of fast neutrons for elastic scattering reaction with hydrogenous (hydrogen-rich) materials. The fast neutrons generate recoil nucleus which is detected by any charged particle detector. For example, hydrogenous material HDPE generates recoil protons after elastic scattering reactions with fast neutrons. This method is popularly known as the recoil proton method.

#### **2.2.4 Charged particle interaction with matter**

Since, the detection of neutrons is indirectly recorded by the energy deposited by the charged particles in the detector active region. Hence, it is imperative to understand the mechanisms by which charged particle interacts and loses energy as it moves through matter. A charged particle traversing through matter can initiate processes such as: Coulomb interactions (ionization & excitation of atoms), emission of electromagnetic radiation (bremsstrahlung), emission of Cerenkov radiation and nuclear interactions. The ionization occurs, when the charged particle have enough energy to remove an electron. This results in a creation of ion pairs in surrounding matter. The excitation takes place when the electron acquires enough energy to move to an empty state in another orbit of higher energy. All these processes cause energy loss of the traversing particles. The relative contribution of these various processes to the total energy loss depends on the kinetic energy of the particle, the detector material, etc. For detailed understanding refs. [9], [61] may be referred.

### 2.3 TYPES OF NEUTRON DETECTORS

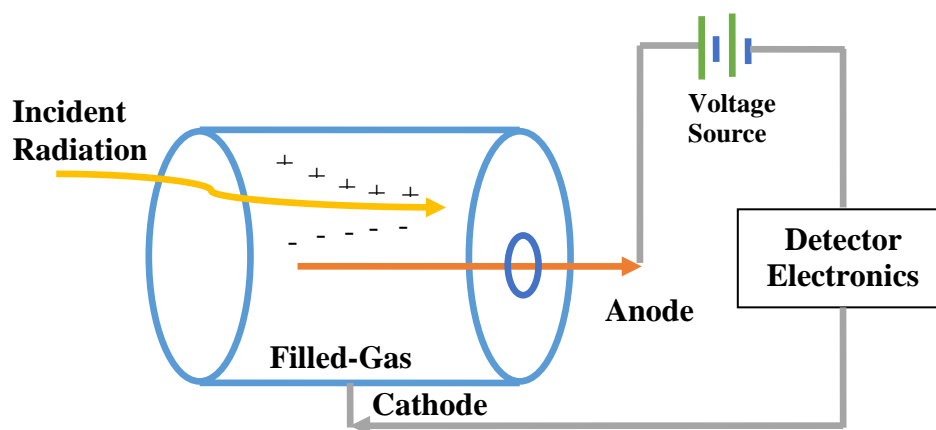
This section briefly explains three main categories of traditional radiation detectors.

#### 2.3.1 Gas-filled detectors

As the name suggests, these detectors are filled with noble gas which is ionized by the charged particles going through it. The gas-filled detectors consist of two electrodes (Figure 2.4) to which a specific voltage is applied. The ionizing radiation ionizes the gas atoms and creates electron-ion pairs which drift under the influence of the applied electric field. Their motion towards electrodes induces the electrical current in associated electronics which is further processed for counting purpose. Depending upon the region of operation, gas-filled detectors are divided in three types viz., ionization chamber, proportional counters, and gieger-müller (GM) counters. The ionization chambers are operated at low electric field such that no gas multiplication takes place. The current is independent of applied voltage. They are preferred for high radiation dose rates due to no dead-time. Proportional counters are operated at slightly higher voltage so that each ion pair produces an avalanche current. The output current pulse is proportional to the energy deposited by the radiation. GM counters are operated at even higher voltages so that each ion-pair create multiple avalanches which spread along the anode wire. GM tubes produce large output signal with minimal electronic processing.

In order to detect neutrons, a layer of neutron sensitive converter material (described in the previous section) is coated on the inner wall of the cylindrical chamber. The incident neutron interacts with the coated material and generates secondary charged particles. These charged particles now create ionization (electron-ion pairs) in the filled gas which is collected to indicate the presence of neutrons. These detectors are mostly used for neutron detection in nuclear applications because they are highly resistant to radiation-induced

damages, and offer high efficiency to thermal neutron detectors with good gamma-background discrimination [9]. Some major drawbacks include large dimension and requirement of the high voltage supply (order of hundreds of volts), and high pressure ( $\approx 10$  bar) for its operation. The purity of filled-gas, wall-effects, and space-charge effects are other major concerns for the gas-filled detectors [9].

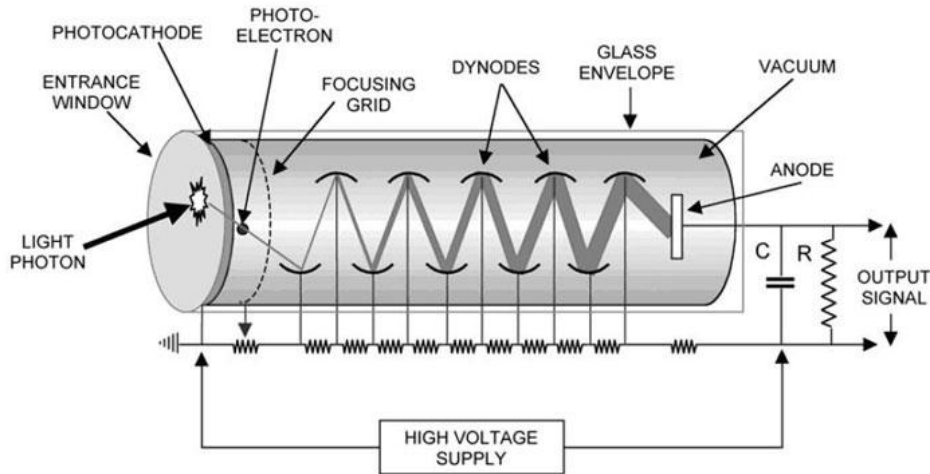


**Figure 2.4 Schematic diagram of a typical Gas-filled detector.**

### 2.3.2 Scintillation detectors

Scintillators are materials which generate scintillation of photons in the visible light range when the ionizing radiation passes through them. These materials can be of solid, liquid or gaseous type. The light emitted from the scintillator is minimal. Therefore, it is amplified with the help of a photomultiplier tube (PMT) as shown in Figure 2.5. Thermal neutrons can be detected by means of a nuclear reaction with  ${}^6\text{Li}$  nuclei by using  ${}^6\text{Li}$ -containing scintillation materials (loaded scintillators) such as  ${}^6\text{LiI}(\text{Eu})$  [9]. Fast neutrons can be detected by any organic (plastic or liquid) scintillators by means of elastic scattering [63]. The scintillation detectors have a wide range of applications. They offer a fast response (1–5  $\mu\text{s}$ ) than gas-filled detectors. However, scintillator detectors need PMT, a

delicate instrument which requires a well-regulated power supply of hundreds of volts and whose response is also affected by magnetic fields present in the application field [9].



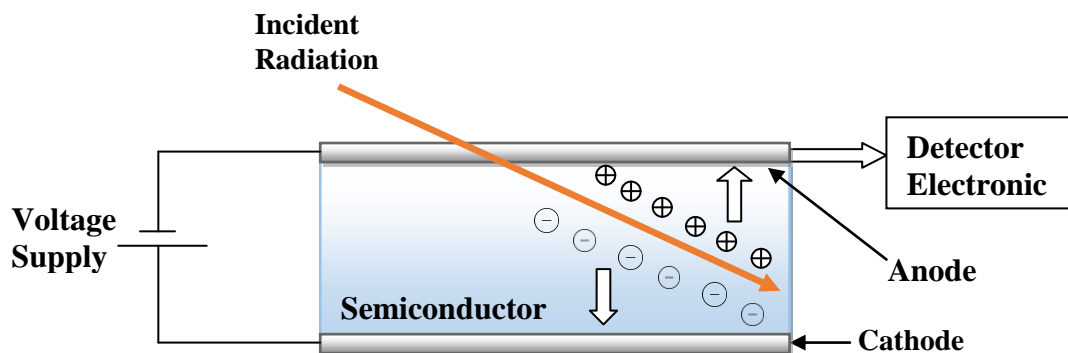
**Figure 2.5 Schematic diagram of a scintillation detector with PMT setup [64].**

### 2.3.3 Semiconductor Detectors

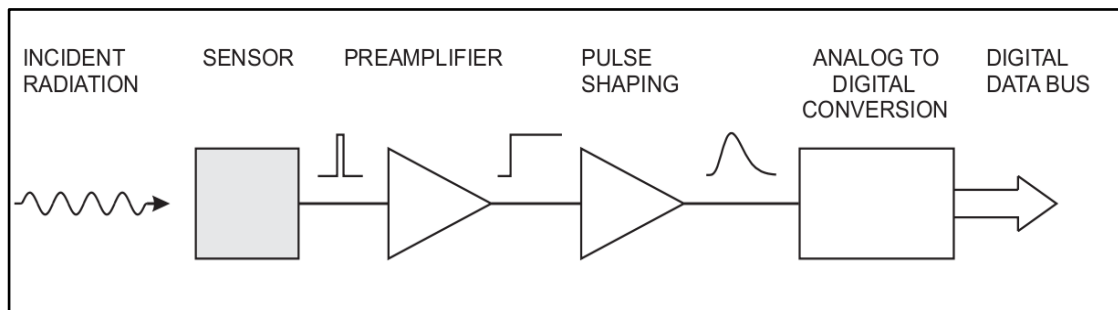
Semiconductor detectors (SDs) are solid-state devices which operate in the same manner as ionization chambers. The charge carriers in SDs are electron-hole pairs instead of electron-ion pairs. Since the density of the solid-state material is high, they can entirely stop the ionizing radiation in a much smaller volume than required by gas-filled detectors. Hence, these detectors are very compact in size. Majority of the SDs are based on Si or Ge materials. In the past decade or two, several other semiconductor based detectors are successfully studied, e.g., cadmium telluride (CdTe), cadmium zinc telluride (CdZnTe), often named CZT, etc., [65], [66].

A SD is generally used in the form of the p-n junction, a p-i-n diode (PiN) or Schottky barrier diode (SBD) in reverse bias mode. In reverse bias, a specific region below the anode contact of the diode becomes depleted of charge carriers and called as depletion region or space-charge region (SCR). The width of the depletion region depends upon the applied external reverse bias voltage. When ionizing radiation passes through a semiconductor, it

ionizes the matter, thereby creating free electron-hole pairs (EHPs). The total number of EHPs created is proportional to the energy transmitted by the radiation to the semiconductor. These EHPs drift towards the respective electrodes and induce image charges on the electrodes which are amplified and processed by associated detector electronics to provide the detector response [67]. The operation of a typical semiconductor detector is illustrated in Figure 2.6 and a typical schematic of the detector electronics is shown in Figure 2.7. The SDs are basically a very high resolution charged particle and photon detectors. In the recent past, several semiconductor based neutron detector prototypes have been developed. The semiconductor-based neutron detectors can be classified into two groups:



**Figure 2.6 Schematic of a semiconductor diode detector.**

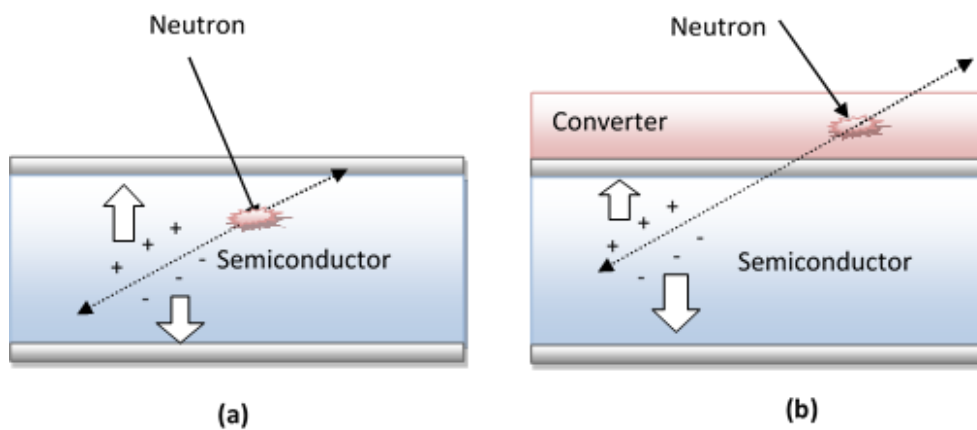


**Figure 2.7 Schematic of detector electronics.**

Semiconductor sensor generates a small electrical signal after capturing the incident radiation. This low-level electrical signal is amplified in pre-amplifier; shaped in pulse shaper and then digitized for storage and further analysis [67].

- **Direct-conversion or bulk neutron detectors**

These are the detectors whose bulk semiconducting material is itself sensitive to the neutrons, e.g., GaAs, CZT, Diamond,  $\text{UO}_2$ ,  $\text{B}_x\text{C}$ , etc., [66]. A typical schematic of a direct conversion neutron detector is shown in Figure 2.8 (a). Neutron directly interacts with the nucleus of the bulk material and generates recoil nucleus or secondary charged particles, which further lose their energy in the detector active (depletion) region to generate the detector signal. This kind of detectors could be highly efficient. However, semiconductors having a large amount of neutron sensitive isotopes, are rare and they suffer from poor charge collection properties [68].

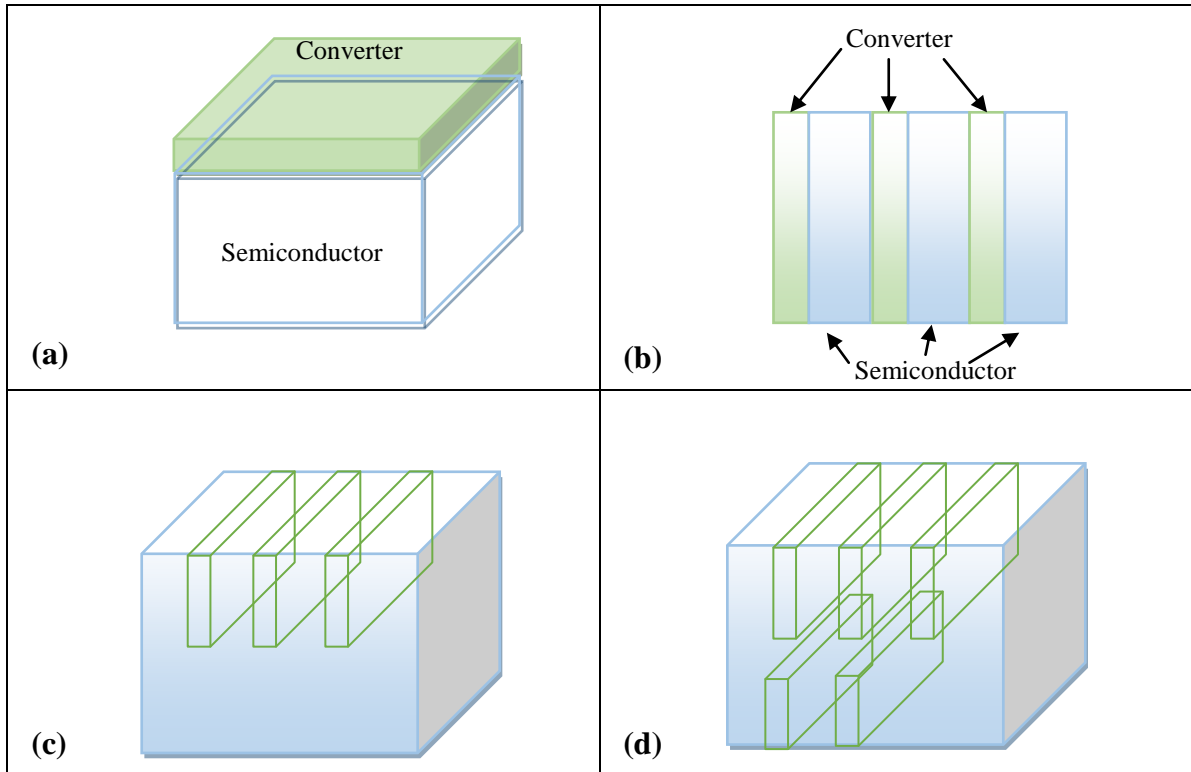


**Figure 2.8 Representation of (a) Direct (b) Indirect-Conversion Neutron Detectors.**

- **Indirect-conversion neutron detectors**

The indirect conversion semiconductor detectors (as shown in Figure 2.8 (b)) have an additional coating of a neutron sensitive converter material. The incident neutrons interact with the coated neutron sensitive converter and generate secondary charged particles which in turn create e-hole pairs in the semiconductor depletion region to provide the detector signal. A planar and few 3D structures of indirect configuration neutron detector are shown in Figure 2.9 [68]. A point to note here is that the planar structure of SDs is matured while

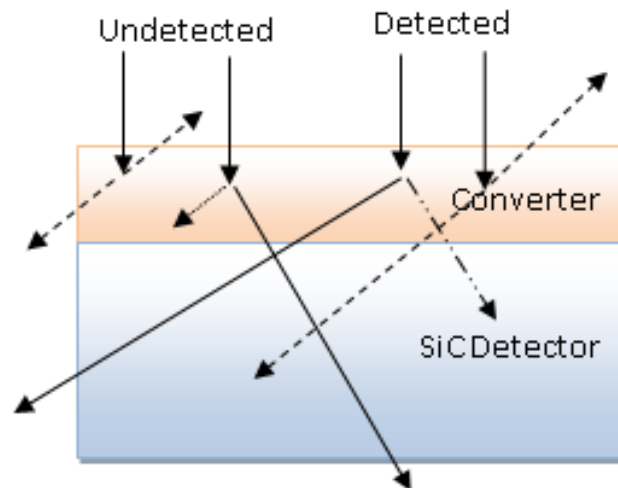
several 3D structures are still under theoretical investigation as they pose a severe challenge in terms of fabrication and efficient charge collection.



**Figure 2.9** Schematic of the (a) planar structure of SD; few 3D structures (b) Stacked SD (c) single side trench structure (d) double side trench structure [68].

The planar and stacked structure of the indirect-conversion SiC-based semiconductor neutron detector has been studied in this work. The planar structure has an inevitable geometrical limitation because the probability of neutron interaction in a planar structure depends strongly on the thickness of the neutron sensitive converter layer. The probability of the neutron interaction increases with the thickness of the converter layer, but at the same time, it reduces the probability of resultant secondary charged particles to reach the active (depletion) region of the SD (due to continuous energy loss in the matter, also known as self-absorption). A careful observation reveals that, in planar structure, not all the secondary charged particles are able to reach the depletion region of the SD as some of the low energy are absorbed within converter and few others are leaving the converter from sides, i.e., unable to reach depletion region of the semiconductor (depicted in Figure 2.10).

Therefore, for each converter material, there is an optimum thickness at which maximum number of reaction products would reach in the SD's depletion region. The optimum thickness of the converter is not feasible to determine through experiments. Hence, Monte-Carlo simulations have been performed to find the optimum thickness for several neutron sensitive converter materials.



**Figure 2.10 Sketch of planar SD illustrating various possibilities of secondary charged particles movement which reflects whether the neutron is detected or undetected.**

Note: Dashed lines indicate the track of charged particles or recoil proton whereas continuous line represents neutron tracks.

After understanding the role of converter material, it is prudent to specify the important characteristics of a neutron sensitive converter material:

- The converter should be made up of isotopes or compound material having a high percentage of those isotopes that captures neutrons.
- It should have a high neutron cross-section for the energy range of interest.
- Converter which emits charged particles such as  $(n, \alpha)$ ,  $(n, p)$  should be preferred over those which emit uncharged particles like  $(n, 2n)$ ,  $(n, \gamma)$  because it is easier to detect charged particles.
- The energy of generated charged particles should be sufficiently high to cross the converter and deposit sufficient energy in the detector active region.



## 2.4 METAL-SEMICONDUCTOR (M-S) JUNCTION

A M-S junction can be rectifying (Schottky contact) or non-rectifying (ohmic contact). In this work, SiC has been used in the form of a SBD. Therefore, it is essential to understand the Schottky contact formation and current transport mechanism through it. It should be noted that, the theory is briefly described considering *n*-type SiC SBD. For detailed understanding, semiconductor textbooks should be referred [69]–[72].

### 2.4.1 Schottky contacts

Schottky contacts allow conduction of current in one direction but blocks it in the other direction. Figure 2.11 (a) shows the energy band diagrams of metal and SiC semiconductor material before making any contact. When the metal is brought into contact with the semiconductor, electrons in the high energy states of the semiconductor flow into the lower energy states of the metal until the Fermi level becomes a constant throughout the system, i.e., until the thermal equilibrium (zero bias) condition is achieved. Also, the metal work-function ( $\Phi_M$ ) should be different than the semiconductor work-function ( $\Phi_S$ ) (for *n*-type semiconductor  $\Phi_M > \Phi_S$  and vacuum level must be continuous across the interface. The above requirements results in a unique energy band diagram (as shown in Figure 2.11 (b)) for an ideal M-S contact where interface states\* are absent. The electrons that flow into the metal leave behind the positively charged donor atoms in the semiconductor, creating a space charge region or depletion region. The excess electrons in the metal side and positive ionized donors in semiconductor create electric field from semiconductor to metal. The alignment of the Fermi level results in a Schottky barrier height ( $\phi_B$ ) on the metal side and a built-in potential ( $V_{bi}$ ) on the semiconductor side. Schottky barrier height (SBH) is the barrier seen by electrons in the metal trying to move

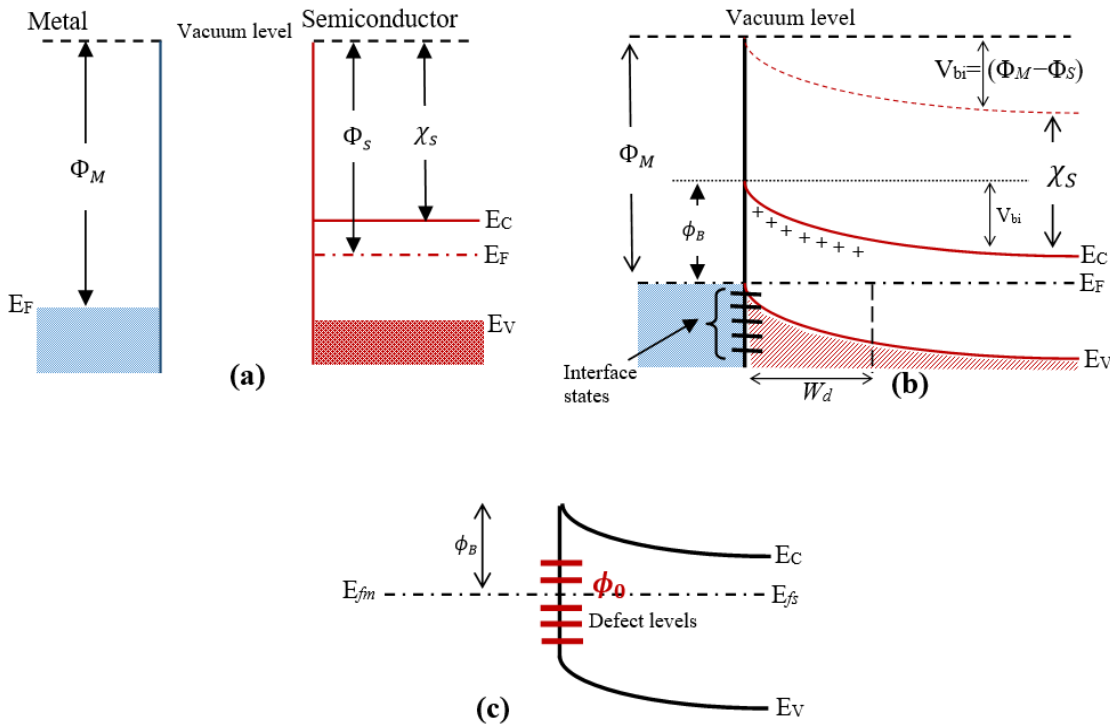
---

\* Interface states are present between the metal-semiconductor boundaries. They arise from many kinds of defects such as broken/dangling bonds at the semiconductor surface.

into the semiconductor, and is ideally given by:

$$\phi_B = \Phi_M - \chi_S \quad (2.7)$$

where,  $\chi_S$  is the energy difference between the conduction band edge  $E_c$  and the vacuum level known as electron affinity of the semiconductor. Ideally, the SBH depends on the metal and semiconductor properties as evident from equation (2.7). However, in case of practical M-S contact, the SBH is independent of the metal due to the interface states present between the M-S boundaries. These states are continuously distributed in energy within the forbidden gap ( $E_g$ ), as shown in Figure 2.11 (c).



**Figure 2.11 Energy band diagram of metal n-type semiconductor contact with  $\Phi_M > \Phi_S$ .**  
 (a) When two materials are isolated from each other (b) thermal equilibrium condition after the contact is made. (c) Fermi level pinning due to interface states.

These states pinned down the Fermi level ( $E_f$ ) at the surface, and thus the SBH will be independent of metal work function and is given by:

$$\phi_B = E_g - E_f \quad (2.8)$$

Most of the M-S contacts do have the interface states, but they are not large enough to be pinned down to the Fermi level. Thus, the SBD will be affected by both the metal work function as well as the interface states. Most of the metals deposited on the SiC, work as Schottky contact provided SiC is not heavily doped and high-temperature (>700 °C) contact sintering is not performed [29]. In SiC, the SBH is found to be dependent on the SiC polytype, the metal, the surface condition before contact formation and the interfacial chemistry. The work-function of some metals used for Schottky contact on SiC is tabulated in Table 2.3.

**Table 2.3 Work-function of several metals for Schottky contact formation on SiC [73].**

Metal	Mg	Mn	In	Ag	Al	Ti	Mo	Cu	Au	Pd	Ni	Pt
$\Phi_M$ (eV)	3.65	4.15	4.20	4.25	4.28	4.33	4.6	4.65	5.1	5.12	5.15	5.65

Apart from the presence of interface states, SBH can also be modified by the Coulomb attraction between the electron and its image charge in the metal, known as an image force lowering. The magnitude of the image force lowering ( $\Delta\phi_{bl}$ ) is expressed as [70], [71]:

$$\phi_{bl} = \sqrt{\frac{qE}{4\pi\epsilon_s}} \quad (2.9)$$

where  $E$  is electric field,  $q$  is electron charge and  $\epsilon_s$  is image force permittivity.

#### 2.4.2 Ohmic Contacts

Ohmic contact is a non-rectifying contact which allows free-flow of charge carriers in both the directions. Ohmic contacts are also significant from the semiconductor device operation point of view. Ohmic contacts have negligible contact resistance compared to total device resistance [70]. For M-S contact to achieve very low contact resistance, it must have either a small barrier height or very high doping density (with an increase in doping,

contact resistance decreases exponentially) or both [70]. It is difficult to produce a small barrier height as it depends on several factors as explained in the previous section. Therefore, Ohmic contacts are fabricated using highly doped semiconductors to achieve this low contact resistance.

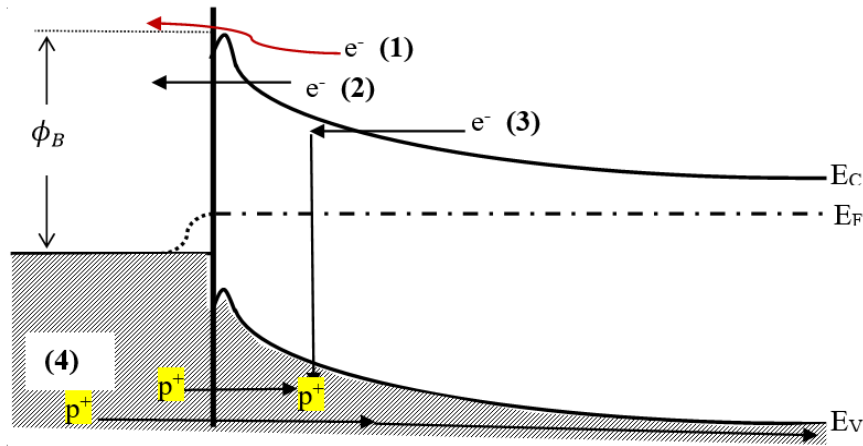
### 2.4.3 Current transport mechanism

In M-S junctions, majority carriers are predominantly responsible for the current transport, unlike p-n junctions, where minority carriers are also accountable for the flow of current. The majority carriers can either be electrons (for *n-type* semiconductors) or holes (for *p-type* semiconductors) [70]. Four mechanisms contribute to the current transport across M-S interface [26], [70], [71]:

- i. ***Thermionic Emission (TE)***: The emission of electrons over the Schottky barrier from the semiconductor into the metal. TE is dominant for lightly doped semiconductors.
- ii. ***Quantum mechanical tunneling***: It is dominant for highly doped semiconductors such that the barrier is sufficiently thin. Tunneling can be ‘pure’ tunneling, i.e., field emission (FE) at low temperatures when electrons' energies are close to the Fermi level or thermionic field emission (TFE) at high temperatures when electrons are excited to levels where barrier is sufficiently thin for tunneling to occur [70], [72].
- iii. ***Carrier recombination and generation*** in the depletion region, and
- iv. ***Hole injection from the metal to the semiconductor*** (recombination in the neutral region).

These transport mechanisms are illustrated in Figure 2.12. In the case of wide bandgap semiconductors such as SiC, the thermionic emission and tunneling of electrons over the Schottky barrier contribute dominantly to the current density. If the SiC material is lightly doped and the operating temperature is not very low, the thermionic emission (TE)

current will be dominant. The tunneling component will only be significant if the SiC is heavily doped and the device is operating in a low-temperature environment. Under reverse bias operation, the tunneling current term contributes significantly.



**Figure 2.12 Basic current transport mechanisms across the M-S junction.**

(1) Thermionic emission, (2) Tunneling, (3) Recombination, (4) Diffusion of holes, [26], [27], [70], [71].

#### 2.4.4 Current-Voltage ( $I$ - $V$ ) relationship

The current conduction in the Schottky diode is mainly due to the majority carriers and can be explained by the *thermionic emission* (TE) theory [70]. The current density of the Schottky diode at forward and reverse bias can be expressed by the relation:

$$J = J_s \left[ \exp \left( \frac{qV}{\eta kT} \right) - 1 \right] \quad (2.10)$$

where  $q$  is electron charge,  $V$  is forward bias voltage,  $\eta$  is ideality factor,  $k$  is Boltzmann constant,  $T$  is temperature (in Kelvin), and  $J_s$  is the reverse saturation current density derived from the straight line fitting of the equation (2.10) at zero biasing and given by equation (2.11):

$$J_s = A^* T^2 \exp \left[ \frac{-q(\phi_B - \Delta\phi_{bl})}{kT} \right] \quad (2.11)$$

where  $\phi_B$ ,  $\Delta\phi_{bl}$ , and  $A^*$  is the barrier-height (BH), image-force lowering and Richardson constant, respectively. The value of  $A^*$  for 4H-SiC is  $146 \text{ A-cm}^{-2}\text{-K}^{-2}$  [74]. The ideality factor ( $\eta$ ) explains the deviation of  $I$ - $V$  characteristics from the TE theory and can be expressed by rearranging the equation (2.10) as:

$$\eta = \frac{q}{kT} \left( \frac{dV}{d(\ln J)} \right) \quad (2.12)$$

For the ideal diode, the value of  $\eta$  is 1, but for the practical diodes, its value is greater than 1. The semi-log plot of  $J$ - $V$  curve (i.e.,  $\ln(J)$  vs.  $V$  plot) at lower forward bias gives a straight line. The slope of this linear region  $\{d(\ln(J))/dV\}$  is used to predict the ideality factor of the diode. The intercept of this linear region with the Y-axis provides value of  $\ln(J_s)$ . The Schottky barrier-height ( $\phi_B$ ) can be estimated from the equation (2.13) using the value of  $J_s$  obtained from the intercept of  $\ln(J)$ - $V$  plot.

$$\phi_B = \frac{kT}{q} \left[ \ln \left( \frac{A^* T^2}{J_s} \right) \right] \quad (2.13)$$

It should be noted that the value of  $\phi_B$  estimated from the  $J$ - $V$  curve is only reliable if the forward bias plot of  $\ln(J)$  vs.  $V$  is linear with a low value of  $\eta$ . To determine the series resistance ( $R_s$ ), the model given by Cheung and Cheung [75] is used. The slope of the  $dV/d(\ln(I))$  vs.  $I$  curve gives the  $R_s$ .

### 2.4.5 Capacitance-Voltage (C-V) relationship

Few critical device parameters such as built-in-potential ( $V_{bi}$ ), effective carrier density ( $N_{eff}$ ), Fermi energy ( $E_f$ ), image-force lowering ( $\Delta\phi_{bl}$ ) are estimated from the  $C$ - $V$ -characteristics. In reverse bias SBD, the depletion or space charge region (SCR) formed at Schottky metal and semiconductor interface acts as a voltage dependent capacitor ( $C=dQ/dV$ ). The reverse bias junction capacitance can be expressed as [70]:

$$C = A \sqrt{\frac{q\epsilon_s\epsilon_0 N_d}{2(V_{bi} + V_R)}} \quad (2.14)$$

where  $A$ ,  $\epsilon_s$ ,  $\epsilon_0$ ,  $N_d$ , and  $V_R$  is the area of Schottky contact, dielectric constant, the permittivity of vacuum ( $\epsilon_0 = 8.85 \times 10^{-14}$  F/cm), doping concentration, and reverse bias voltage, respectively. Equation (2.14) can be rewritten as:

$$\frac{1}{C^2} = \frac{2(V_{bi} + V_R)}{q\epsilon_s\epsilon_0 N_d} \quad (2.15)$$

It shows that the inverse squared capacitance is the linear function of the applied reverse bias voltage [70]. The intercept at the voltage axis of the  $\{(1/C^2) \text{ vs. } V\}$  plot provides the value of  $V_{bi}$ , whereas the slope of the linear curve is used to determine the doping concentration ( $N_d$ ) of the diode epitaxial layer using equation (2.16):

$$N_d = \frac{2}{q\epsilon_s\epsilon_0} \left( \frac{1}{\text{slope}} \right) \quad (2.16)$$

Using the values of  $V_{bi}$  and  $N_d$ , the barrier height ( $\phi_{BC-V}$ ),  $E_f$ ,  $\Delta\phi_{bl}$ , effective carrier density ( $N_c$ ) and depletion width ( $W_d$ ) can be estimated by the following relations:

$$\phi_{BC-V} = V_{bi} + E_f - \Delta\phi_{bl} \quad (2.17)$$

$$E_f = \frac{kT}{q} \ln \frac{N_c}{N_d} \quad (2.18)$$

$$N_c = 4.82 \times 10^{15} T^{3/2} (m_e^*/m_0)^{3/2} \quad (2.19)$$

where  $m_e^*$  is the effective mass of electron and  $m_0$  is the rest mass of electron ( $m_e^* = 0.42m_0$ ).

$$\Delta\phi_{bl} = \sqrt{\left( \frac{qE}{4\pi\epsilon_s} \right)} \quad (2.20)$$

$$W_d = \sqrt{\frac{2\epsilon V_{bi}}{qN_d}} \quad (2.21)$$

### 2.5 DEFECTS IN SEMICONDUCTORS

Defects in semiconductors can be defined as any form of imperfection or deviation from a perfect crystal lattice. As a matter of fact, a perfect semiconductor crystal is impossible to produce due to several reasons that include wafer production, growth methods, and device processing. Defects are also introduced intentionally as a donor impurity into the semiconductor to modify the conductivity of the semiconductor device. Defects can be categorized as intrinsic and extrinsic defects. A defect is of intrinsic type if the defective volume is composed of the same atoms as the undisturbed crystal lattice. If foreign atoms, such as doping impurities, take part in the defect, the defect is said to be of extrinsic character. Intrinsic defects are point defects (0-dimension), line defects (1-D), plane defects (2-D) and volume defects (3-D). The subsequent subsections are focused on the defects in SiC. For detailed description refs. [26], [27], [72], [76] can be followed.

#### 2.5.1 Primary Defects

Primary defects can be classified into two categories, namely, point defects and extended defects. Point defects are not extended in space in any dimension, and this implies that the perturbation of the lattice is localized about a lattice site and involves only a few nearest neighbors. On the other hand, extended defects are extended in nature (such as grain boundaries, dislocations or stacking faults) [76].

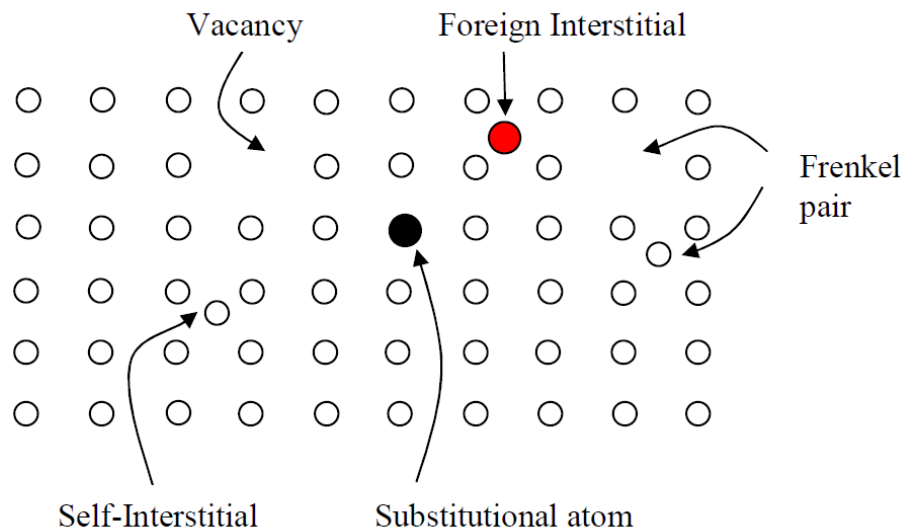
Point defects can be further sub-divided as:

- i. **Vacancy:** An atom is missing from its original lattice position. The vacancy in SiC can either be silicon vacancy,  $V_{Si}$  (there is no atom on a silicon lattice site) or carbon vacancy,  $V_C$  (there is no atom on a carbon lattice site).



- ii. **Interstitial:** An atom that inhabits a position different from its regular site. Interstitials can be classified as self-interstitials (i.e., if the atom is the same as one of the species of the host lattice), or an interstitial impurity (i.e., if the interstitial atom is a different species from the host atoms). In SiC, a self- interstitial can either be silicon,  $\text{Si}_i$  or carbon,  $\text{C}_i$ .
- iii. **Frenkel pair:** A self-interstitial atom is located close to a vacancy.
- iv. **Antisite:** In compound semiconductors, an atom of one sub-lattice is positioned in a lattice site of the other element, e.g., in SiC, when Si takes the lattice position of C (a silicon antisite,  $\text{Si}_\text{C}$ ) or C is on a Si lattice point (a carbon antisite,  $\text{C}_\text{Si}$ ).
- v. **Substitutional impurity:** A foreign atom that occupies a lattice site, e.g., a nitrogen atom on a C site ( $\text{N}_\text{C}$ ).

Point defects are shown schematically in Figure 2.13.



**Figure 2.13** The schematic diagram of point defects in semiconductors, taken from [76].

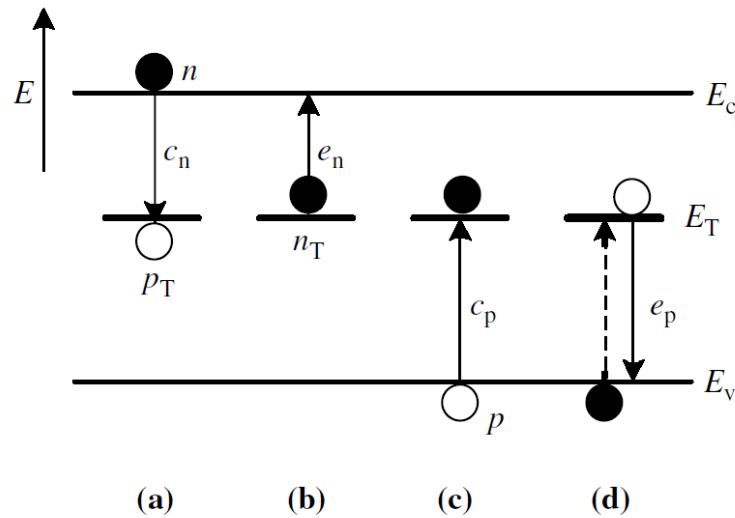
### 2.5.2 Secondary defects

Due to high-energy particle irradiation, primary defects such as vacancy ( $V$ ) and self-interstitial ( $I$ ) are created in semiconductors. The primary defects are mobile at low

temperatures. The  $V$  and  $I$  which survive the recombination can diffuse into the semiconductor and interact with other intrinsic and extrinsic defects which results in another complex room temperature stable defects such as *A-center*, *E-center*, *divacancy*, etc. The removal of two neighboring atoms forms the divacancy ( $V-V$ ). The *E-center* can be described as a vacancy trapped next to a substitutional donor atom. The *A-center* ( $V-O$ ) may be regarded as a vacancy trapped next to an oxygen atom in an interstitial position.

Most of the primary and secondary defects discussed above are electrically active and introduce electronic states in the band gap of semiconductors, which can be classified as *shallow levels* and *deep-levels* [29], [76]. Shallow levels are those defects whose states are located near the band edges (near valence band for acceptor type levels and near conduction band for donor type levels). Deep levels are those defects which are positioned deeper in the band gap [26]. Deep-levels can be described as an electron trap, a hole trap, a recombination center or a generation center, depending on the nature of the electron and hole interactions that happens between the deep-levels and the conduction and valence bands. Figure 2.14 illustrates the possible interactions that can take place between the bands and the deep levels through the emission and/or capture of charge carriers. The possible interactions are:

- a) a deep level can capture an electron from the conduction band with capture rate  $c_n$  after which any of two interactions (b) or (c) may occur,
- b) the deep level can either emit the electron back to conduction band with emission rate  $e_n$ , or
- c) it can capture a hole from the valence band with capture rate  $c_p$
- d) After hole capture, again two interactions are possible: either the hole can be emitted to the valence band with emission rate  $e_p$ , or an electron can be captured from the conduction band (i.e., process (a) follows).



**Figure 2.14** The schematic diagram of different carrier transitions between deep-levels and the energy bands.

(a) Electron capture, (b) electron emission, (c) hole capture, and (d) hole emission [72]. The subscript 'T' stands for traps. Trap centers occupied by electrons are  $n_T$  and occupied by holes are  $p_T$ . The total density  $N_T = n_T + p_T$ .

An electron trap is a deep level for which the  $c_n$  is much higher than the  $c_p$  and vice-versa for a hole trap ( $c_p \gg c_n$ ). If  $c_n \approx c_p$  then the deep level is recombination center. From Figure 2.14, a recombination event is the combination of processes (a) and (c), and a generation event is (b) and (d). A defect where these processes occur is called a generation-recombination center.

Deep levels can either be beneficial or detrimental to device operations, depending on their applications. Thus, the study of deep levels is of paramount importance in the semiconductor device industry so that those deep levels which are useful can be deliberately added and those that are detrimental can be reduced or eliminated.

The deep-levels and their associated properties (signatures) are studied using several techniques such as Deep Level Transient Spectroscopy (DLTS), Thermally Stimulated Current (TSC), Thermally Stimulated Capacitance (TSCAP), Photo-induced Transient Spectroscopy (PITS), etc., whose descriptions are beyond the scope of this thesis.

### 2.5.3 Defects in SiC

This subsection gives a brief account of defects that are reported to be found in 4H-SiC. Epitaxial layers grown on off-axis {0001} SiC substrates exhibit several types of surface defects such as carrot defect, triangular defect, and downfall [29]. When SiC devices include carrot or triangular defects, the devices exhibit excessive leakage currents and significantly decreased breakdown voltages [77]. Another type of defect is *Micropipes*. Micropipes are basically a hollow core penetrating the entire wafer along the c-axis\* direction. Placing any device directly on top of the micropipe is bound to cause failure. Micropipes may be caused by several screw dislocations† bunching together to form a giant screw dislocation, making it energetically favorable to open up a hollow core in the center. Nevertheless, substrates are commercially available with zero or  $\sim 1$  micropipe density/cm<sup>2</sup> [78], [79]. Stacking faults (SFs) are another kind of defects that exist in SiC. SFs occur due to the deviation of Si–C bilayers from the perfect stacking sequence along the c-axis of the crystal. SFs reduce the barrier height and the breakdown voltage of a Schottky diode [80].

Deep-levels are observed in *as-grown* and irradiated *n*-type 4H-SiC. They exist at specific energy levels ( $E_t$ ) within the band gap region. They capture the created charge carriers (electrons or holes) and immobilize them for a period of time or even neutralize them completely. The trap energy level ( $E_t$ ) for specific carrier traps is referred as relative to the band energy. So, for electron trapping,  $E_t$  is given with reference to the conduction energy band as: ( $E_c - E_t$ ) and for hole trapping,  $E_t$  is given with respect to the valance band as: ( $E_v + E_t$ ). Two dominant deep-levels are widely reported in 4H-SiC: the  $Z_{1/2}$  [81] ( $E_c - 0.68$  eV) and the  $EH_{6/7}$  [82] ( $E_c - 1.65$  eV) with densities  $\sim 10^{13}$  cm<sup>-3</sup>. Both defects are extremely stable against high-temperature ( $\sim 1700$  °C) annealing. They are related to the

---

\* For hexagonal structures, four principal axes are commonly used  $a_1$ ,  $a_2$ ,  $a_3$  and  $c$ . The three  $a$ -vectors (with  $120^\circ$  angle between each other) are all in the close-packed plane called  $a$ -plane, whereas the  $c$ -axis (0001) is perpendicular to this plane.

† Screw dislocations formed when atoms are arranged in a helical pattern normal to the direction of stress.

Carbon vacancy [83]. In the lower half of the band-gap, the HK2 ( $E_V + 0.84$  eV), HK3 ( $E_V + 1.24$  eV) and HK4 ( $E_V + 1.44$  eV) [84] centers are dominant deep levels. The densities of HK2, HK3 and HK4 centers are typically in the range  $(1-4) \times 10^{12} \text{ cm}^{-3}$ . The origins of these defects are related to the defect complexes including carbon displacement. Since, the HK2, HK3, and HK4 centers almost disappear upon annealing at 1450–1550 °C [84], the  $Z_{1/2}$  and  $EH_{6/7}$  centers are more important. Indeed, the  $Z_{1/2}$  center has been identified as the dominant lifetime killer, at least for n-type 4H-SiC [85]. After irradiation of 4H-SiC with electrons, some new deep-levels are observed in addition to the increase in the concentration of the existing deep-levels ( $Z_{1/2}$  and  $EH_{6/7}$ ). These deep-level centers are referred to as EH1 ( $E_C - 0.45$  eV), EH2 ( $E_C - 0.68$  eV), EH4 ( $E_C - 0.72$  eV), EH5 ( $E_C - 1.15$  eV), EH6/EH7 ( $E_C - 1.65$  eV) and HH1 ( $E_V + 0.35$  eV) [82], [86]. Following the neutron irradiation, deep-levels ( $E_C - 0.5$  eV,  $E_C - 0.24$  eV, and  $E_C - 0.13$  eV) were observed in 4H-SiC [29], [56]. The list is too exhausting to present here. For extensive details a review of deep levels in SiC by Lebedev *et al.*, [87] may be referred.

#### 2.5.4 Effects of irradiation induced defects

Irradiation-induced defects in the semiconductors may alter the lifetime of charge carriers by trapping them in the various trap centers, which in turn affects the device operation. After heavy irradiation, deep-levels sometimes bring about redistribution of charge carriers and a change in the conductivity of the material. If a material with *n*-type conductivity is irradiated, electrons are transferred from the conduction band to deep levels of acceptor-type radiation defects. As a result, the conductivity of the material decreases, and the semiconductor becomes an insulator (also known as doping compensation). The removal rate for charge carriers ( $\eta_r$ ) is defined as:

$$\eta_r = \Delta n / \Phi_F = (N_0 - N_T) / \Phi_F \quad (2.22)$$

where  $N_0$  and  $N_T$  are the concentrations of charge carriers in the conduction band before and after irradiation and  $\Phi_F$  is the radiation dose/fluence.

Several studies have been performed to determine the deep-levels in 4H-SiC after various particle irradiations. However, there are very few works which report on the electrical behavior of the SiC which is subjected to irradiation. They are also limited in terms of dose or fluence as practically it is difficult to assess the device performance after several fluence/doses of irradiation. Therefore, in this work, we have modeled the SiC-based SBD in a device simulation tool, i.e., TCAD from Silvaco and studied the electrical characteristics of the device subjected to increasing radiation fluence.

## 2.6 SUMMARY

The neutron interaction with matter is discussed in this chapter. The working principle of gas-filled, scintillators and semiconductor detector is briefly explained. Important characteristics of the neutron sensitive converter materials for the development of indirect conversion semiconductor neutron detector are highlighted. The physics of the Schottky diode behavior is also outlined. Several types of defects which are found in semiconductors are also discussed with special emphasis on the deep-levels found in SiC.

\*\*\*\*\*

# 3

## MODELING TOOLS

---

### 3.1 PREAMBLE

This chapter introduces the state-of-the-art Modeling & Simulation (M&S) tools used for this study. M&S is a virtual experiment, in which large computational power along with the knowledge gained from previous experiments and theoretical knowledge are utilized to simulate the results of some physical phenomenon. It is valuable especially in the early phase of the design process when hardware may not be available.

The M&S of the neutron detector is challenging owing to the uncertainty and the randomness in the neutron interaction and transport in matter. Such processes can be best modeled and simulated by using a unique technique known as *Monte-Carlo* method. A brief description of Monte-Carlo method is presented in Section 3.2. A Monte-Carlo tool i.e., GEANT4 (**GE**ometry **ANd** **T**racking) has been used in this study and is described in Section 3.3.

In Section 3.4, semiconductor device simulation software known as **T**echnology **C**omputer-**A**ided **D**esign (TCAD) from Silvaco has been introduced. This section also gives simulation methodology; models used and associated parameters necessary for device simulations using TCAD.

### 3.2 MONTE-CARLO (MC) METHOD

MC methods are used to solve the complex integro-differential problems of wide range of applications, ranging from engineering, science to business and finance. It

involves performing many simulations with random sampling and probabilities for estimating the mathematical function and imitating the operations of complex systems [88], [89].

### 3.2.1 Monte-Carlo in Nuclear and Particle Physics

A particle interacting with matter can undergo several types of physical processes such as radiative capture, absorption, scattering, etc., which all are random in nature with a probabilistic distribution (interaction cross-section). In the case of neutron transport, it is quite challenging to determine the probabilistic path direction and length which changes very often owing to a large number of interactions and uncertainties involved. Therefore, it is better to consider the fraction of a large number of neutrons that may undergo several types of interactions with the help of MC simulations, rather than anticipating what an individual neutron can do. In MC simulations, billions of neutrons can be invoked with certain energies and directions which travel in the matter according to their mean free path ( $\lambda$ ) with random variations from the expected mean value [89]. The MC technique applied decides on simulating a particular type of interaction taking into account the cross-sections for several kinds of interactions which depend on the neutron energy and the material in which neutron is traversing. The repercussions of interaction such as secondary particle generation, change in direction/energy are estimated based on the statistics following the selection of interaction type. This process reiterates until that neutron, and the created secondary particles are absorbed or escape from the defined simulation boundaries, or their energies are below the energy cut-offs .

Several MC codes are under active development for employment in the study of nuclear and particle physics. Most of them are used for dedicated particles such as for electron and proton transport ETRAN and PTRAN are used, respectively. The



MCNP/MCNPX (**M**onte **C**arlo **N**-**P**article **eX**tended), and GEANT4 (**GE**ometry **ANd** **T**racking) are widely accepted and are the most popular general purpose MC codes employed for all particle transport through matter.

In this work, GEANT4 (version 4.10.00.p03) has been extensively used for MC simulations for neutron transport study primarily because it is an open source software and there are several studies which report excellent agreement of both MCNPX and GEANT4 simulation results with the experimental results [50], [89], [90].

### 3.3 GEANT4 SIMULATION TOOLKIT

GEANT4 is a MC toolkit developed in CERN in 1993 and is being developed continuously, maintained and supported by the worldwide collaboration of scientists and software engineers known as GEANT4 collaboration [91]. It has been developed using software engineering and object-oriented approach and implemented in the C++ programming language. Its application consists of particle physics, nuclear physics, accelerator design, space engineering, and medical physics.

GEANT4 is a set of *Application Programming Interface (API)*<sup>\*</sup> tools for simulating a passage of particles through matter. Unlike the other MC codes, it is not an executable program, but it is a set of predefined C++ classes with which the users must write their own C++ code and compile it to generate an executable file. It is implemented as per the software requirements of modern experiments to deliver key requirements of functionality, modularity, extensibility, and openness. Thus, its implementation of physics is transparent and open to the user for validation. It allows the user to understand, modify and extend it in all other possible domains. The modularity in its architecture enables the user to pick only those components that one needs to build the application.

---

<sup>\*</sup>An API is a set of routines, protocols, and tools for building software applications. Basically, an API specifies how software components will interact with each other.

#### 3.3.1 GEANT4 class categories

GEANT4 is a large software which is divided into 17 small independent logical units, known as *class categories*, in order to enable their parallel development and easier organization without interfering with each other [92]. The categories are a group of *classes*<sup>\*</sup>, which are the smallest logical unit defined in the software. The *classes* of the same category have a strong relationship among themselves whereas a weak link with the *classes* of other categories. The role of each class category in GEANT4 is briefly summarized below:

- The *Global class category* handles third-party software and libraries and contains all classes, structures, types, systems of units, physical constants and random numerical values required for general use in GEANT4.
- *Material category* comprises all the ingredients required for the creation of materials: isotopes, elements, and compounds through the NIST<sup>†</sup> database [92].
- *Geometry category* deals with the geometrical definition using the constructive solid geometry (CSG) or as an input from CAD software.
- *Particle category* is responsible for the definition of primary particles. It could be any of leptons, mesons, baryons, bosons, short-lived resonant particles, and ions.
- *Tracking* and *Track categories* manage the propagation of a particle by implementing relevant physical processes.
- *Physics category* handles all the physics processes associated with the particle interaction with matter according to the material, energy and type of the particle.
- *Hits category* is responsible for the creation of hits (snapshot of particle interaction) in the sensitive region of the detector geometry, and *digitization category* manages

---

<sup>\*</sup>In C++, a *class* is a user-defined data type which can hold data as well as functions.

<sup>†</sup>NIST: National Institute of Standards and Technology is a database that contains definition of elements and compound materials used in HEP and Medical fields.

the information stored in Hits.

- *Event categories* control the full event which consists of primary particles and subsequent secondary particle generation, and their tracking. When a simulation is initialized with several particles, each of the particles is treated as an individual event and is processed individually. The Event is the primary unit of GEANT4 simulation.
- *Run* is the largest unit of simulation. A run is made up of a sequence of events. Within a run, the detector geometry, the setup of sensitive detectors, primary particles and the physics processes incorporated in the simulation should be kept unchanged.
- *Visualization category* manages the visualization of detector geometry (2D/3D), trajectories and hits of primary and secondary particles, and it interacts with the graphical libraries needed for the production of graphical user interface (GUI). The object-oriented methodology allows usage of several external independent drivers for visualization viz., Qt, OpenGL, X11, Dawn, and VRML, etc.
- *Intercoms category* is responsible for the interaction of GEANT4 through the user-interface and also enables the communication between several categories.
- *Interfaces* manage the GUI and handle the interactions with the external software.

GEANT4 classes permit the user to define physical models, fundamental particles, sensitive detectors, geometries, and visualization of the track, as well as bestow a high control over the input parameters and the output information needed. As mentioned previously, GEANT4 is not standalone software which can be used out-of-the-box. The users must write their own code using the tools and resources provided by GEANT4 for simulating his/her application. To begin any GEANT4 simulation, users need to set up a mandatory *main( ) program*, which calls and invokes all other classes. It controls the flow

of the simulation and manages the event loop(s) within a run. In addition to the *main( )*, there are three mandatory user initialization classes viz., a) G4VUserDetectorConstruction, b) G4VUserPhysicsList, c) G4VUserActionInitialization. The first mandatory file contains the description of detector geometry, material, etc., the second one defines the physics, and the third file contains the compulsory user action class G4VUserPrimaryGeneratorAction, responsible for primary event kinematics and generation. Apart from the above classes, there are several other optional user action classes which may be used for customization of the simulation process. After implementing all the classes, users have to compile all the files with the help of GEANT4 kernel in order to create an executable file. This executable file is required to run the simulation.

Once the simulation starts, GEANT4 splits the particle trajectories into a number of steps with a specific path length ' $\lambda$ ', which is an average distance between two successive interactions, known as mean free path. GEANT4 uses data driven modeling for the calculation of cross-sections, when experimental or evaluated data are available with sufficient coverage. For neutron and proton induced isotope production, and for detailed transport of neutrons at low energies, GEANT4 uses data driven modeling approach based on evaluated neutron data library ENDF/B-VII [91]. Depending upon the physics and material where the particle is located, the code selects the process randomly with the smallest length. At the end of the step, the information of the particle is updated and a new Step is calculated. The particles are transported Step by Step. Over the selected process, the code takes the actions defined in user action classes. This process is iterated until, either the particle is absorbed, or escapes from the simulation boundaries, i.e., goes out of the sensitive region, or its energy is below than its energy cut-off values.

### 3.3.2 GEANT4 simulation flow for present work

The summary of GEANT4 C++ files written for modeling the neutron detector and studying its transport and interactions is given in Table 3.1:

**Table 3.1 Details of GEANT4 C++ files for modeling neutron detector**

File name	Purpose
Detector_Construction.cc	Detector geometry, i.e., shape, dimensions, placement, position, material, etc., is defined. A sensitive region is also defined in this file, which will register the hits.
Primary_Particle.cc	General Particle Source class of GEANT4 is defined. It takes source setting information through input macro file.
Physics_Lists.cc	<b>QGSP<sup>*</sup>_BERT_HP</b> physics model is used from predefined reference physics List [93]. It uses a high-precision neutron model and cross sections to describe elastic and inelastic scattering, capture and fission, for neutrons below 20 MeV [94]. This file also contains set cuts values for different particles (0 mm for proton and gamma & default value for other particles).
Detector_Messenger.cc	This file enables the changing of detector dimension and material parameters from the input macro file.
Hit.cc & SD.cc	For connecting the sensitive region to the Hits category to register interaction information.
Run.cc RunAction.cc, SteppingAction.cc, and TrackingAction.cc	These files enable the control of the simulation process and help in getting desired output from the Step, Track and Run levels.
HistoManager.cc	This file provide access to external software, i.e., ROOT <sup>†</sup> for plotting the histograms
Main.cc ( <i>main ()</i> method)	This file calls and invokes all mandatory (Detector Construction, Primary Particle Generator and Physics List) and optional Classes (Run, Stepping Action, etc.). It controls the flow of the simulation and manages the event loop(s) within a run.

<sup>\*</sup>The quark-gluon model (QGS) handles protons, neutrons, pions and kaons above 12 GeV. BERT stands for BERTINI model.

<sup>†</sup> ROOT is a data analysis framework developed in CERN for dealing with large data processing, statistical analysis, visualization and storage.

Now, all the above mentioned C++ files are compiled in order to create an executable file. This executable GEANT4 application can be run in following 4 ways:

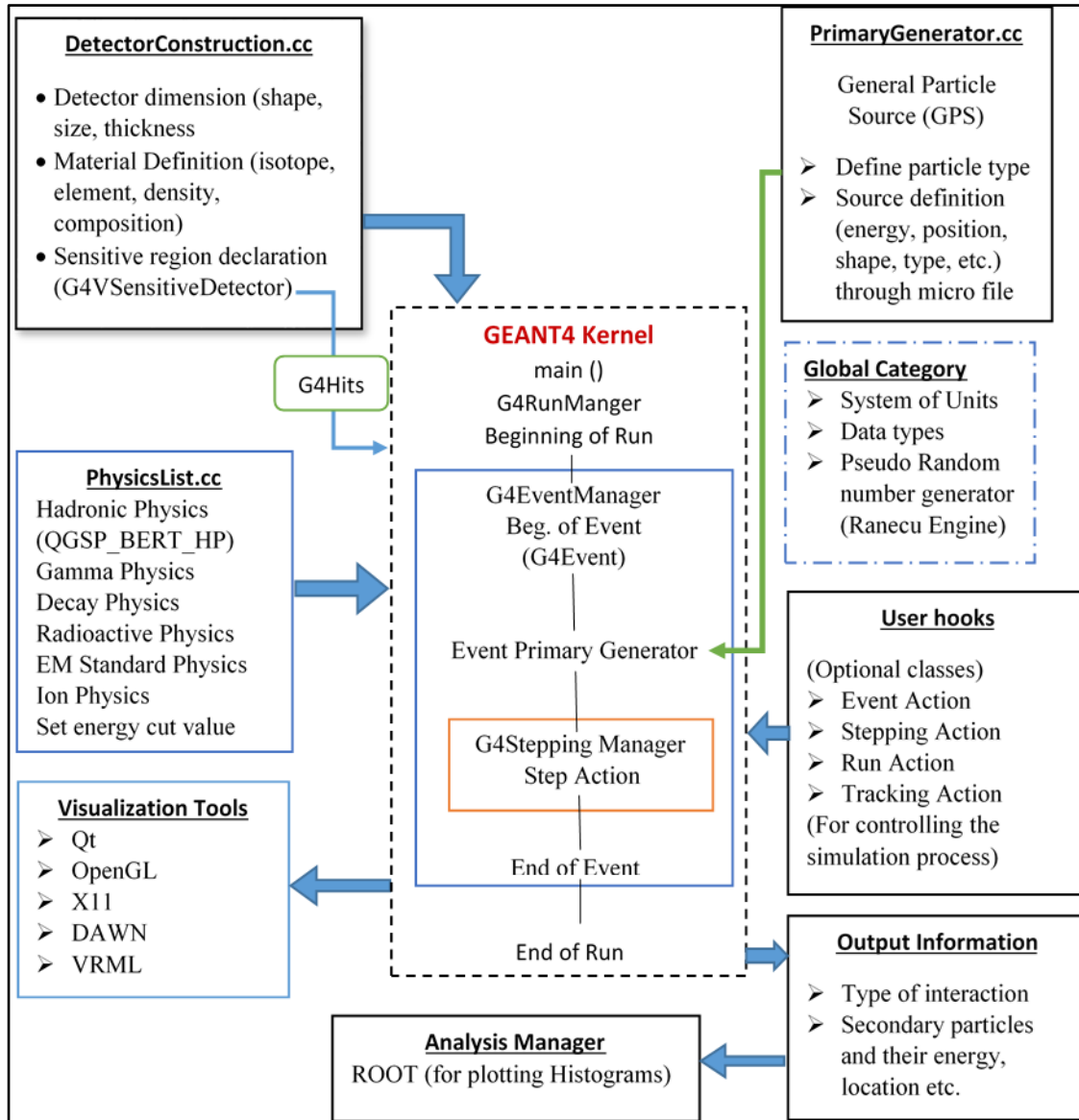
- (i) 'purely hard-coded' batch mode
- (ii) batch mode, but reading a macro of commands
- (iii) interactive mode, driven by command lines
- (iv) interactive mode via a Graphical User Interface

In this work, we have executed in batch mode with a file of macro commands. This way the run conditions can be changed easily in the macro file without recompiling the full code. As we begin the simulation, the *main( )* method creates an instance of the *G4RunManager* class. The Run Manager then performs the detector construction, creates the physics processes, calculates cross sections and otherwise sets up the run. Finally the *beamOn( )* method of Run Manager, which takes integer argument corresponding to a number of particles one wants to simulate, starts shooting the primary particles as defined in the coding. Once, a run has begun neither the detector setup nor the physics processes can be changed. A virtual method named *DoEventLoop( )* of run manager class handles the event loop. i.e., performs the entire simulation of an event. This method creates a *G4Event* object, and then primary particle and the primary vertex is assigned to this *G4Event* object. Then it is forwarded to the Event manager, i.e., *G4EventManager*. A *G4Event* object contains 4 significant information viz., primary vertexes and primary particles, trajectories, hits and digits collection. The event manager then performs following tasks: first, it converts the primary vertex and primary particle objects associated with the *G4Event* object to *G4Track* objects; then it sends all the *G4Track* objects representing the primary particles to the *G4StackingManager*; then each *G4Track* object is popped one after another and sent to the *G4TrackingManager*. Now, the tracking manager passes on the information to the *G4SteppingManager*, which plays a crucial role in tracking the particle. It actually steers

the stepping of the particle. It is also responsible for taking care of all messages that is passing between the objects of different categories relevant for particle transport (for example, geometry and interactions in the matter).

Now, the physics processes describe how the particles interact with the material. GEANT4 has seven major categories of processes viz., 1) electromagnetic, 2) hadronic, 3) decay, 4) photolepton\_hadron, 5) optical, 6) parameterization, and 7) transportation. Each process is equipped with two groups of methods which play an essential role in tracking, *Get-Physical-Interaction-Length* (GPIL) and *DoIt*. The GPIL method calculates the step length from the current space-time point to the next space-time point by calculating the probability of interaction from the cross-section information of the respective process. Each process then proposes a step length based on the interaction and cross-section information. The stepping manager considers the smallest of these step length. This step length is then compared with the safety distance to the next volume boundary (calculated by geometry navigator). If the step length given by process is less than the safety distance, then the step length is selected. Otherwise it is recalculated, and the smaller of the two is taken. Now, the *DoIt* method is invoked which implements the details of the interaction, change in particle's energy, momentum, direction and position, and generating secondary tracks as per the governing process. When the particles travel through the medium, all the continuous processes are invoked. The particle kinetic energy will be updated only after all the invoked process has been completed. The change in the kinetic energy is the sum of the contributions from all the continuous processes. The secondary particles, if generated in the process, are stored in the stack and tracked once the tracking of the primary particle is completed. The G4Step and G4Track object contain all the necessary information about the tracking of the particle, which can be utilized to extract the output information using the user action classes and analysis manager.

A flow diagram of GEANT4 simulation is shown in Figure 3.1. The flow presented in this section is a very abstract process flow of GEANT4. For a detailed understanding of methods in each category, their operation, and definition, etc., the user's manual for application developers should be referred [92].



**Figure 3.1** An illustration of the GEANT4 process flow.

Finally, it is worth to mention that although GEANT4 has got a lot of advantages in terms of its openness, functionality, modularity, and extensibility, there are some disadvantages too: first thing is its huge complex structure, which requires a significant



amount of time for the user to learn and adapt. Secondly, it needs high-performance computing resources with Linux Operating System for reducing the simulation time with multi-threading mode.

### **3.3.3 System information where GEANT4 simulations were performed**

GEANT4 (version 10.00.p02) is installed in our local PC as well as in High-Performance Computing (HPC) cluster facility available in IGCAR. Local PC has a Scientific Linux 6.6 operating system with 3 GB RAM and Core2Duo processor. The GEANT4 application is developed, checked and tested in local PC. The time required for simulating 1 MeV neutron with the fluence of  $10^6$  neutrons/cm<sup>2</sup> through a 1 cm box is ~ 30 min. The simulation of  $10^9$  events in local PC took around 100 hours. The final simulations are performed in the HPC clusters with  $10^9$  numbers of events and up to 5 iterations for higher accuracy. The detail of HPC is as follows:

#### **GPU based HPC Cluster System (Master node: 1. Compute Nodes: 4):**

- Processor- Dual Six Core 64-bit Intel Xeon @3.06 GHz and 48/96 GB RAM
- Graphics Processor- NVIDIA Tesla 2090 GPU 12 Nos.
- Cluster- 4 node, 48 processor core
- Performance- system performance of 3.8 TeraFLOPS
- Interconnects- Infiniband 40 Gbps Two Gigabit Ethernet
- Storage- 4.8 TeraByte Unified Storage
- Operating System- Red Hat Enterprise Linux 6.2

#### 3.4 SEMICONDUCTOR DEVICE SIMULATION USING TCAD

A semiconductor device can be modeled on different levels of physical description ranging from device fabrication steps up to the device operation subjected to several conditions. Semiconductor device simulation has earned relevance for the design and optimization of electronic semiconductor applications due to the rising design complexity and the cost reduction achieved by reducing the number of experimental batch cycles. Today, multidimensional general purpose device simulators are available for modeling Si and GaAs devices. With the advancements in the state-of-the-art simulation tool, it is possible to adopt such available simulation tools for wide band-gap material such as 4H-SiC. Several physical device simulation tools have been developed to understand the device operation. Silvaco TCAD is one of the commercially available tools used for process and device simulations of semiconductor devices [95]. Silvaco TCAD has been used in this work to study the irradiation effects on the electrical characteristics of the *n*-type 4H-SiC-based SBD detectors. The next subsection gives a brief introduction of the Silvaco TCAD modules and simulation methodology adopted in this work.

##### 3.4.1 Silvaco: TCAD simulation suite

Semiconductor simulation is broadly classified into two categories, viz., Process simulation (module: ATHENA) and device simulation (module: ATLAS). Process simulation tool simulates all semiconductor processing steps for optimizing and evaluating process alternatives, sensitivity, and yield improvement. It also provides a realistic structure and impurity profile for meaningful device simulation. On the other hand, device simulation tool simulates single-device electrical characteristics for understanding physical effects, advanced device design, and reliability study. It also provides accurate parameters

for transistor level models to predict circuit performance. We have extensively used ATLAS module and other related modules for device simulation.

ATLAS is a physically-based 2D/3D device simulator. It predicts the electrical behavior of specified semiconductor structures and provides insight into the internal physical mechanisms associated with device operation.

Physically-based simulation provides following advantages [96]:

- a) it is predictive,
- b) it provides insight,
- c) it conveniently captures and visualizes theoretical knowledge,
- d) it is much quicker and cheaper than performing experiments, and provides information that is difficult or impossible to measure.

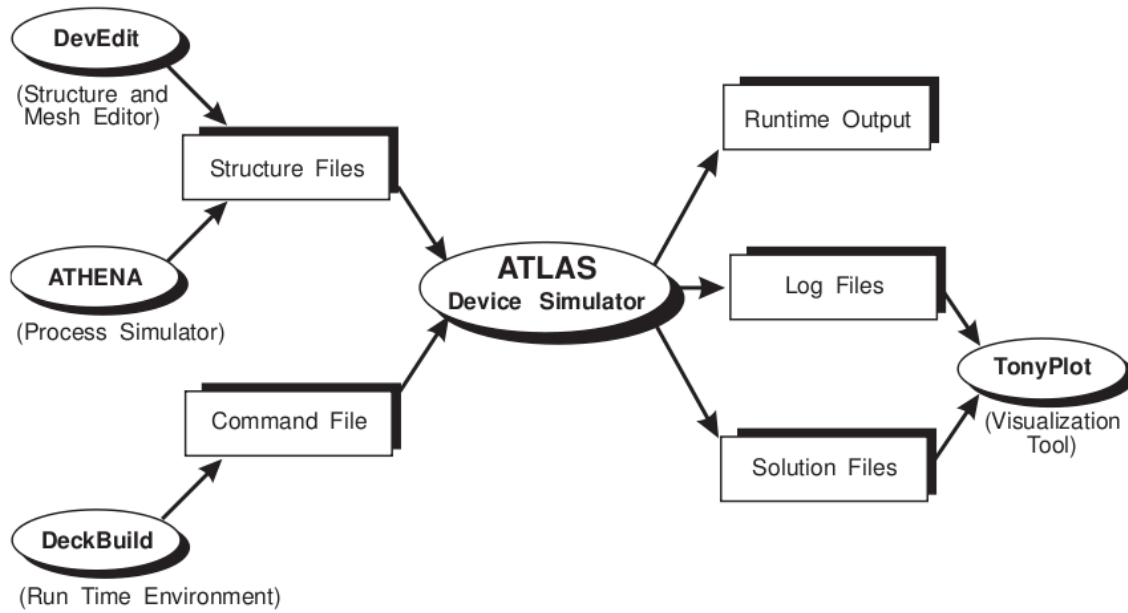
The challenges include:

- a) incorporation of all the relevant and correct physical models,
- b) proper fine meshing near contacts, junctions and edges,
- c) implementation of numerical procedures to solve the associated equations,
- d) Selection of proper precision level. The higher the precision level, the more considerable computing time and resources it requires.

In ATLAS, device simulation problem is defined in the following steps:

- Define the physical structure which needs to be simulated.
- Define the physical models related to the device and process.
- Define the bias conditions for which electrical characteristics are to be simulated.

Figure 3.2 shows the inputs and outputs of ATLAS, which are explained in Table 3.2.



**Figure 3.2 ATLAS inputs and outputs [96].**

**Table 3.2 Description of modules and I/O files of Silvaco TCAD used in this thesis.**

Modules	Description
ATLAS	Device simulation module of Silvaco TCAD
ATHENA	Process simulation module of Silvaco TCAD
DECKBUILD	An interactive Graphical User Interface (GUI) to provide a user-friendly runtime environment for integration of the different aspects of the Silvaco TCAD
DEVEDIT	A device structure editor. It can be used to generate a new mesh on an existing structure and can be used to create or modify a device. 2D and 3D simulators can then use these device structures. It can be used as a simulator under DECKBUILD or through a GUI
TONYPLOT	Powerful graphical display and analysis tool
I/O files	Description
Structure files	It contains device structural information obtained either from DEVEDIT or ATHENA simulation run.
Command File	It contains all the command files for ATLAS to execute.
Runtime output	Provides the progress and the error and warning messages as the simulation proceeds
Log Files	It stores all terminal voltages and currents from the device analysis
Solution Files	It stores 2D and 3D data relating to the values of solution variables within the device at a given bias point

### 3.4.2 Basic Semiconductor Equations

For reliable prediction of the device characteristics, it is vital to understand the physical processes in semiconductor devices. For accurate simulation of real devices, in addition to the description of the device structure, it is imperative to define appropriate physical models in the simulation. After defining the device structure and the physical models, simulation continues with solving the basic semiconductor equations viz., Poisson's equation, the continuity equations, the drift and diffusion current equations. By solving these equations the electrical performance and  $I$ - $V$  relations for the electronic devices can be derived by applying stimuli in the form of voltages or photons or thermal energy. So, they form the theoretical basis for analyzing and interpreting the measured performance of electronic devices. The equations are [96]:

**Poisson's equation:** it relates the electrostatic potential to the space charge density.

$$\text{div}(\epsilon_s \nabla \psi) = -\rho \quad (3.1)$$

where  $\epsilon_s$  is the dielectric constant of the semiconductor,  $\psi$  is the electrostatic potential, and  $\rho$  is the local space charge density.

**Electron and Hole continuity equations:** it expresses the conservation of electrons and holes at particular location.

$$\frac{\partial n}{\partial t} = \frac{1}{q} \text{div} \vec{J}_n + G_n - R_n \quad (3.2)$$

$$\frac{\partial p}{\partial t} = -\frac{1}{q} \text{div} \vec{J}_p + G_p - R_p \quad (3.3)$$

where  $q$  is the elementary charge,  $n$ , and  $p$ , are the electron and hole concentrations,  $J_n$  and  $J_p$  are the electron and hole current densities,  $G_n$  and  $G_p$  are the generation rates for electrons and holes,  $R_n$  and  $R_p$  are the recombination rates for electrons and holes.

#### Electron and Hole current density equations:

$$\vec{J}_n = q\mu_n nE + qD_n \nabla n \quad (3.4)$$

$$\vec{J}_p = q\mu_p pE + qD_p \nabla p \quad (3.5)$$

where  $J_n$  and  $J_p$  are the electron and hole current densities,  $q$  is the elementary charge,  $n$ , and  $p$ , are the electron and hole concentrations,  $E$  is the electric field,  $\mu_n$  and  $\mu_p$  are the electron and hole mobilities, and  $D_n$  and  $D_p$  are the electron and hole diffusion coefficients.

ATLAS solves the equations on a discrete mesh using Newton/Gummel/Block iterative method [96] in predetermined device region with the relevant boundary conditions which gives the potential distribution, the electron and the hole distribution. After a numerical solution of the equations is found, the simulated electrical characteristics can be analyzed using the visualization tool ‘*tonyplot*’ and compared with experiments. The next section describes the important models required for implementing a SiC-based SBD in ATLAS

#### 3.4.3 Models for SiC device description in TCAD

A 2D-structure of  $n$ -type 4H-SiC SBD has been generated using DEVEDIT module of the Silvaco TCAD. The structure is then loaded into the ATLAS device simulation module. The 4H-SiC material parameters are defined together with the essential models such as band-gap, band-gap narrowing, mobility, carrier statistics, recombination, tunneling, impact, and incomplete ionization. As the temperature increases, the lattice constant increases which in turn decreases the band-gap. The temperature ( $T$ ) dependence of the band-gap energy is modeled using the *Varshni* or *Universal Energy Bandgap* model which is governed by equation (3.6) [96], [97]:

$$E_g(T) = EG300 + EGALPHA \left[ \frac{300^2}{300 + EGBETA} - \frac{T^2}{T + EGBETA} \right] \quad (3.6)$$

where, EG300, EGALPHA and EGBETA are user specifiable parameters of MATERIAL statement, whose values for 4H-SiC are specified in Table 5.1 (Chapter 5).

In case of heavy doping (greater than  $10^{17} \text{ cm}^{-3}$ ), the electron and hole related energy bands are attracted towards each other. This phenomenon leads to the decrease in the band-gap value and is known as band-gap narrowing. To model this behavior, *Lindelfelt* Band-gap narrowing model (BGN.LIND) is specified in MODELS statement [96].

The mobilities of electrons and holes are the functions of the local electric field, doping concentration, lattice temperature, etc. For doping and temperature dependent low field mobility, *Caughey-Thomas* model as expressed by equations (3.7) and (3.8) is considered in this simulation study [96].

$$\begin{aligned} \mu_{n0} &= MU1N.CAUG. \left( \frac{T}{300K} \right)^{ALPHAN.CAUG} \\ &+ \frac{MU2N.CAUG. \left( \frac{T}{300K} \right)^{BETAN.CAUG} - MU1N.CAUG. \left( \frac{T}{300K} \right)^{ALPHAN.CAUG}}{1 + \left( \frac{T}{300K} \right)^{GAMMAN.CAUG} \cdot \left( \frac{N}{NCRITN.CAUG} \right)^{DELTAN.CAUG}} \end{aligned} \quad (3.7)$$

$$\begin{aligned} \mu_{p0} &= MU1P.CAUG. \left( \frac{T}{300K} \right)^{ALPHAP.CAUG} \\ &+ \frac{MU2P.CAUG. \left( \frac{T}{300K} \right)^{BETAP.CAUG} - MU1P.CAUG. \left( \frac{T}{300K} \right)^{ALPHAP.CAUG}}{1 + \left( \frac{T}{300K} \right)^{GAMMAP.CAUG} \cdot \left( \frac{N}{NCRITP.CAUG} \right)^{DELTAP.CAUG}} \end{aligned} \quad (3.8)$$

where N is local (total) impurity concentration in  $\text{cm}^{-3}$  and T is lattice temperature in °K. This model is activated by specifying ANALYTIC in the MODELS statement. The

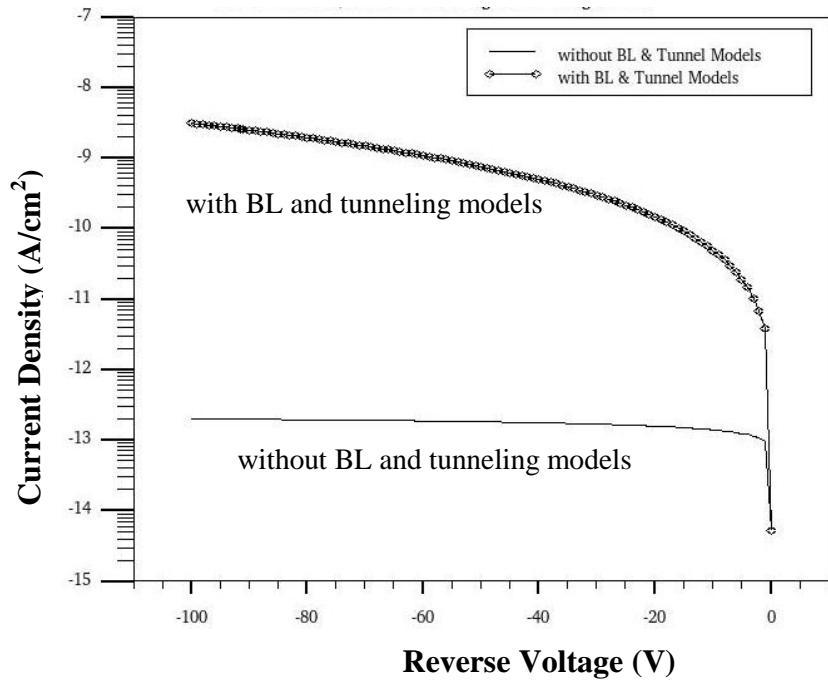
parameters of this model namely MU1N, MU2N, etc., are specified in the MOBILITY statement and corresponding values for 4H-SiC are given in Table 5.1 (Chapter 5). At very high electric fields, the velocity of the carriers saturates, leading to degradation in mobility. Thus, the saturation velocity model is also used in this study. The parameter VSATN of MOBILITY statement is associated with the saturation velocity model. The effects of temperature and doping on the band-gap and mobility of SiC along with the comparison of different models are explained elsewhere [97].

Carrier generation-recombination is the process through which the semiconductor material attempts to return to equilibrium from a disturbed state. For trap-assisted recombination, *Shockley-Read-Hall* (SRH) model is employed. The electron and hole lifetime parameters of SRH model, TAUN0 and TAUP0, are user-definable in the MATERIAL statement. For band-to-band transition, Auger recombination model is used and parameters AUGN and AUGP of MATERIAL statement are associated with it.

The impact ionization model proposed by *Selberherr* is used in this model for simulating the high reverse bias condition which can lead to the avalanche breakdown [96]. This model is activated by using SELB parameter in IMPACT statement. The list is too exhausting to explain here. For more details, ATLAS Manual may be referred [96].

In order to create the Schottky contact, it is essential to define WORKFUN parameter in the CONTACT statement, or it will be considered as an ohmic contact by default. For wide band-gap material 256-bit precision is recommended. Furthermore, for accurately simulating the reverse *I-V* characteristics of the Schottky diode, the *image-force lowering* effect [70] and *tunneling current* models have been incorporated (defined using BARRIER and E.TUNNEL in CONTACT statement, respectively) [59], [70], [98]. The reverse current of the SBD was underestimated without these models (see Figure 3.3).

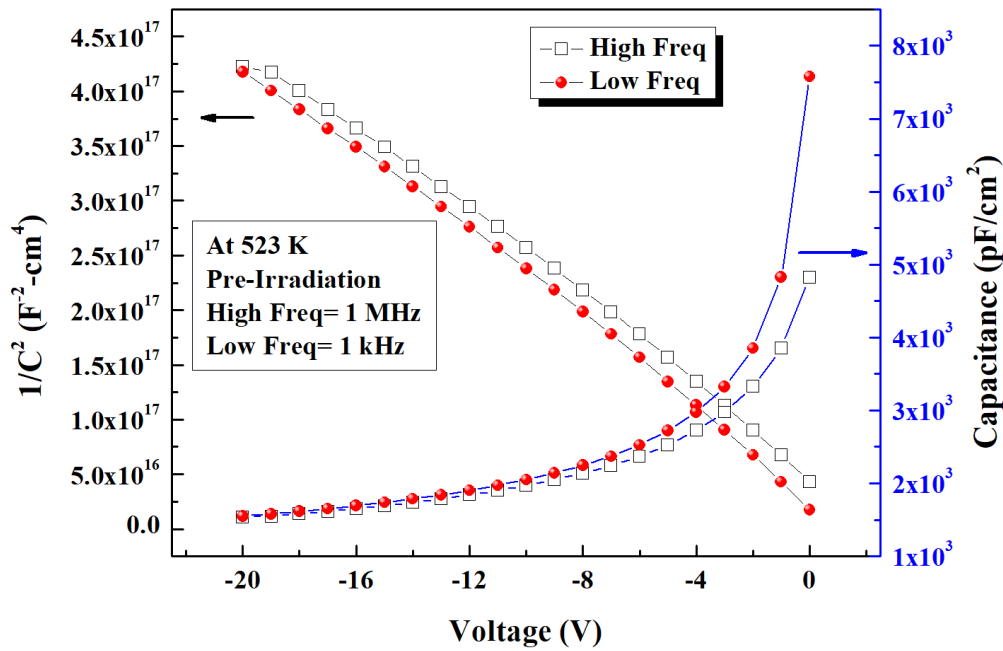




**Figure 3.3 Simulated reverse  $J$ - $V$ -characteristics of Ni/4H-SiC SBD with and without the barrier lowering and tunneling models.**

For simulating the  $C$ - $V$ -characteristics, an AC voltage with a certain frequency is superimposed on the DC bias. This results in a Y-parameter extraction which contains the conductance and capacitance information for each electrode in the device [96]. The  $C$ - $V$ -characteristics are performed with low (1 kHz) and high (1 MHz) frequency ac signals. It is observed that the  $C$ - $V$ -characteristics were almost identical for both the frequencies up to 423K. At 523K, a slight deviation is found between the plots (see Figure 3.4). It should be noted that the low frequency (LF) signal has predicted the  $C$ - $V$ -characteristics very well compared to the high-frequency (HF) signal which required fine meshing or very small step biasing for proper convergence of the simulation result at high temperature.

Similar situation was also observed while simulating the heavily irradiated (fluence  $>10^{15}$  particles/cm<sup>2</sup>) SBDs. The LF AC signal was able to predict the  $C$ - $V$ -characteristics whereas HF AC signal was failing to converge or was predicting a flat  $C$ - $V$  curve (after very fine meshing and 256-bit precision).



**Figure 3.4 Simulated  $(1/C^2)$ -V and C-V curve at 523 K with low (1 kHz) and high (1 MHz) frequency ac signals.**

The difference in the plots is evident at high temperature. High-frequency simulation required very fine meshing and high-precision (256 bit) for the simulation to converge. The simulation with high-precision and fine meshing took a huge amount of time to execute.

### 3.4.4 Irradiation-induced defect definition in TCAD

An energetic radiation particle impinging on the semiconductor loses its energy via ionization and non-ionization processes. During ionization, electron-hole pairs are created whereas the result of a non-ionization process could be a defect generation (briefly discussed in Chapter 2). The generated defects can be of primary types such as vacancy defects, interstitial defects, or of secondary types such as E-center, A-center and other complex defects [52], [56], [99]. The primary defects are mobile and unstable at room temperature (RT). Some of these defects are annealed with time or at a higher temperature. Other defects may combine with dopants to create stable defects. The formation of defect complexes in the semiconductor is complicated and only partially understood [99]. Majority of these defects are electrically active and introduce deep-levels in the semiconductor band-gap [76]. These deep levels are often referred to as '*trap centers*' or '*recombination centers*'. Based on the position in band-gap, capture cross-section of the

majority and minority carriers, the deep levels can be categorized as majority carrier trap or minority carrier trap. In an  $n$ -type semiconductor, an electron trap is a majority carrier trap. Deep levels can significantly modify the electrical properties of the semiconductors and eventually the devices fabricated thereon.

The Radiation Effect Module (REM) in Silvaco TCAD allows the simulation of defect generation due to the energetic particle impingement in the semiconductor [96]. The total defect density of states ( $N_T$ ) due to irradiation is modeled as:

$$N_T = \alpha_D \rho E_l \Phi_F \quad (3.9)$$

where  $\alpha_D$ ,  $\rho$ ,  $E_l$ , and  $\Phi_F$ , is the damage factor by a particular particle, density of the material, non-ionizing energy loss (NIEL) factor, and total radiation flux, respectively. Traps are then created within the band-gap of semiconductor material using the defect density of states ( $N_T$ ). In addition to that, trap level signatures (if known) can be directly introduced in the modeling using the 'TRAP' statement. The parameters of TRAP statements are:

- **E.LEVEL:** Sets the energy of the discrete trap level. For acceptors, it is relative to the conduction band edge. For donors, it depends on the valence band edge.
- **DENSITY:** Sets the maximum density of states of the trap level.
- **SIGN:** Specifies the capture cross section of the trap for electrons.
- **SIGP:** Specifies the capture cross section of the trap for holes.
- **ACCEPTOR/DONOR:** Specifies an acceptor/donor-type trap level.

In this work, the signatures of dominant trap-levels, as reported in literature for a specific particle irradiation, are incorporated using TRAP statement and its effect on the electrical performance of the 4H-SiC SBD detector is studied.

### 3.5 SUMMARY

The state-of-the-art neutron transport code, i.e., GEANT4 and semiconductor device simulation tool, i.e., Silvaco TCAD are introduced in this chapter. The GEANT4 simulation flow pertaining to this work is presented. Several components of Silvaco TCAD are briefly explained. Some of the challenges, important models used and their associated parameters necessary for device simulation in TCAD are also discussed. Irradiation induced defect definition using TRAP statement is also presented.

\*\*\*\*\*

# 4

## CONVERTER OPTIMIZATION AND EFFICIENCY ENHANCEMENT

---

### 4.1 PREAMBLE

This chapter presents the results of GEANT4 Monte-Carlo simulations performed for optimizing the thicknesses of several neutron sensitive converter materials for different energy neutron sources. In order to achieve high efficiency, the optimization of converter thickness is essential. The methodology adopted for thickness optimization and efficiency estimation is described in Section 4.2. This section also contains the simulation methodology used for studying the effect of background discrimination on neutron detection efficiency and for studies towards achieving higher efficiency.

Section 4.3 presents the benchmarking studies performed for the planar detector modeled in GEANT4 against the published results. For benchmarking studies High Density Polyethylene (HDPE) is used as a converter. The detector geometry and neutron source is defined similar to the MCNPX study performed by Sedlackova *et al.*, [50], GEANT4 simulation done by Cortesi *et al.*, [100] and experimental work done by Flammang *et al.*, [24]. Three aspects are compared: Probability of Interaction with analytical calculation, optimized thickness and maximum efficiency achievable with HDPE.

In Section 4.4, simulation results related to the aspects described in Section 4.2 are presented for several neutron sensitive hydrogenous converter materials.

### 4.2 SIMULATION METHODOLOGIES IN GEANT4

GEANT4 simulations are performed for studying the following three aspects of various neutron sensitive converter materials:

- a) Optimization of converter thickness to achieve maximum efficiency.
- b) Effect of background discrimination on detection efficiency
- c) Improvement in detection efficiency

The subsequent subsections briefly describe the methodology for studying these aspects:

#### 4.2.1 Methodology for converter thickness optimization

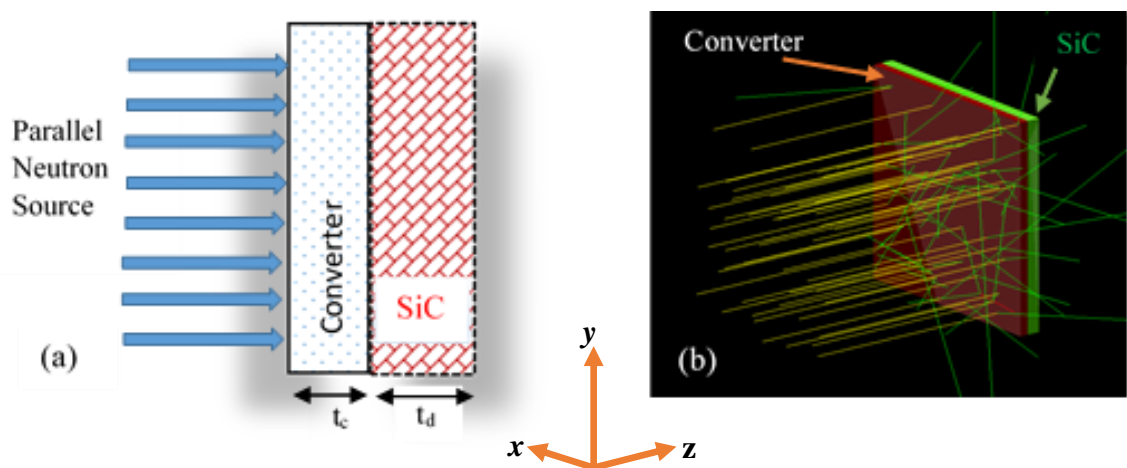
The planar configuration (converter-semiconductor setup) of detector as shown in Figure 4.1 (a) is defined using GEANT4.10.00.p02 version. It consists of two regions: the first region is a converter layer composed of neutron sensitive material responsible for generation of charged particles upon interaction with neutrons and the second region is the SiC-based semiconducting region to detect those generated charged particles. The cross-sectional area of the front face of the converter and the SiC semiconductor surface (XY-plane) is  $1 \text{ cm}^2$ . The thickness of the SiC region ( $t_d$ ) is kept at  $600 \text{ }\mu\text{m}$  (see section 4.4.1) and the thickness of converter ( $t_c$ ) is varied from one micrometer to few millimeters in order to optimize the thickness of converter layer. The converter thickness at which the obtained detection efficiency is maximum, is regarded as the optimum thickness. The detection efficiency ( $\eta_{det}$ ) is estimated as expressed by equation (4.1):

$$\eta_{det} = \frac{N_{p_{C \rightarrow S}}}{N_n} \quad (4.1)$$

where  $N_{p_{C \rightarrow S}}$  is the number of recoil protons generated in converter material and depositing their energy in the sensitive region of the SiC detector and  $N_n$  is the total

number of incident neutrons on the front face of neutron-sensitive converter material. Therefore, in other words, the optimum thickness is the thickness at which, the maximum number of charged particles from converter would reach into the detector's active region to generate a detectable signal.

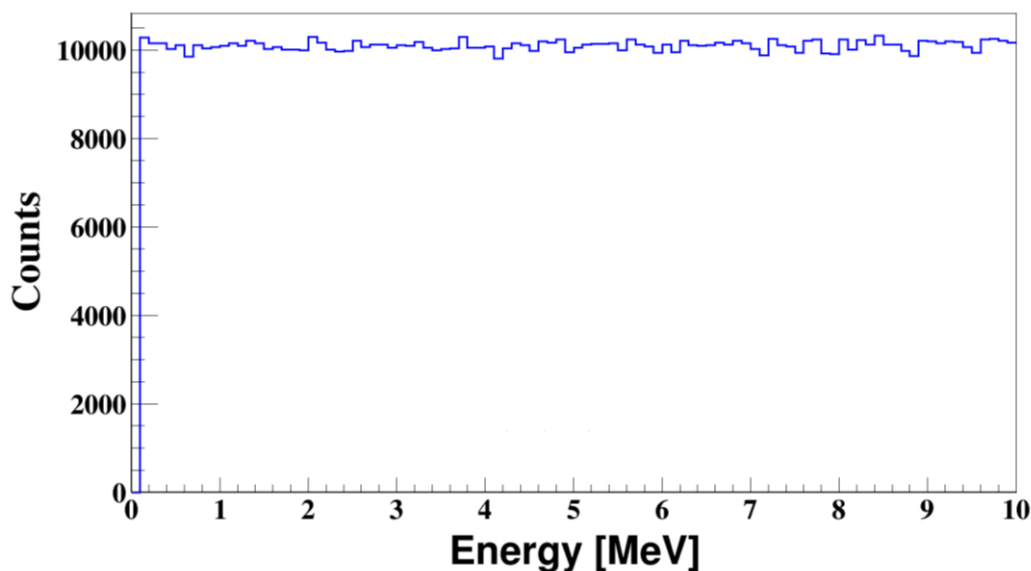
The General Particle Source (GPS) class of GEANT4 particle category is used to generate several mono-energetic as well as standard neutron sources. In each run of the simulation, total fluence of  $10^9$  neutrons/cm<sup>2</sup> are emanating from the planar source in the form of a parallel beam, and impinging uniformly and perpendicularly on the front face of the converter (as shown in Figure 4.1 (b)). In order to achieve the maximum theoretical neutron detection efficiency, the source is defined in such a way that the incident neutrons are impinging uniformly and perpendicularly on the front face of the converter material— a standard approach suggested by McGregor *et al.*, [101]. However, in real-world applications, neutrons fall from the random directions on the detector surface. Therefore, in practical applications, the actual detection efficiency would always be lesser than the efficiency reported by this simulation study.



**Figure 4.1 (a) Schematic of the Planar detector configuration (b) Screenshot from GEANT4 simulation.**

#### 4.2.2 Methodology for study of effect of background discrimination

Neutron flux is generally accompanied by gamma or other background radiations. Hence, it is of utmost importance to estimate the discrimination capability of the neutron detector between the neutrons and other background related counts. Therefore,  $\gamma$ -discrimination is one of the significant performance parameters for neutron detectors. It helps in minimizing the spurious counts. In addition to that, some of the generated charged particles have very low energy, or they lose a significant amount of energy in converter region before reaching the active region of SiC. In such cases, the energy deposited by the charged particles would be quite low, equivalent to other charged particles/background radiations. Hence, GEANT4 simulations have been carried out to analyze the impact of discrimination of  $\gamma$ , and other background radiations, on the neutron detection efficiency. For this study, a mixed neutron-gamma uniform source (spectrum shown in Figure 4.2) of energies ranging from 0.1 to 10 MeV has been generated using GPS, considering a fluence of  $10^6 \text{ cm}^{-2}$  for neutrons and  $\gamma$ -rays, both.



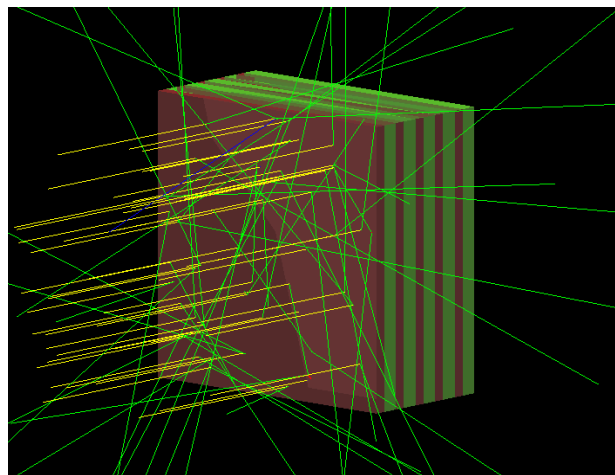
**Figure 4.2 Spectrum of the source used for simulating the mixed neutron-gamma source.**



Furthermore, to prevent the spurious counts originated due to the background radiations, an energy threshold value known as *Low-Level Discriminator* (LLD) is implemented in such a way that all the events depositing energy less than this threshold value are eliminated. The LLD also eliminates the low energy charged particles which result in a loss of counts for efficiency estimation. Therefore, for understanding the effect of elimination of low energy charged particles on the neutron detection efficiency, different LLD threshold values (300 keV, 500 keV, 1 MeV, and 2 MeV) are incorporated in this simulation study (in stepping action class) and reduction in detection efficiency has been estimated. The particles depositing energy higher than this threshold value are only considered for efficiency determination [102].

#### 4.2.3 Methodology for study of efficiency improvement

The efficiency achieved with the studied planar detector setup is low for reliable and consistent monitoring applications. Therefore, to enhance the efficiency of the detector, a special stacked detector configuration as shown in Figure 4.3, is proposed by juxtaposing several layers of converter and SiC by using the G4Replica Class of GEANT4.



**Figure 4.3 Stacked detector schematic.**

The yellow color rays depict the impinging neutrons whereas green rays represent  $\gamma$ -rays. The tracks of generated charged particles, which are blue in color can be viewed by zooming the interaction region (Red color: HDPE; Green color: SiC)

For initial simulation, the thicknesses of converter and SiC are kept as 400  $\mu\text{m}$  and 600  $\mu\text{m}$ , respectively. Simulations have been performed with  $^{241}\text{Am}$ -Be neutron source (fluence =  $10^9 \text{ n/cm}^2$ ) (spectrum is given in Figure 4.10 (b)). The improvement in neutron detection efficiency is estimated by increasing the number of stacked layers. The efficiency estimated in the stacked detector simulation is the total efficiency obtained with  $N$ -stacked layers. Furthermore, stacked detectors of different layers viz., 5, 10, 15, 20, and 50, have been simulated for different converter thicknesses and increment in efficiency is estimated.

### 4.3 BENCHMARKING SIMULATIONS

The simulation results are as good as the physics, and other inputs that are given to it. Since the fabrication of the detector is going to be a consequence of or depends on this study. Therefore, it is essential to perform benchmark simulations and reproduce some of the published experimental and simulation results to get enough confidence on the modeling code written by us using GEANT4 classes. HDPE is used as neutron converter in benchmarking studies because HDPE based neutron detectors have been reported in literature [24], [50], [100]. The benchmarking simulations include:

- (i) Comparison of probability of interaction for 1 MeV neutrons in HDPE converter, simulated using GEANT4 and computed analytically,
- (ii) HDPE thickness optimization and detection efficiency calculation for:
  - a)  $^{239}\text{Pu}$ -Be neutron source and comparison with [50],
  - b) 2.5 MeV D-D neutron source and comparison with [24], [100].

#### 4.3.1 Probability of Interaction for 1 MeV neutrons in HDPE

The incident neutrons may interact anywhere in the converter material since it is a random phenomenon. If  $N_0$  is the initial intensity of the incident neutron beam and  $N(t)$  is the intensity of the un-collided beam at the thickness of  $t$ , then  $N(t)$  can be given by equation (4.1) [60]:

$$N(t) = N_0 e^{-\Sigma t} \quad (4.2)$$

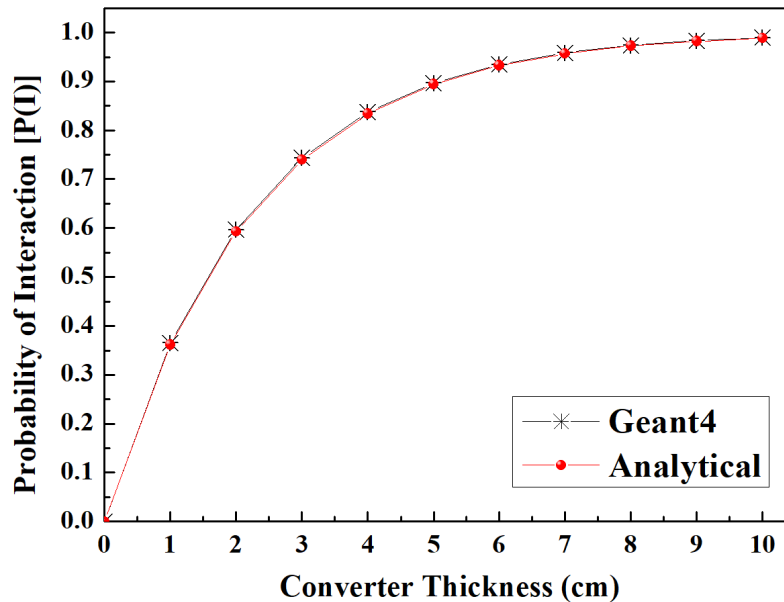
where  $\Sigma$  is the macroscopic cross-section for the converter material. The intensity of the beam which has collided with the material can be expressed as:

$$N_c = N_0 - N(t) \Rightarrow N_0(1 - e^{-\Sigma t}) \quad (4.3)$$

The probability of interaction  $P(I)$  can thus be expressed as  $(N_c/N_0)$ , i.e.,

$$P(I) = 1 - e^{-\Sigma t} \quad (4.4)$$

The macroscopic cross-section ( $\Sigma$ ) of HDPE for 1 MeV neutron interaction is  $0.449 \text{ cm}^{-1}$  [6]. The probability of interaction for 1 MeV neutrons with respect to converter thickness ( $t$ ) is calculated from the equation (4.4) and is compared with the GEANT4 simulated interaction probability in HDPE material with 1 MeV mono-energetic neutron source. Figure 4.4 represents that the GEANT4 simulation result is excellently complementing the analytical calculation.



**Figure 4.4 GEANT4 vs. Analytical calculation of  $P(I)$ .**

It can also be observed from Figure 4.4 that the  $P(I)$  is increasing as the thickness of the converter is increasing. After a certain thickness, it eventually saturates or reaches 99.9%, which shows that almost all the neutrons in the beam have undergone interaction with the

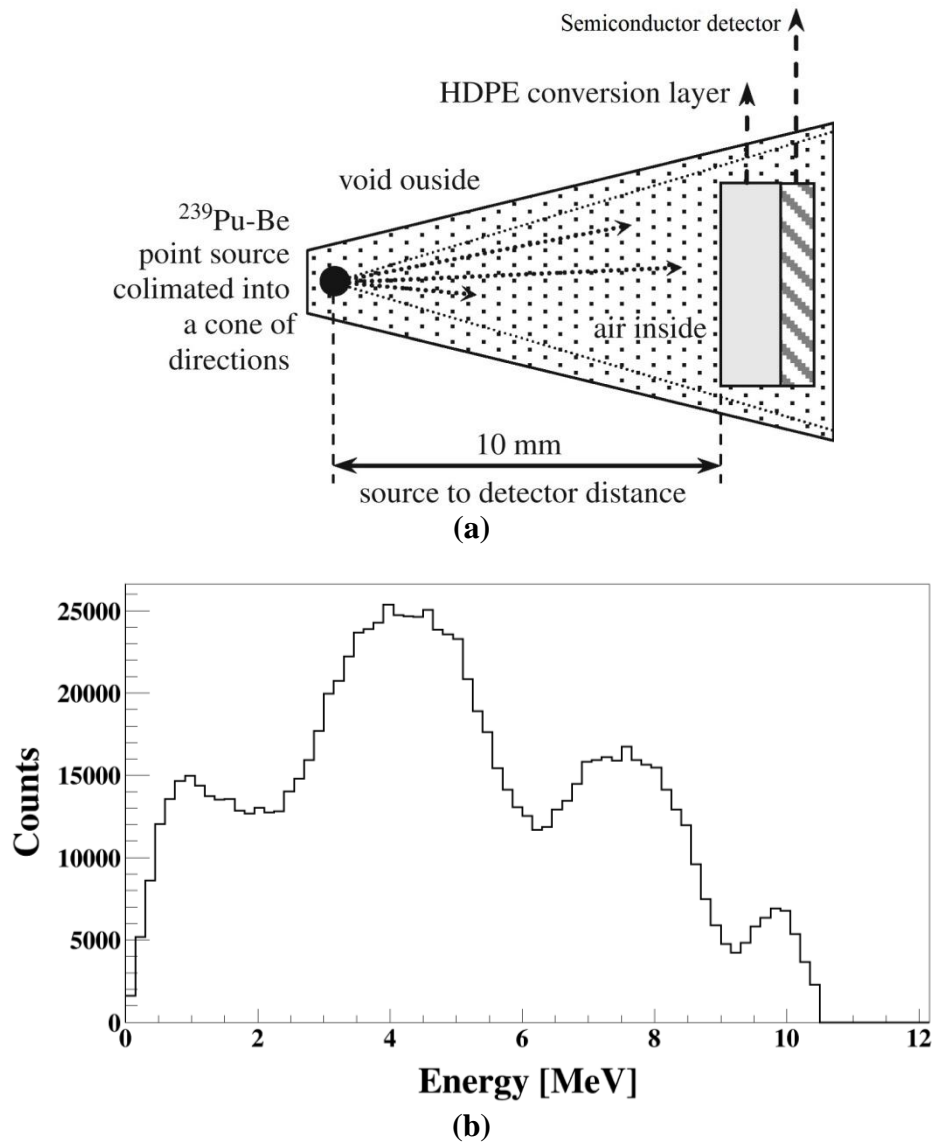
converter material. Therefore, approximately 99.9% of the incident neutrons of energy 1 MeV would interact with the ~ 9–10 cm thick HDPE converter either via elastic or some other reaction mechanism.

#### 4.3.2 HDPE thickness optimization for $^{239}\text{Pu}$ -Be neutron source

K. Sedlackova *et al.*, [50] have optimized the thickness of HDPE for  $^{239}\text{Pu}$ -Be neutron source using MCNPX. The cross-sectional area of the front face of the converter surface is  $3\text{ mm}^2$  and the distance between the neutron source and the detector is 10 mm in their work, as shown in Figure 4.5 (a). We have also created a similar structure in GEANT4. With the help of GPS feature in GEANT4,  $10^6$  collimated point source neutrons from the  $^{239}\text{Pu}$ -Be spectrum (shown in Figure 4.5 (b)) are generated. The neutrons upon interaction with converter, i.e., HDPE, generate recoil protons as a charged particle with specific kinetic energies  $E_p$  (depends on reaction kinematics explained in Chapter 2). These energetic recoil protons tend to deposit/lose its energy in the converter material through columbic interactions (ionization & excitation). Although, with 10 cm thick HDPE all the neutrons may undergo an interaction, but the resultant recoil protons may end up losing all their energy in the HDPE converter itself, thereby, causing the loss of count. The range\* of 1 MeV and 10 MeV energetic recoil protons in HDPE is around  $20\text{ }\mu\text{m}$  and  $1200\text{ }\mu\text{m}$  (0.12 cm), respectively (computed using SRIM2013 and shown in Figure 4.6). Therefore, the majority of the recoil protons which are supposed to reach the SiC active region, end up losing all their energy in the converter itself, resulting in poor efficiency. Hence, there is a need for the optimization of the converter thickness so that the maximum number of recoil protons should reach in the detector active region.

---

\* The particle range is defined as the mean thickness of material, which is usually expressed in terms of mass per unit area, traversed before it comes to rest.



**Figure 4.5 (a) Detector and source setup as described by K. Sedlackova et al. [50], (b) The neutron spectrum of the  $^{239}\text{Pu-Be}$  source.**

The thickness is optimized in terms of neutron detection efficiency ( $\eta_{det}$ ). The  $\eta_{det}$  is estimated at each thickness of HDPE converter. Figure 4.7 illustrates the change in  $\eta_{det}$  with respect to the thickness of the HDPE converter for  $^{239}\text{Pu-Be}$  neutron source. The initial increase in the efficiency is due to the increased interaction rate with increasing thickness. After a certain thickness, the efficiency peaks and starts to decrease gradually. It is due to the fact that some of the low energy recoil protons are unable to reach the detector active region i.e., losing all their energy in converter itself and some of the energetic recoils are leaving the converter from the sides. This is one of the factors which limit the efficiency of

the detector. The thickness corresponding to the maximum efficiency can be regarded as the optimized thickness of the converter.

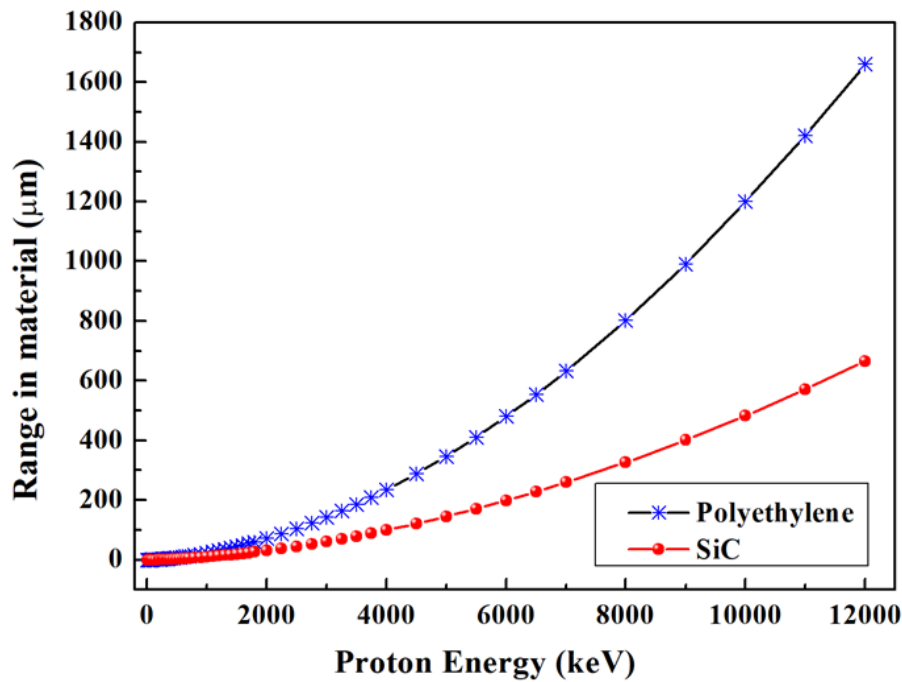


Figure 4.6 Range of proton in HDPE and SiC material (computed using SRIM software).

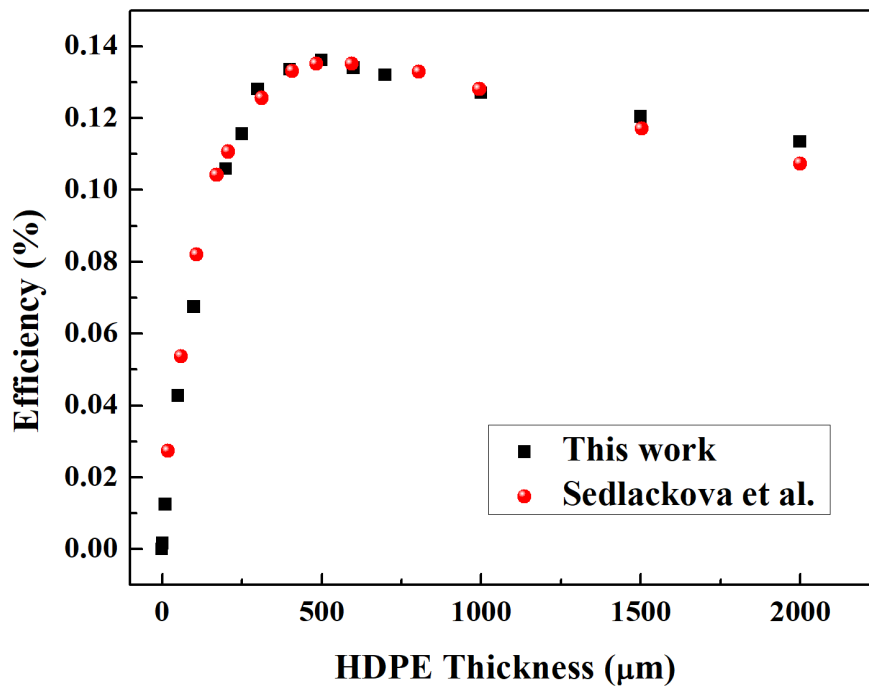
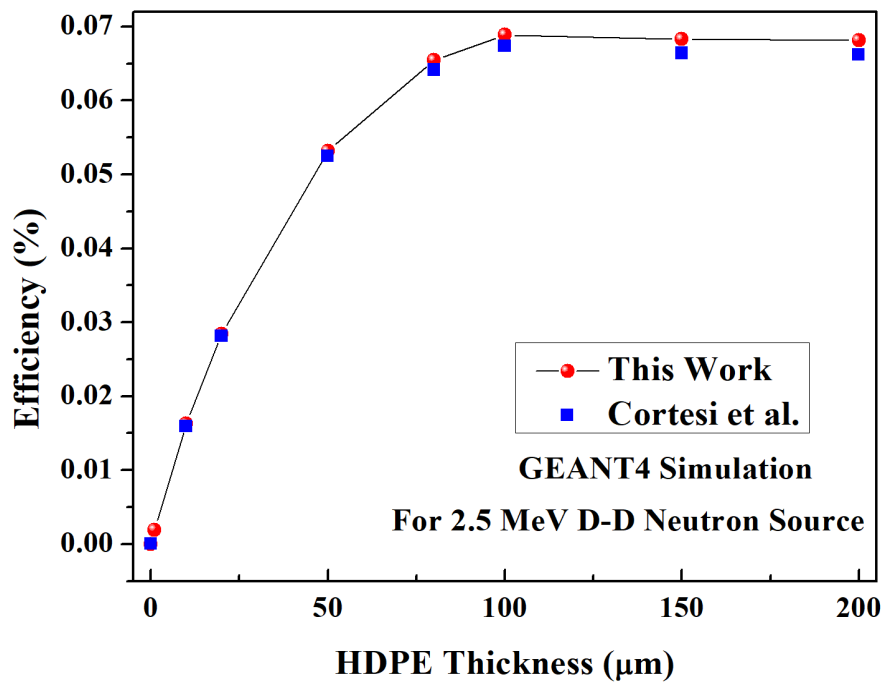


Figure 4.7 Optimization of HDPE thickness for  $^{239}\text{Pu}$ -Be neutron source and estimation of neutron detection efficiency with the help of Monte-Carlo simulation tools: GEANT4 (this work) and MCNPX (K. Sedlackova et al. [50]).

The Figure 4.7 also represents an excellent agreement between the MCNPX based literature result and our GEANT4 simulation result. The maximum efficiency of  $\sim 0.135\%$  is achieved with about  $500\ \mu\text{m}$  thick HDPE layer in both the works.

#### 4.3.3 HDPE thickness optimization for 2.5 MeV D-D neutron source\*

The thickness of HDPE converter is also optimized for the 2.5 MeV mono-energetic neutrons from the D-D source. For this simulation, the cross-sectional area of the front face of the converter is kept at  $1\ \text{cm}^2$ . The 2.5 MeV mono-energetic neutron source is defined in GPS class of GEANT4. The neutron detection efficiency is calculated as a function of varying HDPE thickness for 2.5 MeV neutron source and is depicted in Figure 4.8.



**Figure 4.8** Neutron detection efficiency vs. HDPE converter thickness for 2.5 MeV D-D neutron source and comparison with the GEANT4 simulation work by Cortesi *et al.*, [100].

Our GEANT4 simulation results are in excellent agreement with the other GEANT4 simulation work performed by M. Cortesi *et al.*, [100]. The efficiency of  $\sim 0.07\%$  is achieved at around  $100\ \mu\text{m}$  thickness of HDPE which is similar to the values reported in the

\* Fusion of deuterium atoms (D+D) generates  $^3\text{He}$  ion and a neutron with a kinetic energy of  $\sim 2.5\ \text{MeV}$ .

literature. Flammang *et al.*, [24] have experimented and measured the detector's response as a function of HDPE converter thickness. They have also obtained the best response for the 2.5 MeV D-D neutron source with the 100  $\mu\text{m}$  thick HDPE.

Hence, the simulation results of our modeling using GEANT4 are able to reproduce the results of MCNPX, GEANT4, and experimental work reported in the literature. The results are in excellent agreement with the literature which motivates for extending the GEANT4 simulation work.

#### 4.4 SIMULATION RESULTS AND DISCUSSIONS

This section presents the results of following simulations performed using GEANT4:

- (i) First subsection, i.e., Section 4.4.1 shows the advantage of indirect conversion neutron detector over direct conversion neutron detectors. It also shows various neutron interactions that are happening in SiC and HDPE converter, and resultant secondary particles along with their mean, Q-value, etc.
- (ii) In Section 4.4.2, HDPE-SiC-based detector is simulated as per the methodologies described in the Section 4.2.
- (iii) Since, HDPE cannot work in high-temperature environment. Hence, several other hydrogenous converters namely, Lithium Hydride (LiH), Perylene and Perylene-tetracarboxylic dianhydride (PTCDA) which can be juxtaposed with SiC in harsh conditions are considered. The detection efficiency offered by these converters for  $^{241}\text{Am}$ -Be neutron source is estimated and presented in Section 4.4.3. Based on this study LiH is proposed as a converter for harsh environments.
- (iv) Section 4.4.4 presents the extensive simulation study of the LiH-SiC-based neutron detector as per the methodology described in Section 4.2.



- (v) In Section 4.4.5, it is shown that the energy deposition in SiC active region is higher due to charged particles generated in LiH than the HDPE.
- (vi) In Section 4.4.6, thickness of perylene is optimized for various energy neutron sources. Perylene is proposed as a converter for spectroscopic applications. However, detailed study of perylene-SiC detectors is needed for such applications.
- (vii) Finally, in Section 4.4.7, dependence of detection efficiency on neutron source distribution is shown. This study also shows independence of optimized thickness on source distribution.

#### 4.4.1 Nuclear reactions in Direct and Indirect conversion SiC-based detectors

In direct-conversion SiC-based neutron detectors, Si and C-atoms in SiC can undergo elastic scattering reactions to generate  $^{28}\text{Si}$  or  $^{12}\text{C}$  recoils, respectively, and inelastic scattering reactions to produce  $\alpha$ , protons, and other charged particles in accordance with the particular reaction cross-section [103]. To determine the reactions that are taking place in SiC, a simulation was performed with 1 cm thick SiC. Table 4.1 lists out the nuclear reactions which are happening in SiC due to the  $10^6$  incident neutrons from the  $^{241}\text{Am}$ -Be spectrum (shown in Figure 4.10 (b)). It can be observed that Si and C recoils are generated in more than 90% of the interactions. Table 4.2 represents the list of particles generated along with their mean kinetic energy and range of the kinetic energies at the time of their production.

**Table 4.1 List of nuclear reactions in SiC material for  $10^6$  incident neutrons.**

Nuclear Reactions	Frequency relative to total neutron interactions <sup>a</sup> (%)	<i>Q</i> -value
$n + ^{12}\text{C} \rightarrow n \gamma + ^{13}\text{C}$	0.000427967	-734.52 keV
$n + ^{12}\text{C} \rightarrow n \gamma + \alpha + ^9\text{Be}$	0.145080736	-5.7038 MeV
$n + ^{12}\text{C} \rightarrow n \gamma + n + ^{12}\text{C}$	1.906164005	-231.52 eV
$n + ^{12}\text{C} \rightarrow \alpha + ^9\text{Be}$	0.191729114	-5.7012 MeV
$n + ^{12}\text{C} \rightarrow n + ^{12}\text{C}$	39.50347295	139.26 eV

Nuclear Reactions	Frequency relative to total neutron interactions <sup>a</sup> (%)	<i>Q</i> -value
$n + {}^{13}\text{C} \rightarrow N \gamma + \alpha + {}^{10}\text{Be}$	0.0012839	-3.8359 MeV
$n + {}^{13}\text{C} \rightarrow N \gamma + n + {}^{13}\text{C}$	0.018402571	-260.39 eV
$n + {}^{13}\text{C} \rightarrow \alpha + {}^{10}\text{Be}$	0.001711867	-3.8358 MeV
$n + {}^{13}\text{C} \rightarrow n + {}^{13}\text{C}$	0.416839637	-27.684 keV
$n + {}^{28}\text{Si} \rightarrow N \gamma + {}^{29}\text{Si}$	0.008987302	6.4167 MeV
$n + {}^{28}\text{Si} \rightarrow N \gamma + \alpha + {}^{25}\text{Mg}$	0.259775831	-2.4198 MeV
$n + {}^{28}\text{Si} \rightarrow N \gamma + n + {}^{28}\text{Si}$	10.41585531	-63.193 eV
$n + {}^{28}\text{Si} \rightarrow N \gamma + p + {}^{28}\text{Al}$	0.907289558	-3.6085 MeV
$n + {}^{28}\text{Si} \rightarrow \alpha + {}^{25}\text{Mg}$	0.411276069	-2.7349 MeV
$n + {}^{28}\text{Si} \rightarrow n + {}^{28}\text{Si}$	41.15028909	31.809 eV
$n + {}^{28}\text{Si} \rightarrow p + {}^{28}\text{Al}$	0.397581132	-3.8759 MeV
$n + {}^{29}\text{Si} \rightarrow N \gamma + 2 n + {}^{28}\text{Si}$	0.000855934	-1.149 MeV
$n + {}^{29}\text{Si} \rightarrow N \gamma + \alpha + {}^{26}\text{Mg}$	0.024394106	-31.934 keV
$n + {}^{29}\text{Si} \rightarrow N \gamma + n + {}^{29}\text{Si}$	0.738242683	-48.522 eV
$n + {}^{29}\text{Si} \rightarrow N \gamma + p + {}^{29}\text{Al}$	0.013694937	-2.8964 MeV
$n + {}^{29}\text{Si} \rightarrow \alpha + {}^{26}\text{Mg}$	0.016690704	-89.088 keV
$n + {}^{29}\text{Si} \rightarrow n + {}^{29}\text{Si}$	1.746104432	31.061 eV
$n + {}^{29}\text{Si} \rightarrow p + {}^{29}\text{Al}$	0.017118671	-2.9129 MeV
$n + {}^{30}\text{Si} \rightarrow N \gamma + {}^{31}\text{Si}$	0.000427967	4.3037 MeV
$n + {}^{30}\text{Si} \rightarrow N \gamma + \alpha + {}^{27}\text{Mg}$	0.000855934	-4.2002 MeV
$n + {}^{30}\text{Si} \rightarrow N \gamma + n + {}^{30}\text{Si}$	0.411704035	2.2936 keV
$n + {}^{30}\text{Si} \rightarrow N \gamma + p + {}^{30}\text{Al}$	0.000427967	-6.8197 MeV
$n + {}^{30}\text{Si} \rightarrow \alpha + {}^{27}\text{Mg}$	0.001711867	-4.2538 MeV
$n + {}^{30}\text{Si} \rightarrow n + {}^{30}\text{Si}$	1.29160372	25.478 eV

<sup>a</sup> The total number of neutron interactions is 233663. Here N is number of Gamma; N = 1→8. Negative *Q*-value indicates the threshold reactions

**Table 4.2 List of generated particles in SiC with their mean kinetic energy for 10<sup>6</sup> incident neutrons.**

Generated Particles	Number	Mean Kinetic Energy	Range of Kinetic Energy
<sup>28</sup> Al	3049	367.77 keV	16.171 keV → 1.1204 MeV
<sup>29</sup> Al	72	349.65 keV	28.833 keV → 1.0893 MeV
<sup>30</sup> Al	1	581.19 keV	581.19 keV → 581.19 keV
<sup>10</sup> Be	7	1.2123 MeV	160.58 keV → 2.1968 MeV
<sup>9</sup> Be	787	1.1595 MeV	14.152 keV → 3.137 MeV
<sup>12</sup> C	96759	395.14 keV	0.34078 eV → 2.9473 MeV
<sup>13</sup> C	1018	347.16 keV	180.32 eV → 2.4177 MeV

Generated Particles	Number	Mean Kinetic Energy	Range of Kinetic Energy
$^{25}\text{Mg}$	1568	876.6 keV	43.409 keV $\rightarrow$ 2.3849 MeV
$^{26}\text{Mg}$	96	928.07 keV	110.96 keV $\rightarrow$ 2.0859 MeV
$^{27}\text{Mg}$	6	788.25 keV	194.37 keV $\rightarrow$ 1.5206 MeV
$^{28}\text{Si}$	120493	145.37 keV	0.26237 eV $\rightarrow$ 1.3631 MeV
$^{29}\text{Si}$	5826	154.35 keV	15.233 eV $\rightarrow$ 1.1235 MeV
$^{30}\text{Si}$	3980	139.39 keV	2.4636 eV $\rightarrow$ 1.1573 MeV
$^{31}\text{Si}$	1	70.041 keV	70.041 keV $\rightarrow$ 70.041 keV
$\alpha$	2464	3.428 MeV	197.08 keV $\rightarrow$ 8.2182 MeV
$\gamma$	49939	1.5854 MeV	406.57 eV $\rightarrow$ 8.9998 MeV
$n$	31526	2.9368 MeV	6.335 keV $\rightarrow$ 9.4629 MeV
$p$	3122	3.153 MeV	238.19 keV $\rightarrow$ 7.5591 MeV

Furthermore, a hydrogen-rich neutron converter material such as HDPE can be coated above the active region of the SiC-based detector to form an indirect-conversion neutron detector [24]. Table 4.3 represents the reactions, which are happening in 1 cm thick HDPE upon interaction with the incident neutrons of  $^{241}\text{Am}$ -Be source. It is evident that the elastic scattering reactions of neutrons with hydrogen which generate recoil protons is dominating ( $\sim 72\%$ ). This is because, for fast neutrons, the elastic scattering cross section is higher than other reaction cross-sections. In addition to this, neutrons will also undergo elastic scattering reaction with Carbon nuclei, which is the next reaction in terms of dominance ( $\sim 26\%$ ). Other than these reactions, neutron will also undergo several inelastic scattering reactions with Carbon and Hydrogen nuclei [ $^{12}\text{C}(n, n')^{12}\text{C}$ ;  $^{13}\text{C}(n, n')^{13}\text{C}$ ;  $^2\text{H}(n, n')^2\text{H}$ ] and a very few  $(n, \alpha)$  reactions [ $^{12}\text{C}(n, \alpha)^9\text{Be}$ ;  $^{13}\text{C}(n, \alpha)^{10}\text{Be}$ ] due to very low cross-sections. Some reactions have negative Q-value, which shows these reactions will occur only when the incident neutrons will have energy equal to or greater than the threshold energy. Table 4.4 shows the list of particles generated due to neutron interaction with HDPE along with their mean kinetic energy and range of the kinetic energies at the time of their production.

**Table 4.3 List of nuclear reactions in HDPE converter for  $10^6$  incident neutrons.**

Nuclear Reactions	Frequency relative to total neutron interactions <sup>a</sup> (%)	<i>Q</i> -value
$n + {}^{12}\text{C} \rightarrow N \gamma + {}^{13}\text{C}$	0.0010	186.34 keV
$n + {}^{12}\text{C} \rightarrow N \gamma + \alpha + {}^9\text{Be}$	0.1017	-5.7038 MeV
$n + {}^{12}\text{C} \rightarrow N \gamma + n + {}^{12}\text{C}$	1.3493	-290.49 eV
$n + {}^{12}\text{C} \rightarrow \alpha + {}^9\text{Be}$	0.1291	-5.7012 MeV
$n + {}^{12}\text{C} \rightarrow n + {}^{12}\text{C}$	26.2475	144.32 eV
$n + {}^{13}\text{C} \rightarrow N \gamma + \alpha + {}^{10}\text{Be}$	0.0010	-3.8386 MeV
$n + {}^{13}\text{C} \rightarrow N \gamma + n + {}^{13}\text{C}$	0.0131	-230.71 eV
$n + {}^{13}\text{C} \rightarrow \alpha + {}^{10}\text{Be}$	0.0017	-3.8353 MeV
$n + {}^{13}\text{C} \rightarrow n + {}^{13}\text{C}$	0.2885	-28.831 keV
$n + {}^1\text{H} \rightarrow N \gamma + {}^2\text{H}$	0.0003	578.25 keV
$n + {}^1\text{H} \rightarrow n + p$	71.8599	840.86 eV
$n + {}^2\text{H} \rightarrow n + {}^2\text{H}$	0.0064	429.84 eV

<sup>a</sup> The total number of neutron interactions is 281108. Here *N* is number of Gamma; *N* = 1 → 4. Negative *Q*-value indicates the threshold reactions

**Table 4.4 List of generated particles in HDPE with their mean kinetic energy for  $10^6$  incident neutrons.**

Generated Particles	Number	Mean Kinetic Energy	Range of Kinetic Energy
${}^{10}\text{Be}$	8	1.4649 MeV	303.12 keV → 2.7232 MeV
${}^9\text{Be}$	649	1.1741 MeV	9.0611 keV → 3.5147 MeV
${}^{12}\text{C}$	77577	409.14 keV	1.3303 eV → 2.9667 MeV
${}^{13}\text{C}$	851	360.36 keV	897.91 eV → 2.5871 MeV
$\alpha$	657	1.8154 MeV	206.39 keV → 4.8089 MeV
${}^2\text{H}$	19	1.5774 MeV	151.93 keV → 5.3214 MeV
$\gamma$	10607	1.6236 MeV	1.0013 keV → 9.142 MeV
$n$	3830	2.2004 MeV	31.444 keV → 6.1871 MeV
$p$	202004	1.5502 MeV	1.0023 eV → 10.726 MeV

As evident from the Table (4.1–4.4) that the recoil protons with higher kinetic energy and range are generated in significant number in indirect-conversion setup, therefore, SiC-detector coupled with hydrogen-rich converter material will offer better efficiency than the direct-conversion setup. Also, the maximum energy of the generated recoil proton is ~11 MeV which can have a range of ~ 570  $\mu\text{m}$  in SiC (see Figure 4.6). Therefore, in order to capture the full energy of recoil protons SiC region is kept at 600  $\mu\text{m}$ .

Furthermore, a data analysis framework, known as ROOT, has been integrated with GEANT4 to plot the histograms of the energy deposition by several particles for different geometries of the detector. Figure 4.9 represents the histograms of total energy deposited, energy deposited by the recoil protons (generated in HDPE converter), and energy deposited by other charged reaction products in SiC active region, respectively.

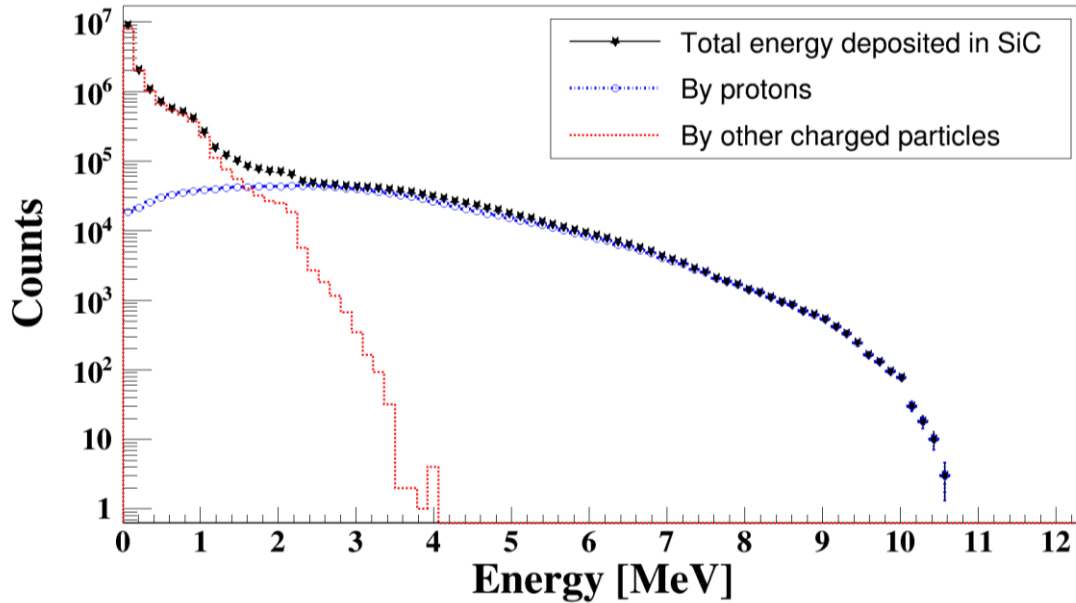


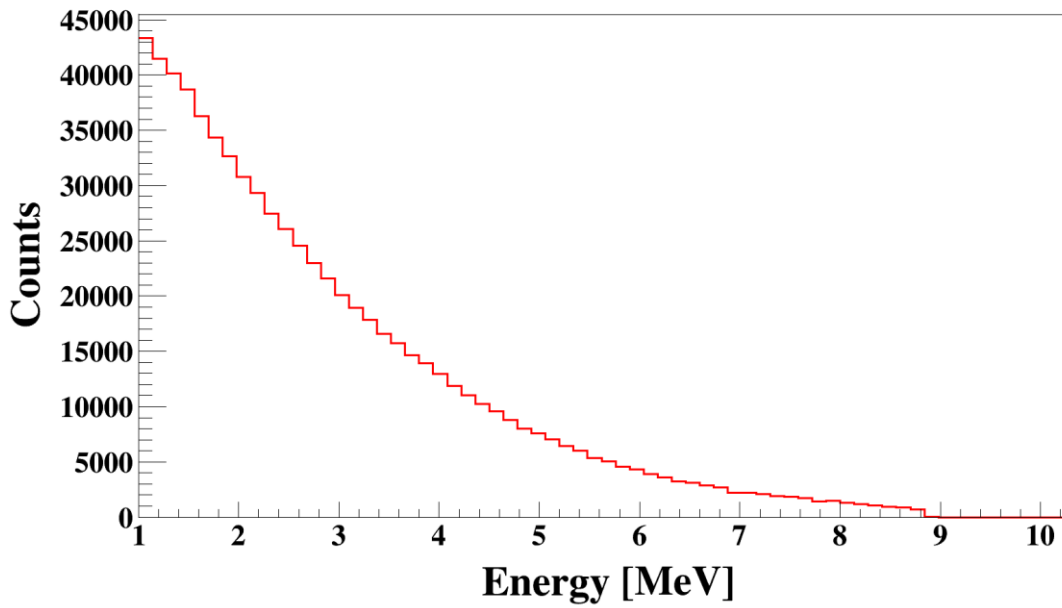
Figure 4.9 Energy deposited in SiC by all particles (★), recoil protons (○), and other charged particles (dotted line).

#### 4.4.2 HDPE as a converter (HDPE-SiC-based detector)

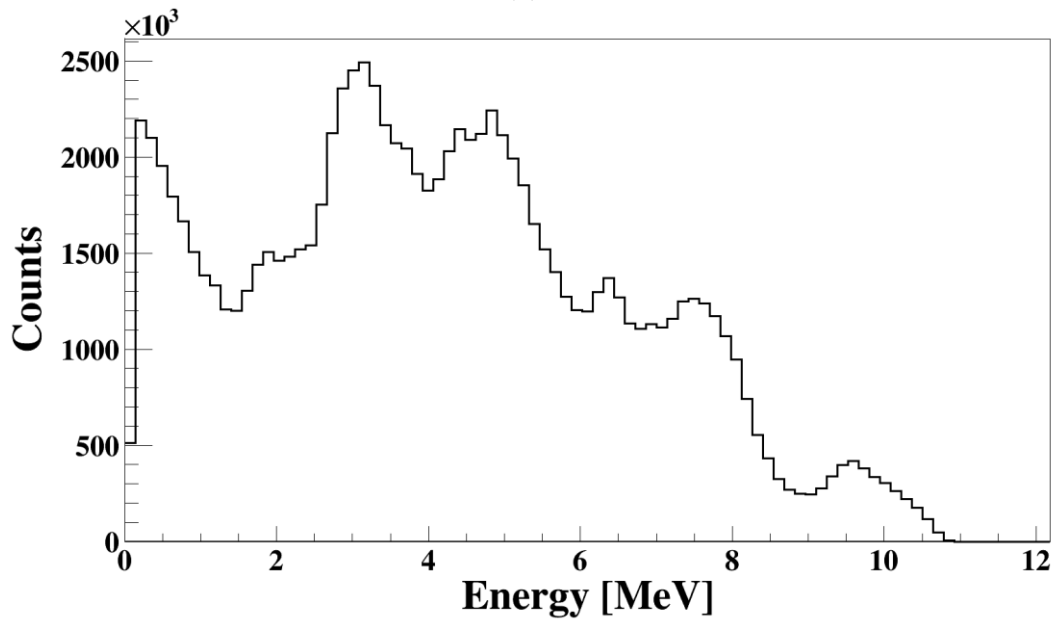
##### 4.4.2.1 Optimization of HDPE thickness and efficiency estimation

The GEANT4 simulations have been extended for different mono-energetic (0.5 to 10, and 14 MeV) as well as standard neutron sources such as  $^{252}\text{Cf}$  and  $^{241}\text{Am-Be}$  [104] (see Figure 4.10). Figure 4.11 (a) shows the detection efficiency variation with respect to HDPE thickness for  $^{252}\text{Cf}$  and  $^{241}\text{Am-Be}$  neutron sources. The optimized thickness for  $^{241}\text{Am-Be}$  neutron source is found to be  $\sim 500 \mu\text{m}$ , which is in good agreement to the value of  $580 \mu\text{m}$  reported in the literature by T.M. Filho *et al.*, [25]. Figure 4.11 (b) depicts the dependence of the optimized thickness of the converter on the incident neutron energy. The detection

efficiency for different energy neutrons peaks at different thicknesses of converter layer. It is due to the dependence of cross-section on neutron energies. Therefore, it is challenging to design a neutron detector which can be applicable for a broad energy spectrum of the neutrons. For detection of the unknown spectra, such as in typical fast test reactor having maximum neutron of energy  $\sim 10$  MeV and central peak around few hundreds of keV, a HDPE thickness of  $\sim 400$   $\mu\text{m}$  is selected from the Figure 4.11 (b).

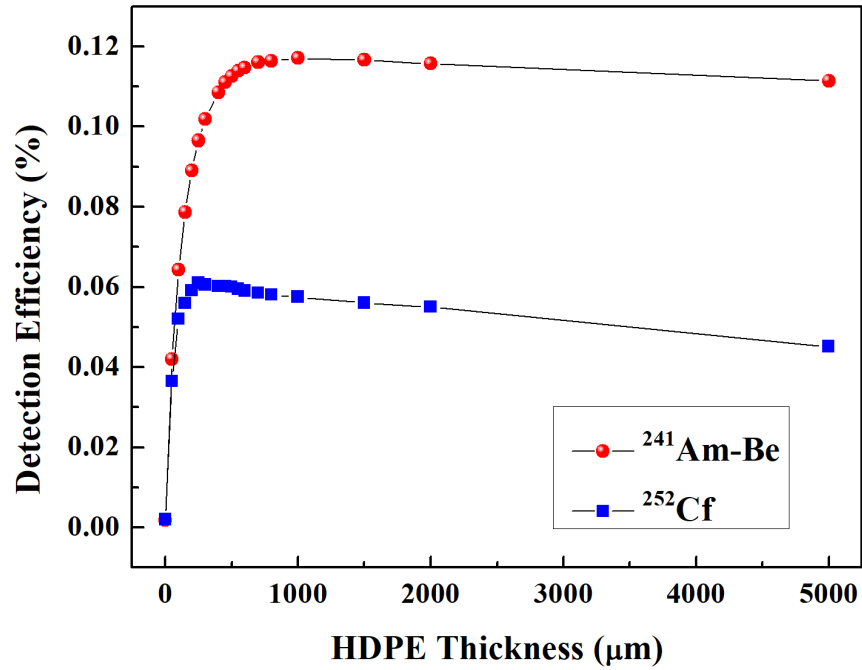


(a)

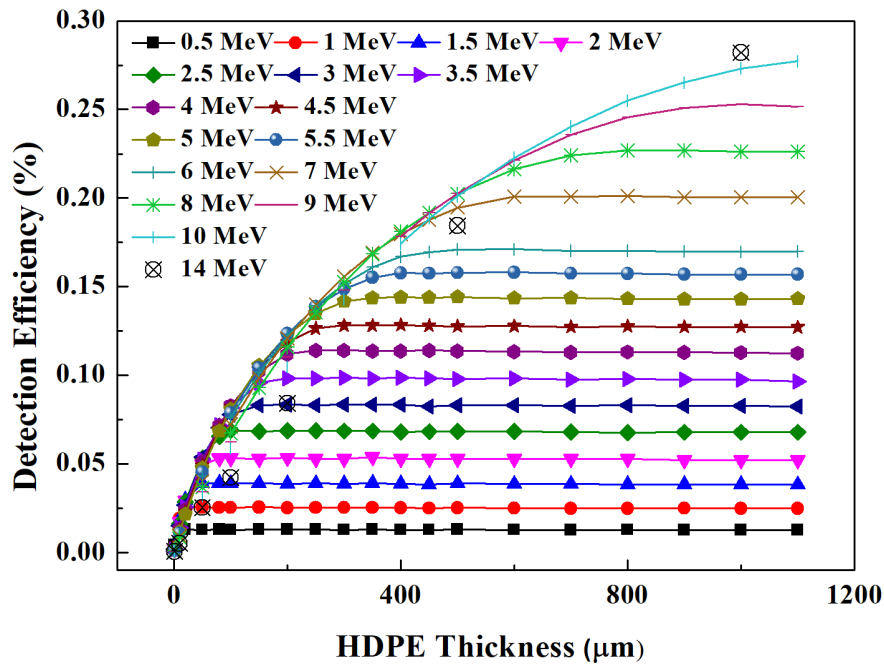


(b)

**Figure 4.10** Spectrum of (a)  $^{252}\text{Cf}$  and (b)  $^{241}\text{Am-Be}$  neutron sources [104].



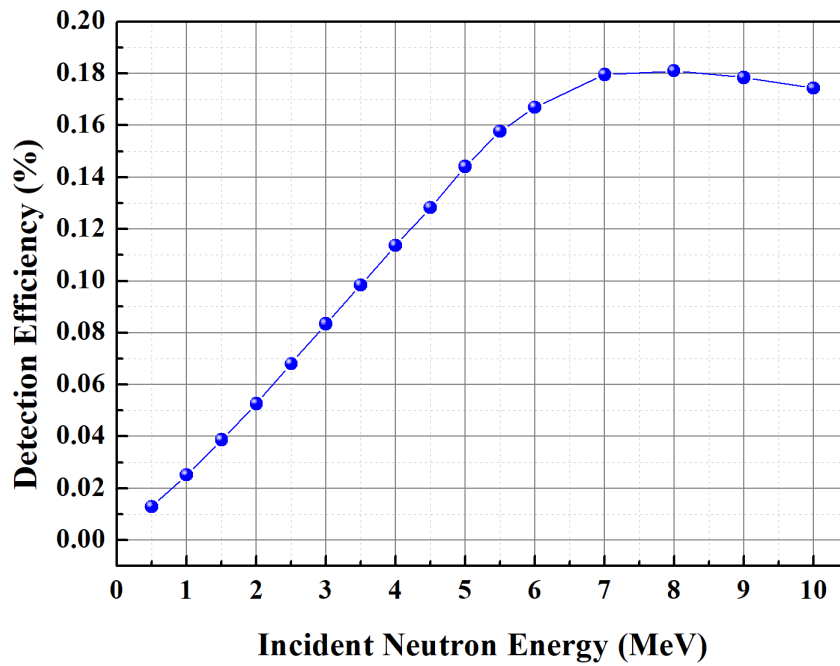
(a)



(b)

**Figure 4.11 Optimization of HDPE thickness for (a) <sup>252</sup>Cf and <sup>241</sup>Am-Be (b) various mono-energetic ( $E_n = 0.5$  to 10, and 14 MeV) neutron sources.**

The efficiency of neutron detector with 400 μm thick HDPE converter with respect to different mono-energetic neutron sources is shown in Figure 4.12. It can be observed that with 400 μm thick HDPE converter, maximum efficiency of ~ 0.18% can be achieved for up to 7 MeV neutron sources.



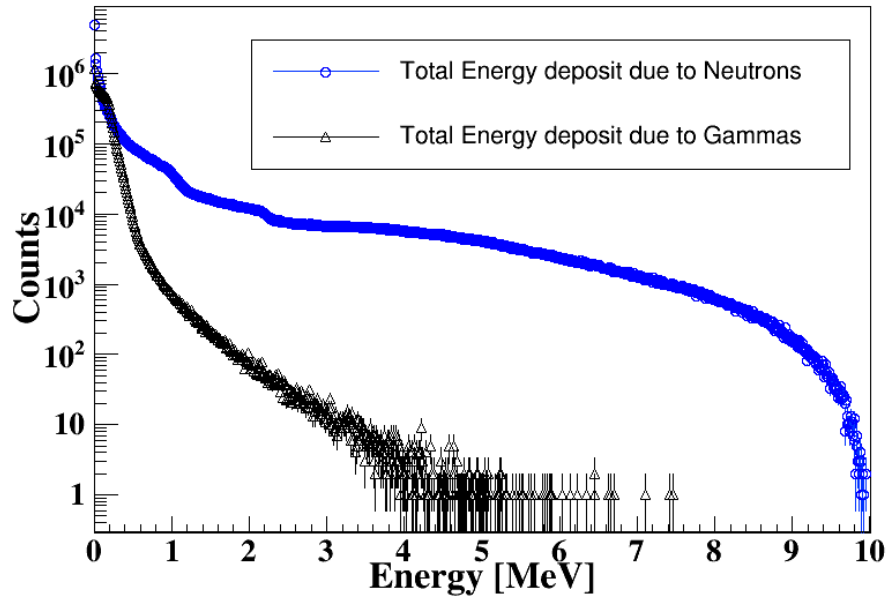
**Figure 4.12** Efficiency of neutron detector with a 400  $\mu\text{m}$  thick HDPE converter for different mono-energetic neutron sources.

#### 4.4.2.2 Effect of $\gamma$ -discrimination on efficiency

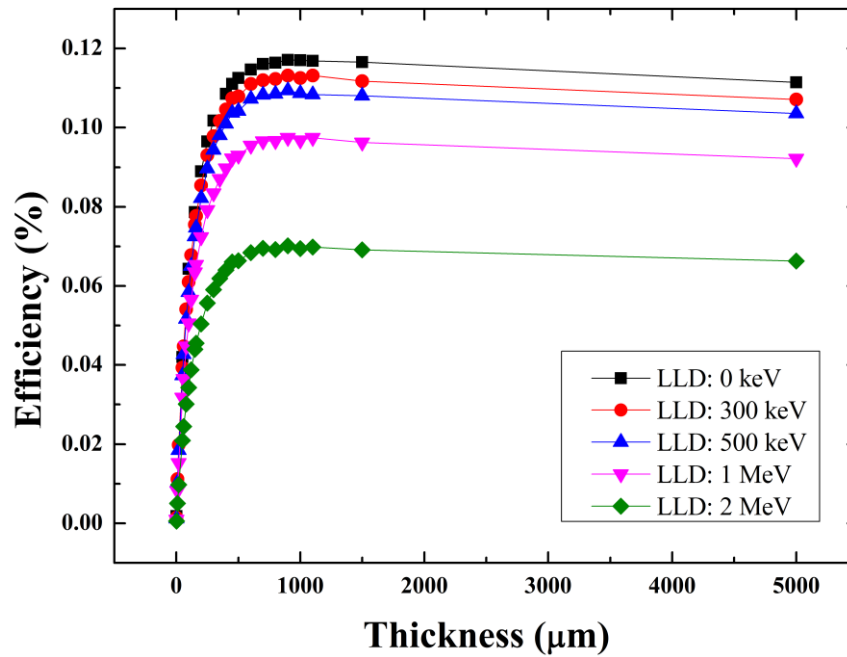
To analyze the effect of  $\gamma$ -background discrimination on neutron detection efficiency, a mixed neutron-gamma source is generated as defined in Section 4.2.2 (Figure 4.2). Figure 4.13 shows the histogram of the total energy deposition in the SiC detector region due to the gamma and neutron induced events. The spectrum due to gamma events has mean energy  $\sim 148$  keV and it contains electrons due to Photoelectric and Compton effects. They are quite dominant and comparable to neutron-induced events (counts), having mean energy  $\sim 3.2$  MeV, in the low energy region (below 1 MeV). Between 1 and 2 MeV, the difference in counts is quite evident and can easily be discriminated by implementing LLD (see Section 4.2.2). Beyond 2 MeV, the counts due to gamma events are negligible. Figure 4.14 shows the effect of LLD on HDPE-SiC detector's efficiency. It is observed that by increasing the LLD threshold to higher energy levels, the background radiations of  $\gamma$ -rays and other charged particles are eliminated, but at the same time, some of the recoil protons are inevitably discriminated which results in a decrease in the detection efficiency.



Therefore, the detector with a finite discrimination level always has a slightly lower efficiency. As can be seen, at the LLD value of 2 MeV, the efficiency is reduced to  $\sim 0.07\%$  from  $0.112\%$ .



**Figure 4.13** Comparison of energy deposition in detector's active region (histograms) due to gamma ( $E_{\text{mean}} = \sim 148 \text{ keV}$ ) and neutron ( $E_{\text{mean}} = \sim 3.2 \text{ MeV}$ ) events.



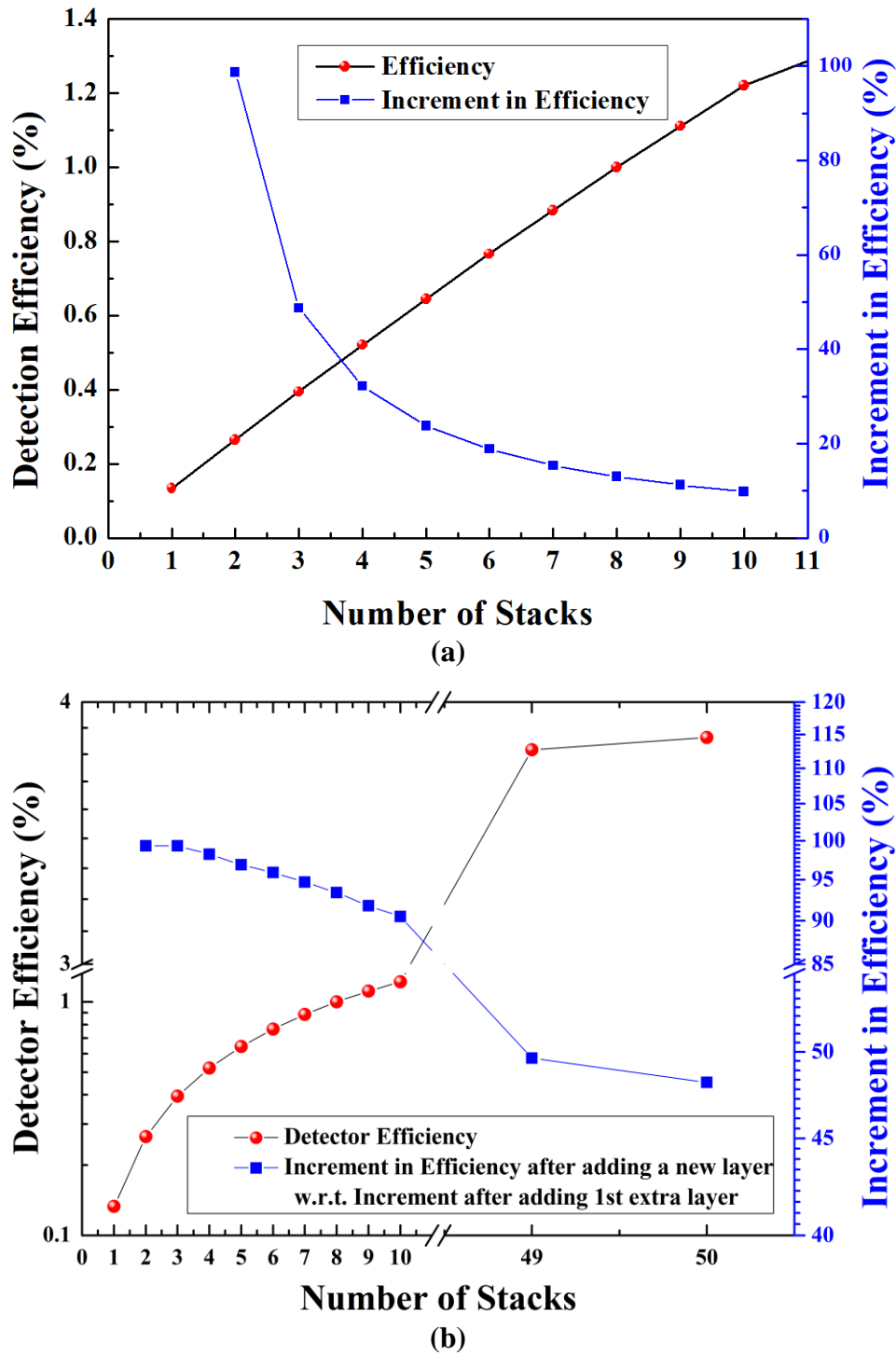
**Figure 4.14** Effect of LLD on HDPE-SiC-based detector efficiency.

### 4.4.2.3 HDPE-SiC-based Stacked detector simulation for higher efficiency

Furthermore, to enhance the efficiency of the detector, stacked detector (Figure 4.3) simulations (as explained in section 4.2.3) have been carried out. The improvement in neutron detection efficiency is estimated by increasing the number of stacked layers and illustrated in Figure 4.15 (a). From Figure 4.15, it is apparent that as the number of stacks increases the efficiency also increases, but non-linearly. As the number of stacks is increased from 1 to 2, the increment in efficiency is almost double, i.e., the efficiency increases from 0.112% to 0.23%. The increment in efficiency with respect to previous layer is  $\sim 99.33\%$ . Further, from second-stack to third-stack, the increment is reduced to 50%. In other words, the efficiency increases to 0.32% with 3 layers of stacked detector in comparison to 0.23% of 2 layers of stacked detector. Similarly, from ninth-stack to tenth-stack, the increase is just 10%. This shows that after a certain number of layers the efficiency saturates eventually. This may be due to the fact that the probability of interaction for neutron with HDPE will saturate at a certain thickness as shown in Figure 4.4. Also, each HDPE layer will attenuate some fraction of incident neutron flux thereby decreasing the incident flux for subsequent converter layers. The authors in [102] have shown a similar effect in the case of thermal neutron detector with  $^{10}\text{B}$  and  $^6\text{LiF}$  converters. Thus, the stacked structure must have a reasonable amount of detectors in order to cope up with power supply and processing electronics. Figure 4.15 (b) illustrates the increment in the efficiency of HDPE-SiC detector after adding a new layer with respect to the increment in the efficiency obtained after adding the 1<sup>st</sup> extra layer, i.e., with respect to adding the 2<sup>nd</sup> layer. Thus, the detection efficiency of  $\sim 1.04\%$  can be achieved with 10 layers of the HDPE-SiC-stacked detector.

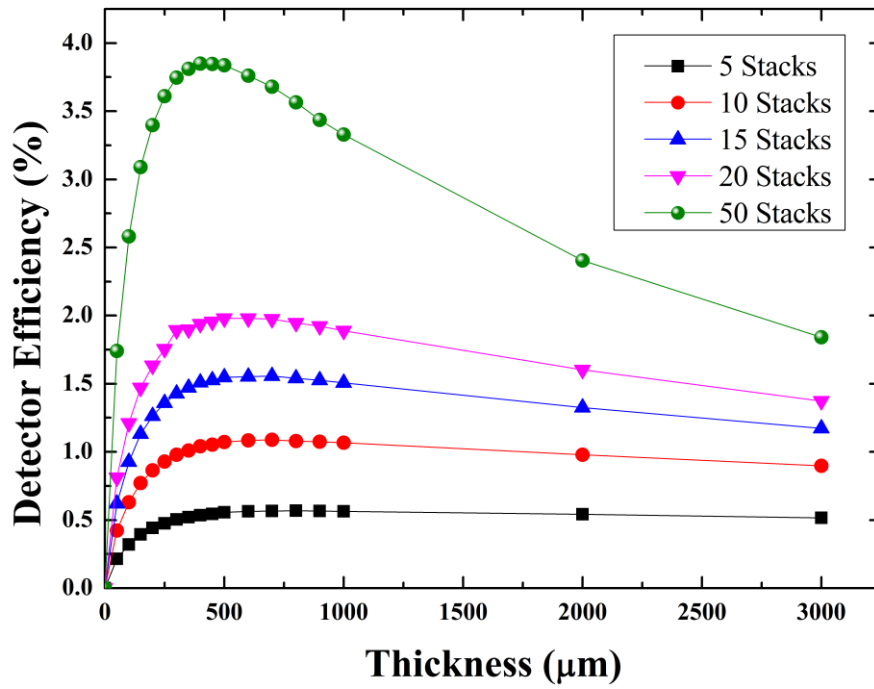
In order to further enhance the efficiency, stacked detectors of different layers viz., 5, 10, 15, 20, and 50, have been simulated for different converter thicknesses. The maximum

efficiency of  $\sim 3.85\%$  has been achieved with 50 layers in the stack and with  $450\ \mu\text{m}$  thick HDPE converter. The efficiency of different stacked detectors concerning converter thicknesses is represented in Figure 4.16.



**Figure 4.15 Increment in the efficiency of HDPE-SiC detector with various stacked layers.**

(a) The percentage increment in efficiency upon increasing the number of layers. (b) The percentage increment in efficiency after adding a new layer with respect to the increment in efficiency obtained after adding the 1<sup>st</sup> extra layer, i.e., w.r.t. adding a 2<sup>nd</sup> layer.



**Figure 4.16** Efficiency variation with respect to converter thicknesses for a stacked detector with different number of stacked layers viz., 5, 10, 15, 20 and 50.

#### 4.4.3 Study of other hydrogenous converters for harsh environments

The HDPE-SiC-based detector could not be employed in the high-temperature environment because the HDPE cannot sustain temperature higher than  $\sim 70\text{--}90^\circ\text{C}$  and could eventually meltdown over  $110^\circ\text{C}$ . Therefore, this section explores various hydrogenous converter materials viz., (a) HDPE, (b) LiH, (c) Perylene and, (d) PTCDA, which can be juxtaposed with SiC to detect fast neutrons in harsh environments.

LiH is an effective neutron shielding material for weight-sensitive reactor applications, such as on-board space reactors. LiH has high hydrogen content (12.68 wt. % H in LiH) and a high number of H-atoms/ $\text{cm}^3$  ( $5.85 \times 10^{22} \text{ cm}^{-3}$ ) which can aid in recoil-proton generation upon interaction with fast neutrons [105]. Perylene ( $\text{C}_{20}\text{H}_{12}$ ) is an organic semiconductor material, having good optical properties and, excellent thermal and chemical stability. It is usually deployed as a blue emitting dopant material in Organic LEDs. Kargar *et al.*, have reported a direct-configuration fast neutron sensor based on perylene [106].

PTCDA (an organic semiconductor) is a compound of perylene which is also reported to be used as direct conversion fast neutron detector [107]. Physical and electrical properties of the selected converter materials are tabulated in Table 4.5.

**Table 4.5 Properties of various neutron converter materials.**

Properties	Neutron Converter Materials			
	HDPE	LiH	Perylene	PTCDA
Chemical Formula	(C <sub>2</sub> H <sub>4</sub> ) <sub>n</sub>	LiH	C <sub>20</sub> H <sub>12</sub>	C <sub>24</sub> H <sub>8</sub> O <sub>6</sub>
Density (g/cm <sup>3</sup> )	0.96	0.78	1.286	1.7
Melting Point (°C)	115–135	688.7	274	350
Thermal Coefficient of Expansion (/°C)	100–220 × 10 <sup>-6</sup>	41 × 10 <sup>-6</sup>	–	–
Electron Mobility (cm <sup>2</sup> /V-s)	–	–	5.5 at 60K	3 × 10 <sup>-2</sup>
Hole Mobility (cm <sup>2</sup> /V-s)	–	–	87.4 at 60K	–
Hydrogen (wt. %)	14.37	12.68	4.79	2.06

GEANT4 simulations have been carried out to estimate the maximum neutron detection efficiency (as expressed by equation 4.1) which can be achieved from the studies of several hydrogenous neutron converter materials. The planar detector setup is same as described in Section 4.2.1. The efficiency has been estimated for these converters at different thicknesses for <sup>241</sup>Am-Be neutron source and is illustrated in Figure 4.17. It is observed from the figure, that LiH provides neutron detection efficiency significantly close to what HDPE has offered. The efficiency of ~ 0.101% has been achieved with LiH converter in comparison to the efficiency of ~ 0.112% obtained with HDPE converter. On the other hand, the efficiency offered by perylene and its compound PTCDA is ~ 0.04% and ~ 0.02%, respectively. The optimum thickness of various converters for <sup>241</sup>Am-Be neutron source can also be estimated from Figure 4.17. The optimized thickness of LiH, Perylene, and PTCDA, is found to be ~ 500 µm, ~ 400 µm, and ~ 350 µm, respectively.

As apparent from Figure 4.17 and Table 4.5, LiH can provide efficiency very close to the efficiency offered by HDPE, and it can also sustain temperature higher than HDPE, because of the high melting point (~ 680 °C). The next material in terms of neutron

detection efficiency is perylene. The following subsection is devoted to the detailed simulation studies of the LiH as a neutron converter material for SiC-based detectors for applications in harsh environments.

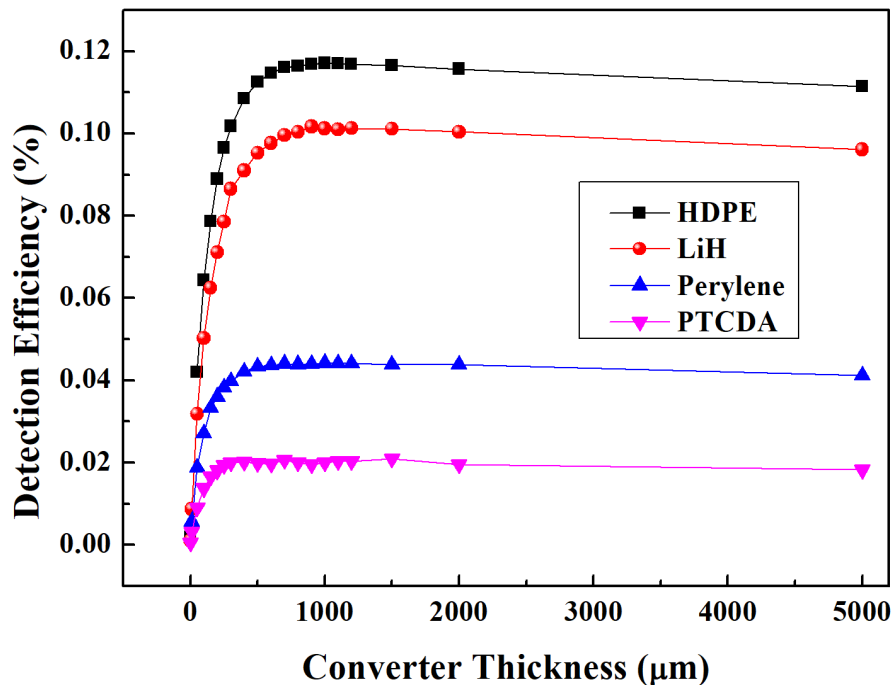


Figure 4.17 Comparison of detection efficiency offered by selected converter materials.

#### 4.4.4 LiH as a converter (LiH-SiC-based detector)

In LiH, the element Lithium encompasses two isotopes namely,  $^6\text{Li}$  and  $^7\text{Li}$  with a weight percentage of 7.59% and 92.41%, respectively. The  $^7\text{Li}$ -isotope, which is in abundance, is entirely transparent to the thermal as well as fast neutrons. Therefore, the majority of the neutrons will interact with the hydrogen content of the LiH and will generate recoil protons, which will be collected in SiC active region to form the detector signal. Table 4.6 shows the reactions that are taking place in LiH following the interactions with the neutrons of the  $^{241}\text{Am}$ -Be spectrum. It is observed from the table that elastic scattering reaction, which generates a recoil proton, is dominant (~ 54%), followed by the reaction producing  $^7\text{Li}$  (35–42%). It should be noted that the maximum energy of the recoil proton generated through the elastic scattering reaction can be equal to the energy of

incident neutron (in case of head-on collision with the hydrogenous material) [5], [9]. Since, the  $^{241}\text{Am}$ -Be spectrum contains neutrons up to 11 MeV, therefore, the maximum kinetic energy of the generated recoil proton can be up to 11 MeV, depending upon the angle of interaction. Similarly, the  $^7\text{Li}$  recoil can be generated with the maximum energy of 4.375 MeV. The range of  $^7\text{Li}$  ion of energy 4.375 MeV in LiH is  $\sim 20\ \mu\text{m}$  whereas the recoil proton of similar energy can traverse easily up to  $\sim 450\ \mu\text{m}$  in LiH (calculated using SRIM package [108] and shown in Figure 4.18). Thus, the recoil protons will easily punch through the converter region and deposit its energy in the detector active region. In spite of the fact that recoil proton can travel a longer distance in the converter, a thick LiH converter layer cannot be deployed because, as described earlier, the protons will lose out a substantial amount of energy in the converter layer. Also, the protons with low kinetic energy may lose all its energy in the converter itself, resulting in loss of counts. Therefore, GEANT4 Monte-Carlo simulations have been carried out to optimize the thickness of LiH.

**Table 4.6 List of Nuclear reactions happening in LiH material for  $10^6$  incident neutrons.**

Nuclear Reactions	Frequency <sup>a</sup>	Q-value
$n + ^1\text{H} \rightarrow \text{N}\gamma + ^2\text{H}$	0.00083	-995.22 keV
$n + ^1\text{H} \rightarrow n + p$	54.3826	802.88 eV
$n + ^2\text{H} \rightarrow n + ^2\text{H}$	0.0070	441.88 eV
$n + ^6\text{Li} \rightarrow \text{N}\gamma + n + ^6\text{Li}$	0.7642	-168.21 eV
$n + ^6\text{Li} \rightarrow \text{N}\gamma + p + 2n + \alpha$	0.0020	-3.6982 MeV
$n + ^6\text{Li} \rightarrow \text{N}\gamma + p + ^6\text{He}$	0.0028	-2.7269 MeV
$n + ^6\text{Li} \rightarrow \alpha + ^3\text{H}$	0.3197	4.2816 MeV
$n + ^6\text{Li} \rightarrow n + ^6\text{Li}$	2.2779	147.41 eV
$n + ^6\text{Li} \rightarrow p + 2n + \alpha$	0.0144	4.1932 MeV
$n + ^6\text{Li} \rightarrow p + ^6\text{He}$	0.0186	-2.7261 MeV
$n + ^7\text{Li} \rightarrow 2n + ^6\text{Li}$	0.0028	-6.8341 MeV
$n + ^7\text{Li} \rightarrow \text{N}\gamma + 2n + ^6\text{Li}$	0.0033	-7.25 MeV
$n + ^7\text{Li} \rightarrow \text{N}\gamma + ^2\text{H} + ^6\text{He}$	0.0008	-7.7515 MeV
$n + ^7\text{Li} \rightarrow \text{N}\gamma + n + ^7\text{Li}$	6.6635	-173.94 eV
$n + ^7\text{Li} \rightarrow n + ^7\text{Li}$	35.5387	145.22 eV

<sup>a</sup> Frequency is relative to the total number of neutron interactions, which is, 241,404. N = Number of  $\gamma$ -rays. Negative *Q-value* indicates the threshold reactions.

#### 4.4.4.1 Optimization of LiH thickness and efficiency estimation

GEANT4 simulations are performed to optimize the LiH thickness for different mono-energetic neutron beams (0.5 to 10 MeV & 14 MeV) and  $^{241}\text{Am}$ -Be standard neutron sources and are illustrated in Figure 4.19 and Figure 4.20, respectively. It is observed from the figure that the detector efficiency is gradually decreasing after a specific thickness of the converter. It is due to the fact that some of the low energy recoil protons are unable to reach the detector active region and some of the energetic recoils are leaving the converter layer from the sides. Hence, some of the generated recoil protons are unable to reach the active region of SiC detector and thus results in a loss of count. This is one of the factors which limit the efficiency of the detector. The detection efficiency eventually becomes zero when the converter thickness exceeds the mean free path of maximum energy neutron from the source, plus, the range of maximum energy recoil proton in the converter.

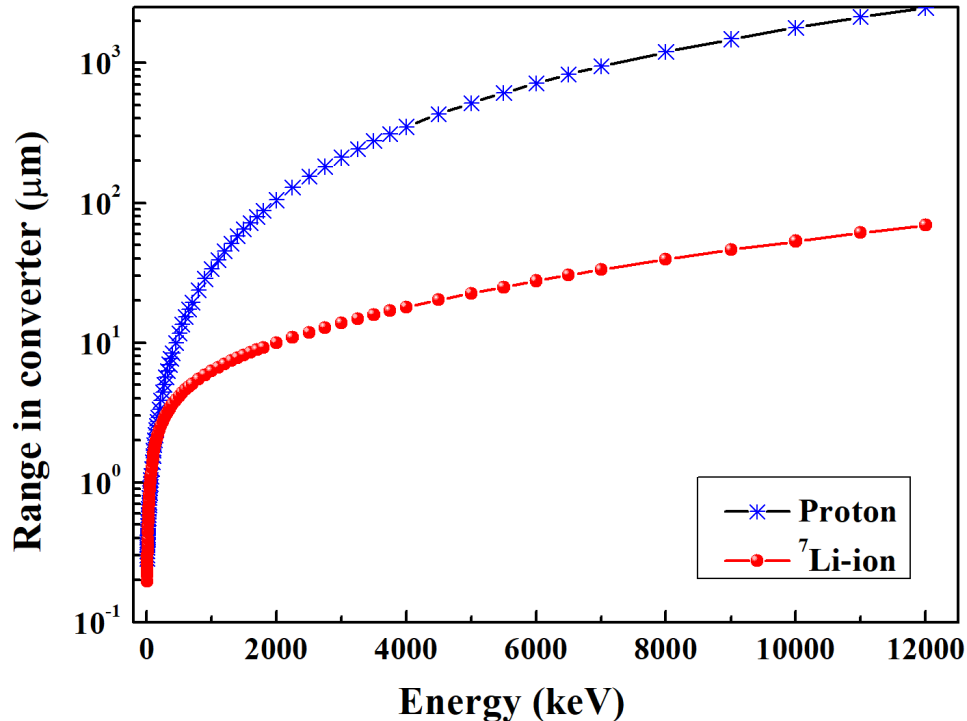


Figure 4.18 Range of protons and  $^7\text{Li}$  ion in LiH converter material (calculated using SRIM package).



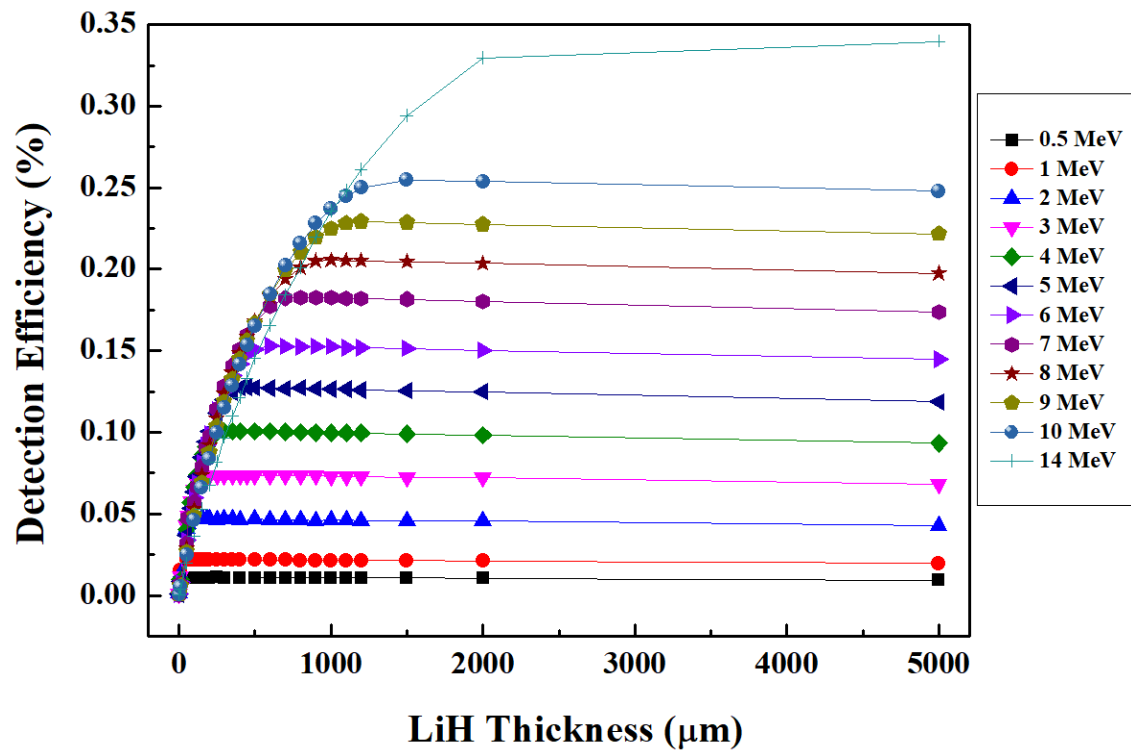


Figure 4.19 Efficiency vs. LiH thickness for different mono-energetic neutron sources.

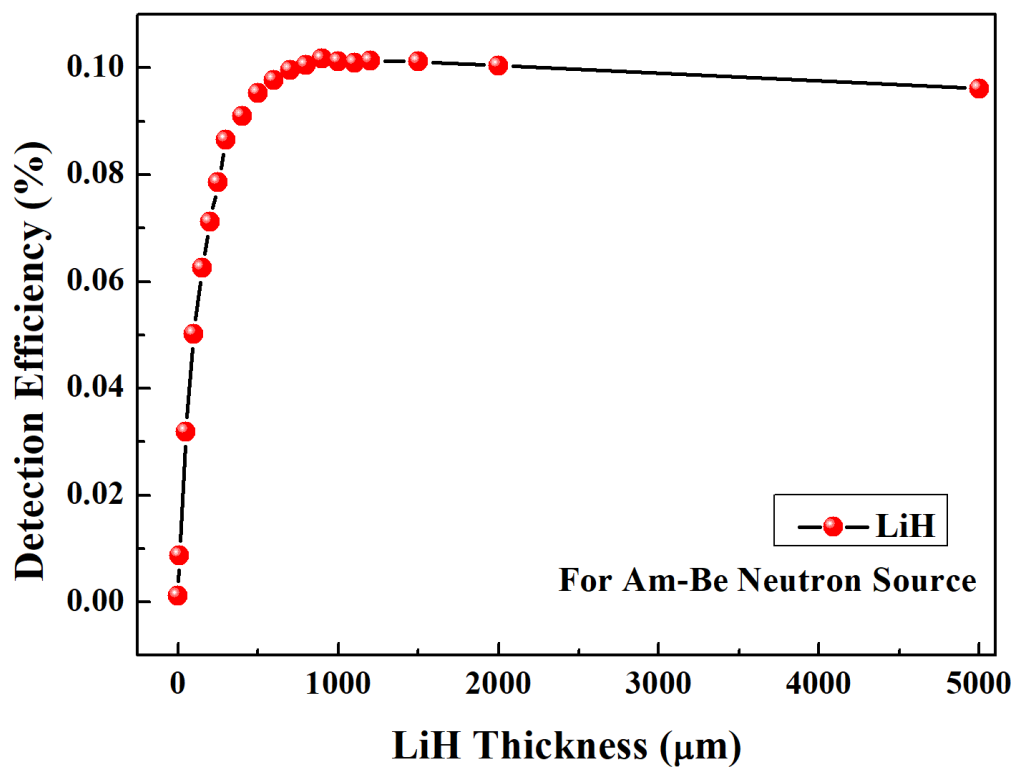


Figure 4.20 Efficiency vs. LiH thickness for  $^{241}\text{Am}$ -Be neutron source.

Table 4.7 shows the optimized thickness of LiH converter for different mono-energetic neutron beams along with the maximum detection efficiency achievable. The LiH thickness can be selected from Table 4.7 for a specific application where the incident neutron energy is known. For instance, a 150  $\mu\text{m}$  thick LiH can be selected for 2.5 MeV D–D neutron source. Similarly, for efficiently detecting the 14 MeV neutrons the LiH thickness of  $\sim 2$  mm will be appropriate. For  $^{241}\text{Am}$ -Be neutron source, the optimized thickness of LiH is  $\sim 500$ – $600$   $\mu\text{m}$ .

Furthermore, for the unknown spectrum, a LiH thickness can be chosen, which can be efficient for specific energy range, i.e., 0.5–10 MeV in the context of this work. Thus, to cover the unknown spectrum of energies ranging from 0.5–10 MeV,  $\sim 500$   $\mu\text{m}$  thick LiH can be accounted as an optimized thickness.

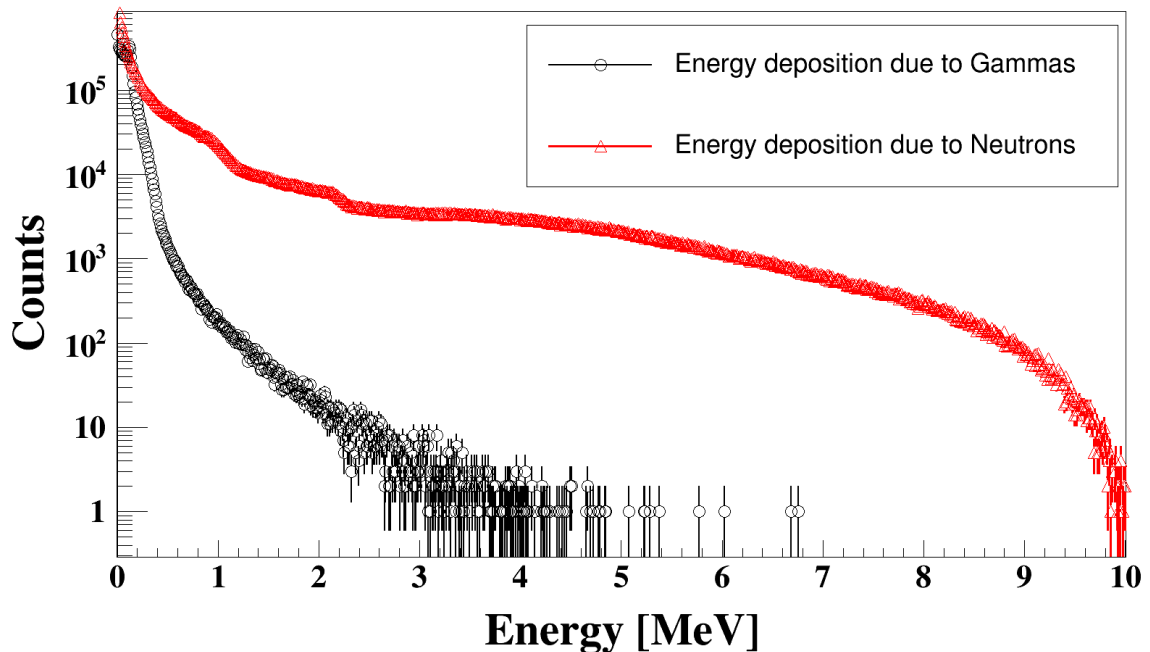
**Table 4.7 Optimized thickness and efficiency of the LiH-SiC detector for different energy neutrons.**

Energy (MeV)	Optimized thickness ( $\mu\text{m}$ )	Maximum Efficiency (%)
0.5	60	0.012
1	80	0.022
2	120	0.047
3	150	0.074
4	250	0.1
5	400	0.13
6	550	0.15
7	700	0.18
8	800	0.2
9	1100	0.23
10	1500	0.25
14	2000	0.32
Am-Be	500-600	0.105

#### 4.4.4.2 Effect of $\gamma$ -discrimination on efficiency

To analyze the effect of  $\gamma$ -background discrimination on neutron detection efficiency, a mixed neutron-gamma source is generated as defined in Section 4.2.2 (Figure 4.2).

Figure 4.21 shows the histogram of the total energy deposition in the SiC detector region due to the gamma and neutron induced events. It is evident that the spectrum due to gamma events, which have a mean energy  $\sim 150$  keV, are quite dominant and comparable to the neutron-induced events (counts) in the low energy region (below 1 MeV). Between 1 and 2 MeV, the difference in counts is quite evident and can easily be discriminated by implementing LLD, as described in Section 4.2.2. Beyond 2 MeV, counts due to gamma events are almost negligible. To prevent the spurious counts originated due to the background radiations, LLD is applied and its effect on neutron detection efficiency has been illustrated in Figure 4.22. It is observed that by increasing the LLD threshold to higher energy levels, the background radiations of  $\gamma$ -rays and other charged particles are eliminated. However, some vital counts due to recoil protons are also eliminated resulting in the reduction of detection efficiency. Therefore, the detector with a finite threshold level always offers marginally lower efficiency.



**Figure 4.21** Comparison of energy deposition (histograms) in the detector active region due to gamma ( $E_{\text{mean}} = \sim 150$  keV) and neutron ( $E_{\text{mean}} = \sim 3.5$  MeV) events.

As can be seen, at the LLD value of 300 keV, 500 keV, 1 MeV, and 2 MeV, the efficiency is reduced to  $\sim 0.097\%$ ,  $\sim 0.094\%$ ,  $\sim 0.087\%$ , and  $\sim 0.063\%$ , respectively, from the value of  $0.105\%$  which is obtained without LLD. In other words, the neutron detection efficiency would be reduced by  $\sim 7\%$ ,  $\sim 10\%$ ,  $\sim 16\%$ , and  $\sim 40\%$  with the applied LLD value of 300 keV, 500 keV, 1 MeV, and 2 MeV, respectively. This also shows a trade-off between neutron detection efficiency and  $\gamma$ -discrimination. For achieving high  $\gamma$ -discrimination, one has to accept the low efficiency or vice-versa.

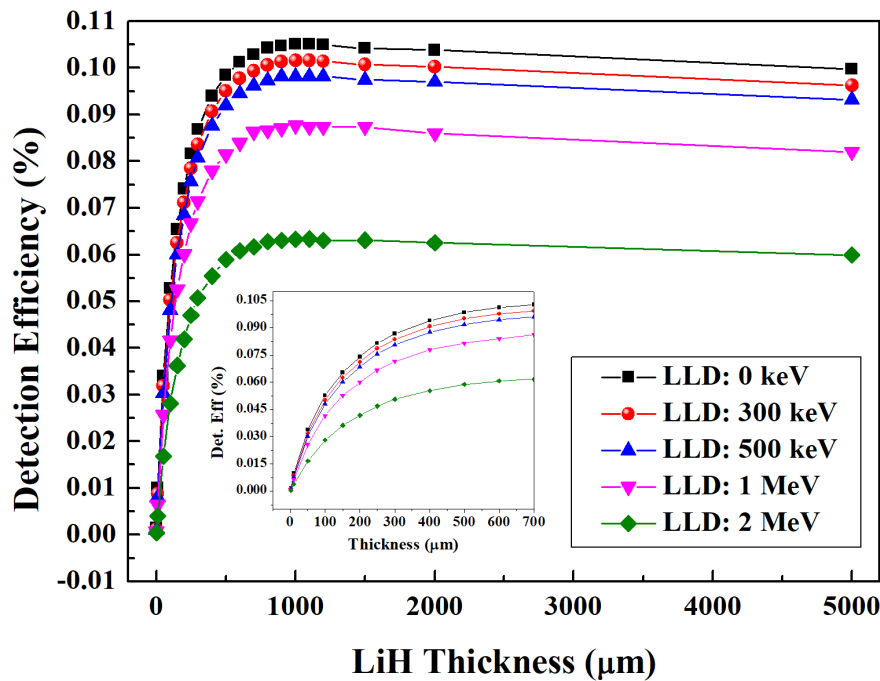


Figure 4.22 Effect of various LLD threshold values on the neutron detection efficiency of the LiH-SiC-based detector.

#### 4.4.4.3 LiH-SiC-based Stacked detector simulation for higher efficiency

Furthermore, to enhance the efficiency of the detector, stacked detector (Figure 4.3) simulations (as explained in section 4.2.3) have been carried out. The thickness of LiH and SiC are kept as  $500\ \mu\text{m}$  and  $600\ \mu\text{m}$ , respectively. The improvement in neutron detection efficiency is estimated by increasing the number of stacked layers and depicted in Figure 4.23. It is observed from Figure 4.23 (a) that the improvement in efficiency is not linear to

the increment in the number of stacks. As the number of stacks is increased from 1 to 2, the increment in efficiency is almost double, i.e., ~ 98% increment. Further, from second-stack to third-stack, the increment is reduced to 50%. Similarly, from ninth-stack to tenth-stack, the increase is just 10%. This implies that after a certain number of stacked layers the efficiency eventually gets saturated. This is because; each layer in the stack attenuates a part of impinging neutron flux, resulting in a diminished flux for the subsequent layers. Also, the probability of neutron interaction with converter material will saturate at a certain thickness as shown in Figure 4.4 for HDPE converter material.

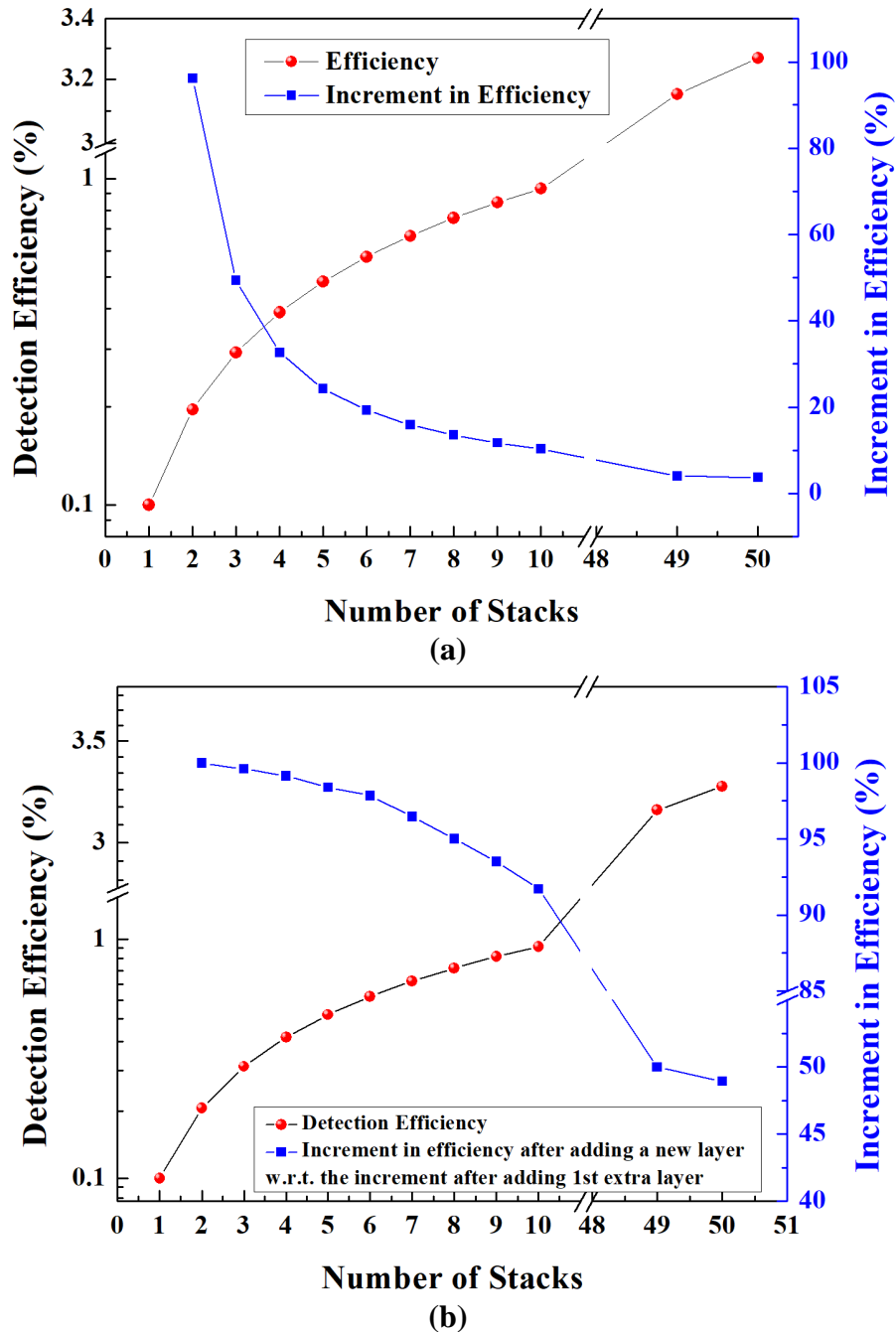
Figure 4.23 (b) illustrates the increment in the efficiency of LiH-SiC detector after adding a new layer with respect to the increment in efficiency obtained after adding the 1st extra layer, i.e., w.r.t. adding the 2<sup>nd</sup> layer. The efficiency of ~ 0.93% has been achieved with ten stacked layers of the LiH-SiC-stacked detector.

In order to further enhance the efficiency, stacked detectors of different stacked layers viz., 5, 10, 15, 20, and 50, have been simulated as a function of varying converter thicknesses and illustrated in Figure 4.24. It is apparent from the figure that the maximum neutron detection efficiency of ~ 3.25 % can be achieved with 50 stacked layers of LiH-SiC, having 450  $\mu\text{m}$  thick LiH converter layer.

#### **4.4.5 Comparison of Energy deposition in SiC through LiH & HDPE**

Figure 4.25 shows the histogram of total energy deposited in the active region of the SiC by secondary particles generated due to the neutron interaction in the HDPE and LiH converters. It can be observed that the energy deposited in SiC by the charged particles generated in LiH is slightly higher than the deposition by the charged particles generated in HDPE. This is due to the lower density of LiH than HDPE, which results in less energy deposition (or loss) by charged particles in LiH itself. In other words, charged particles are traversing the longer distance in LiH than HDPE converter material. The histogram of

energy deposition by the recoil-protons (generated in LiH and HDPE) in SiC is shown in Figure 4.26. This figure also confirms that a more significant number of recoil-protons are reaching in the active region of the SiC detector after going through LiH converter. Hence, LiH-SiC-based detector will produce a better detectable signal.



**Figure 4.23** Increment in the detection efficiency of LiH-SiC-based detector with various stacked layers.

(a) The percentage increment in efficiency upon increasing the number of layers. (b) The percentage increment in the efficiency after adding a new layer with respect to the increment in efficiency obtained after adding the 1<sup>st</sup> extra layer, i.e., w.r.t. adding the 2<sup>nd</sup> layer.

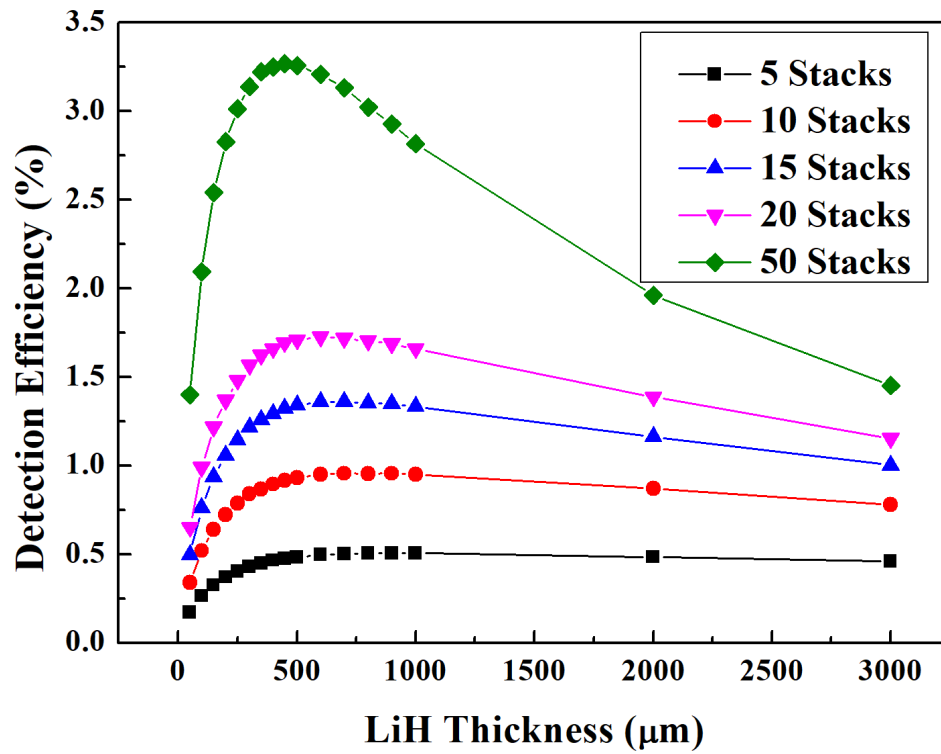


Figure 4.24 Efficiency variation with respect to converter thicknesses for a stacked detector with a different number of stacked layers viz., 5, 10, 15, 20 and 50.

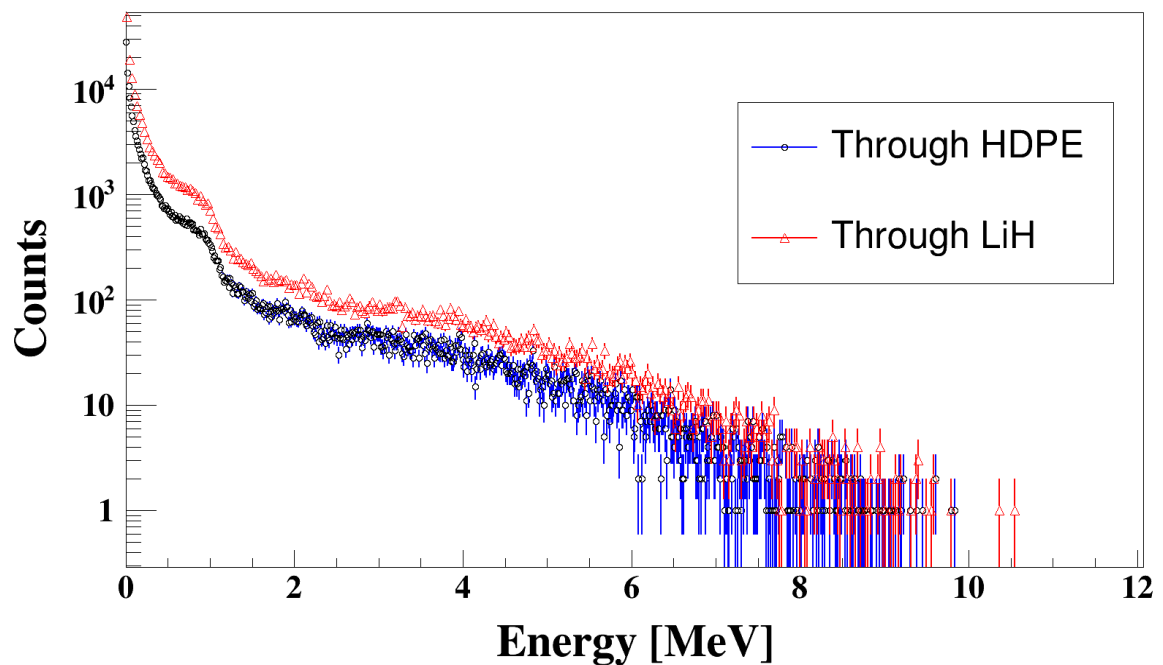
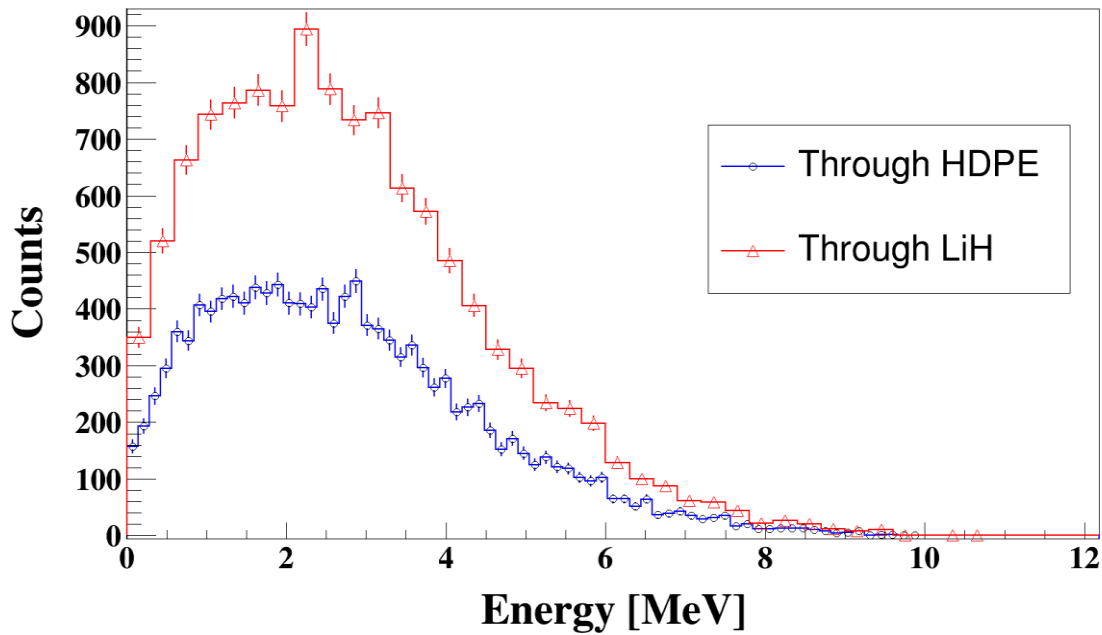


Figure 4.25 The histogram of the total energy deposited in the active region of SiC by the secondary charged particles generated due to the neutron interaction in the HDPE and LiH converters.



**Figure 4.26** The histogram of energy deposition by the recoil-protons (generated in LiH and HDPE) in SiC active region.

#### 4.4.6 Perylene as a converter (perylene–SiC-based detector)

It is known that a low- $Z$  hydrogenous material is preferred for use as a neutron converter since it possesses relatively high cross-section for elastic scattering with fast neutrons [6], [9]. Perylene is an organic semiconductor material having high hydrogen content which could be utilized as a medium of elastic scattering for fast neutrons to produce recoil protons such as in proton recoil detector. The recoil protons generated in the converter would lose part of its energy in converter itself which could not be collected, thus resulting in a continuum of energy spectrum in the active region of the SiC detector. Kargar *et al.*, have reported a direct conversion fast neutron detector made up of perylene [106]. Though the detector was able to respond to neutrons, but the neutron counts were very less. It could be because of the very low mobility of electrons and holes in perylene, i.e., 5.5 and 87.4  $\text{cm}^2/\text{V}\cdot\text{s}$  at 60 K, respectively. It could also hinder the efficient charge collection process, thereby providing no significant usage application. Therefore, we have proposed perylene to be used as a hydrogenous neutron converter material along with the SiC-based



detector for harsh environment applications. Since perylene is an organic semiconductor; it may also assist in the charge collection even from the unexploited energy which is lost in the converter. If it can be achieved, it would definitely augment the efficiency of the detector.

GEANT4 simulations have been performed to optimize the thickness of perylene for different mono-energetic as well as  $^{241}\text{Am}$ -Be neutron sources. Figure 4.27 represents an efficiency of perylene converter-based SiC detector as a function of perylene thickness for different energy neutrons. From this plot, the optimum thickness could be determined for different mono-energetic and unknown spectrum of neutrons having energies up to 10 MeV range. The data in Table 4.8 shows the optimized thickness of perylene converter for different mono-energetic neutron beams along with the maximum detection efficiency achievable. The perylene thickness can be selected from Table 4.8 as per the application requirement. For instance, a  $\sim 100\text{ }\mu\text{m}$  thick perylene can be chosen for a 2.5 MeV D-T neutron source. Furthermore, for the unknown spectrum, a perylene thickness can be selected, which can be efficient for specific energy range, i.e., 0.5–10 MeV in the context of this work. Thus, to cover the unknown spectrum of energies ranging from 0.5–10 MeV,  $\sim 500\text{ }\mu\text{m}$  thick perylene can be accounted as an optimized thickness.

The thickness of perylene is also optimized for  $^{241}\text{Am}$ -Be neutron source and is illustrated in Figure 4.28. The maximum efficiency of  $\sim 0.045\%$  is obtained at around  $500\text{ }\mu\text{m}$  thickness of perylene. The mean energy of  $^{241}\text{Am}$ -Be neutron source is  $\sim 4.16\text{ MeV}$ , and from Table 4.8, the optimized thickness of perylene for 4 MeV mono-energetic neutron source is  $\sim 450\text{ }\mu\text{m}$ , which is very close to our  $^{241}\text{Am}$ -Be simulation result of  $500\text{ }\mu\text{m}$ . It can be concluded from the study that the perylene can be used as a converter material with SiC for fast neutron detection but the efficiency obtained is quite low. Also, at present, it is

unclear, how the difference in charge collection efficiency (CCE) of perylene and SiC will affect the overall CCE of the detector, but it could be an area worth to explore further.

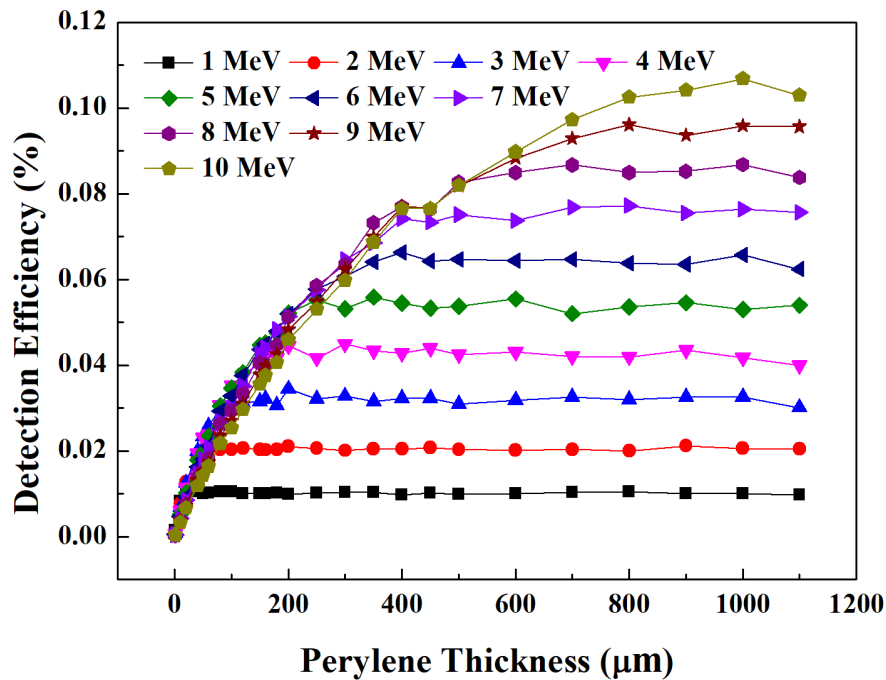


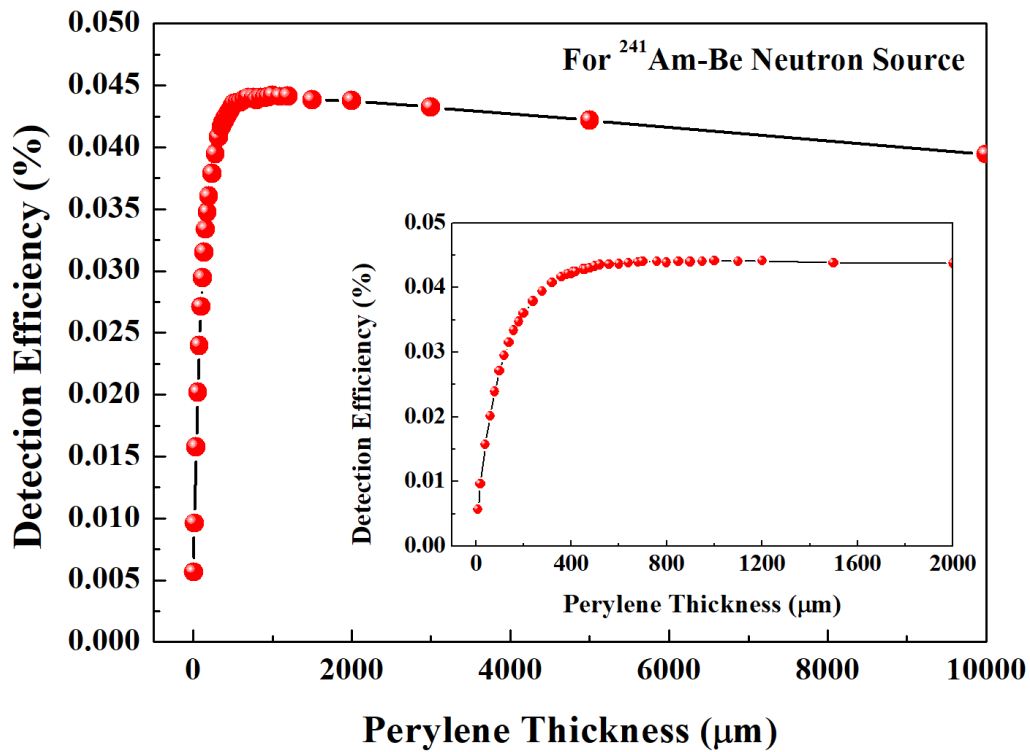
Figure 4.27 Efficiency vs. perylene thickness for various mono-energetic neutrons.

Table 4.8 Optimized thickness and efficiency of the perylene-SiC detector for different energy neutrons.

Neutron Energy (MeV)	Optimized thickness (μm)	Maximum Efficiency (%)
1	60	0.0104
2	140	0.0207
3	300	0.034
4	450	0.045
5	500	0.056
6	550	0.066
7	600	0.075
8	700	0.087
9	800	0.096
10	900	0.106

#### 4.4.7 Dependence of Efficiency on source distribution

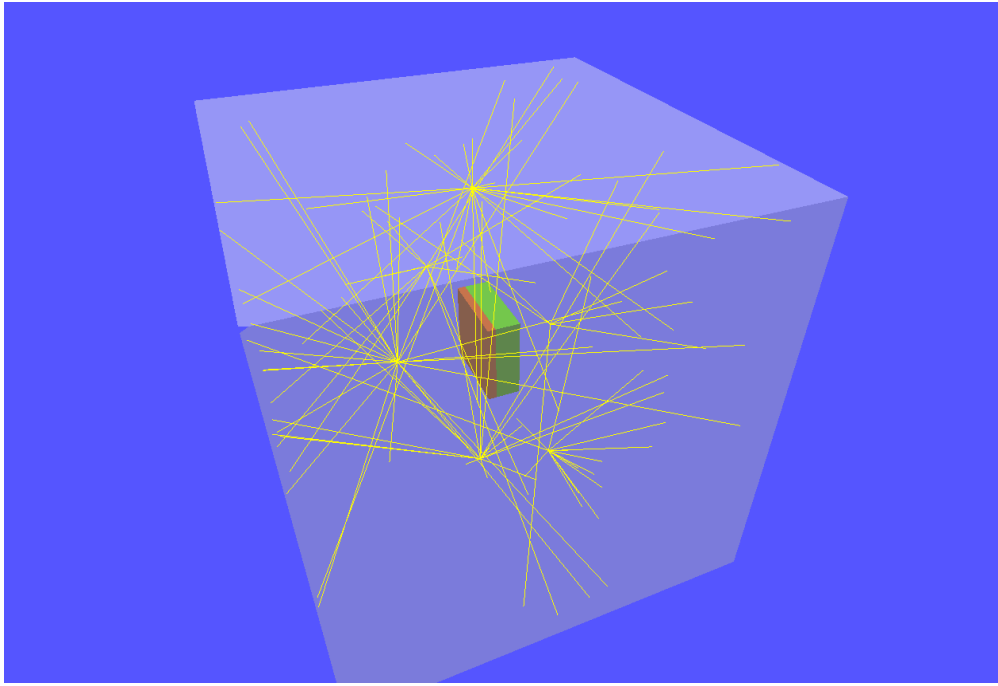
In our simulation, to achieve the maximum theoretical neutron detection efficiency, the source is defined in such a way that the incident neutrons are impinging uniformly and perpendicularly on the front face of the converter material– a standard approach suggested



**Figure 4.28 Perylene thickness optimization for  $^{241}\text{Am-Be}$  Neutron source.**  
(Inset: Zoomed view of 0–2000  $\mu\text{m}$  thickness region of perylene)

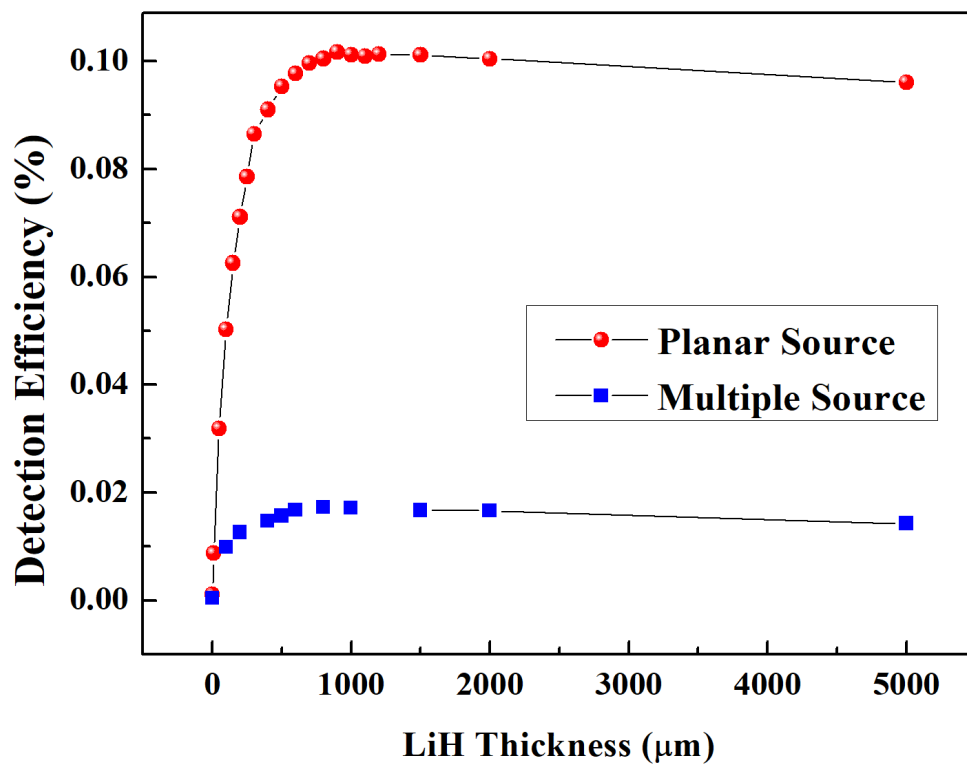
by McGregor *et al.*, [101]. However, in real-world applications, neutrons fall from random directions on the detector surface. For demonstrating such scenarios, simulations have been carried out with multiple isotropic sources positioned at six different locations with respect to the detector for creating the practical situation where radiation from random direction/angle are impinging on the detector (shown in Figure 4.29).

It can be observed from Figure 4.30, that the optimized thickness and the curve plateau trend are more or less similar; only the detection efficiency is reduced. The reduction in detection efficiency can be attributed to the fact that now lesser number of neutrons are falling on the converter surface. Therefore, lesser number of forward peaking elastic scattering reactions with hydrogen atoms are happening and resulting in lesser number of recoil-protons in SiC active region. Hence, in practical applications, the actual detection efficiency would always be lesser than the efficiency reported by this simulation study.



**Figure 4.29 GEANT4 simulation in Real World Scenario.**

Screenshot of the GEANT4 simulation in which six isotopic neutron sources are defined to create real-world radiation situation. Now the neutrons are impinging from 6 different directions on the detector surface randomly. (For demonstration, only 200 events are used in this image).



**Figure 4.30 Efficiency vs. LiH converter thickness of LiH-SiC-based FND for planar and multiple sources**

## 4.5 SUMMARY

GEANT4 Monte-Carlo simulation have been performed extensively for (a) optimizing the thicknesses of several neutron converter materials viz., HDPE, LiH and perylene, (b) for determining the effect of background discrimination on neutron detection efficiency and (c) for improving the efficiency of HDPE/LiH-SiC based detectors.

For locations such as under vessel where maximum temperature is  $< 90\text{ }^{\circ}\text{C}$  at full power, the HDPE-SiC-based detector is recommended. The maximum efficiency achieved is  $\sim 0.112\%$  with  $400\text{ }\mu\text{m}$  thick HDPE converter in planar configuration. The efficiency is enhanced up to  $\sim 1.04\%$  and  $\sim 3.85\%$  with 10 and 50 stacked layers, respectively.

Furthermore, for locations where temperature is  $\sim 200\text{-}250\text{ }^{\circ}\text{C}$ , LiH is proposed to be coated on SiC as a neutron converter. The maximum efficiency of  $\sim 0.1\%$  is achieved with  $500\text{ }\mu\text{m}$  thick LiH. The efficiency is enhanced up to  $\sim 0.93\%$  and  $3.25\%$  with 10 and 50 stacked layers, respectively.

A point worth to mention here is that in GEANT4 simulations, the effects of temperature and the dead layer are not considered. The regions inside and near the metal electrodes/protective coatings on the diode structure constitute the dead layer. The dead layer thickness decreases the efficiency of the detector by further reducing the initial kinetic energy available to the charged particles, which are formed due to neutron interactions in the converter [109]. Prasanna *et al.*, [110] have reported that due to a  $0.2\text{ }\mu\text{m}$  thick Au dead layer, the thermal neutron detection efficiency of the  $^{10}\text{B}$  coated Si detector is reduced to  $4\%$  from  $4.2\%$  ( $5\%$  reduction). The effect of dead layer in fast neutron detectors is expected to be less prominent in comparison to thermal neutron detectors.

At elevated temperatures, due to Doppler Effect, neutron interaction cross-section

also decreases which reduces the neutron detection efficiency further. Hence, the actual efficiency would be slightly lower than the simulated efficiency.

\*\*\*\*\*

# 5

## **EFFECT OF DEEP LEVELS ON THE CHARACTERISTICS OF SiC-BASED SBDs**

---

### **5.1 PREAMBLE**

This chapter presents the results of TCAD simulation studies performed for analyzing the effect of irradiation-induced deep-levels (defined in Section 2.5.2) on the electrical characteristics of 4H-SiC based SBD detectors.

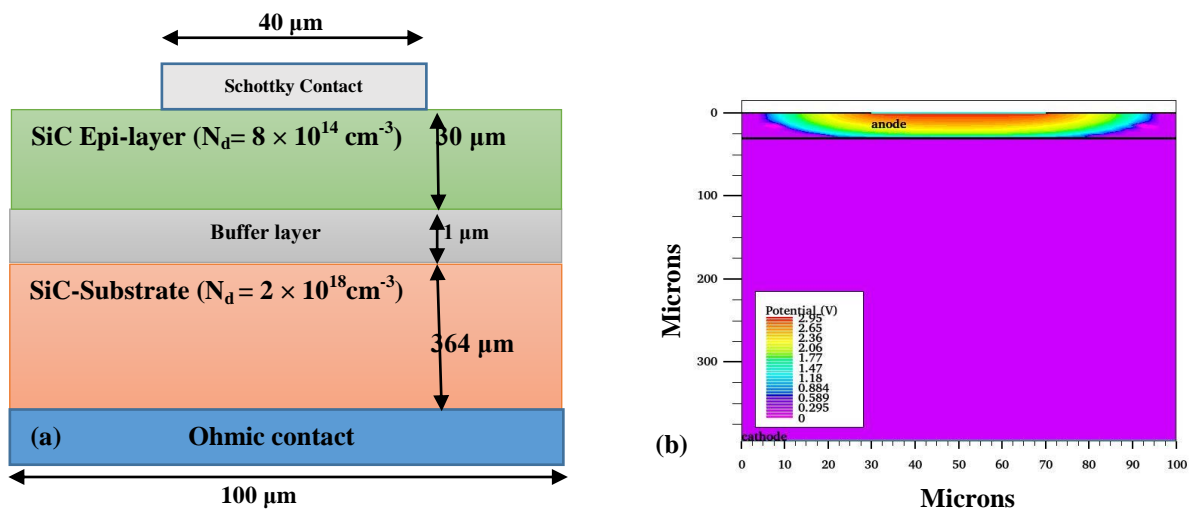
Section 5.2 briefly describes the SiC-based device description and steps of simulation in SILVACO™ TCAD. The parameter values associated with physical models required for modeling 4H-SiC based SBDs are also given.

Section 5.3 presents the device simulation results for *as-grown* (not-irradiated), 100 Mrad  $\gamma$ -irradiated (for reproducing the published results, i.e., benchmarking of our modeling), 8.2 MeV electron, 6.5 MeV proton and 1 MeV equivalent neutron irradiated *n*-type 4H-SiC SBD detectors.

At present, the TCAD study is focused on the bare SiC-based SBD detector, i.e., without converter layer. Furthermore, the TCAD simulations are based on the assumptions that at higher fluence new deep levels are not generated and even if they are generated their densities are too low to affect the device electrical performance. This study is performed to examine the maximum level of radiation fluence to which *n*-type 4H-SiC based SBD detectors can be exposed to.

## 5.2 DEVICE SIMULATION METHODOLOGY IN SILVACO TCAD

A 2D-structure of Ni/*n*-type 4H-SiC-based SBD is generated in the DEVEDIT module of the SILVACO TCAD. The created SBD structure is similar to the fabricated structure reported in the literature by P.V. Raja *et al.*, [58]. Figure 5.1, shows the typical dimensions of the 2D diode structure. The Ni/4H-SiC SBD bulk structure consists of three uniformly doped regions: (1) 30  $\mu\text{m}$  thick lightly doped ( $8 \times 10^{14} \text{ cm}^{-3}$ ) epitaxial layer for Schottky contact formation at the top surface, (2) 1  $\mu\text{m}$  thick buffer layer (doping:  $1 \times 10^{17} \text{ cm}^{-3}$ ) and (3) 364  $\mu\text{m}$  thick heavily doped ( $1 \times 10^{18} \text{ cm}^{-3}$ ) substrate for ohmic contact formation at the bottom. A 40  $\mu\text{m}$  wide Ni (50 nm)/Au (150 nm) bimetal Schottky contact has been defined on the top surface of the epitaxial layer. Very fine meshing is done near the contacts and junctions. The structure is then loaded into ATLAS, a device simulation module. The 4H-SiC material parameters are defined together with the essential models as defined in Chapter 3 (Section 3.4.3). The typical parameters and their values for *n*-type 4H-SiC device modeling in TCAD are extracted from the recent experimental results reported in the literature and are listed in Table 5.1.



**Figure 5.1 (a) Schematic of *n*-type 4H-SiC 2D-structure simulated in TCAD (b) 2D-structure generated in DEVEDIT module.**



**Table 5.1 TCAD model parameter values for the modeling of SiC-based devices.**

State ment	Parameters	Possible Range of Values	Value used in this work	Unit	References
<b>MATERIAL</b>	Affinity ( $\chi$ )	$3.6 \pm 0.2$	3.6	eV	[111]
	Permittivity ( $\epsilon$ )	9.66–9.76	9.66	–	[112]
	EG300 ( $E_g(300)$ )	3.23–3.285	3.23	eV	[97]
	EGALPHA ( $\alpha^{E_g}$ )	0.0033–0.033	0.033	eV/K	[97]
	EGBETA ( $\beta^{E_g}$ )	$240-1 \times 10^5$	$1 \times 10^5$	K	[97]
	TAUN0 ( $\tau_{n0}$ )	$1 \times 10^{-9}$	$1 \times 10^{-9}$	s	[96]
	TAUP0 ( $\tau_{p0}$ )	$6 \times 10^{-7}$	$6 \times 10^{-7}$	s	[96]
	TMUN ( $\mu_n^T$ )	1.72–2.25	1.72–2.25	–	[113]
	TMUP ( $\mu_p^T$ )	2.25	2.25	–	[113]
	LT.TAUN	2.3	2.3	–	[96]
	LT.TAUP	2.3	2.3	–	[96]
	AUGN ( $C_n$ )	$5 \times 10^{-31}$	$5 \times 10^{-31}$	cm <sup>6</sup> /s	[96]
	AUGP ( $C_p$ )	$2 \times 10^{-31}$	$2 \times 10^{-31}$	cm <sup>6</sup> /s	[96]
<b>MOBILITY</b>	MU1N.CAUG ( $\mu_n^{min}$ )	10–28	28	cm <sup>2</sup> /(V-s)	[97]
	MU2N.CAUG ( $\mu_n^{T_0}$ )	410–950	950	cm <sup>2</sup> /(V-s)	[97]
	ALHPAN.CAUG ( $\alpha_n^{mob}$ )	–3–0	0	–	[97], [114]
	BETAN.CAUG ( $\beta_n^{mob}$ )	–3–0.2	–2.4	–	[97], [114]
	GAMMAN.CAUG ( $\gamma_n^{mob}$ )	–7–0	0.73	–	[97], [114]
	DELTAN.CAUG ( $\delta_n^{mob}$ )	0.6–0.7	0.61	–	[97], [114]
	NCRITN.CAUG ( $N_{n0}^{crit}$ )	$(1-1.94) \times 10^{17}$	$1.94 \times 10^{17}$	cm <sup>-3</sup>	[97], [114]
	MU1P.CAUG ( $\mu_p^{min}$ )	0–20	0	cm <sup>2</sup> /(V-s)	[97], [114]
	MU2P.CAUG ( $\mu_p^{T_0}$ )	95–114	114	cm <sup>2</sup> /(V-s)	[97], [114]
	ALPHAP.CAUG ( $\alpha_p^{mob}$ )	–3–0	0	–	[97], [114]
	BETAP.CAUG ( $\beta_p^{mob}$ )	–3–0.2	–2.72	–	[97], [114]
	GAMMAP.CAUG ( $\gamma_p^{mob}$ )	0– 5.5	2.44	–	[97], [114]
	DELTAP.CAUG ( $\delta_p^{mob}$ )	0.5– 0.7	0.7	–	[97], [114]
	NCRITP.CAUG ( $N_{p0}^{crit}$ )	$1 \times 10^{16}-1 \times 10^{18}$	$1 \times 10^{16}$	cm <sup>-3</sup>	[97], [114]
	VSATN ( $v_{sat}$ )	$2.2 \times 10^7$	$2.2 \times 10^7$	cm/s	[96]
	D.CONWELL ( $D$ )	$6.9 \times 10^{20}$	$6.9 \times 10^{20}$	(cm.V.s) <sup>-1</sup>	[115]
	F.CONWELL ( $F$ )	$7.452 \times 10^{13}$	$7.452 \times 10^{13}$	cm <sup>-2</sup>	[115]
<b>IMPACT</b>	AN1 ( $a_n$ )	$3.44 \times 10^6$	$3.44 \times 10^6$	cm <sup>-1</sup>	[96]
	BN1 ( $b_n$ )	$2.58 \times 10^7$	$2.58 \times 10^7$	V/cm	[96]
	AP1 ( $a_p$ )	$(3.5-5.8) \times 10^6$	$3.5 \times 10^6$	cm <sup>-1</sup>	[96], [116]
	BP1 ( $b_p$ )	$(1.4-1.7) \times 10^7$	$1.7 \times 10^6$	V/cm	[96], [116]

After defining the material and models related parameter, the numerical method and biasing condition (AC or DC, as applicable) for each of the electrodes are applied. ATLAS then calculates the current through each electrode. ATLAS also calculates internal quantities, such as carrier concentrations and electric fields throughout the device, which is

difficult or impossible to measure. The terminal characteristics calculated by ATLAS are saved in Log files. These are current and voltages for each electrode in DC simulations. In transient simulations, the time is stored. In AC simulations, the small signal frequency and the conductances and capacitances are saved. The Log Files are visualized through the *tonyplot* module. From *tonyplot*, the data is exported in .csv format. Using these data, the device parameters such as ideality factor, barrier height, etc., as defined in Sections 2.4.4 and 2.4.5, are calculated.

In this work, trap signatures, as identified in the literature, have been added using TRAP statement to investigate the effect of irradiation on the electrical properties of the SiC-based SBD detector. Two dominant deep levels  $Z_{1/2}$  ( $E_c - 0.63 \text{ eV}$ ) and  $EH_{6/7}$  ( $E_c - 1.55 \text{ eV}$ ) are commonly identified in *as-grown* epitaxial layer of SiC by CVD technique [29]. Therefore, we have incorporated these two electron trap centers in the pre-irradiation or as-grown device model. The trap signatures identified after the gamma-irradiation (dose = 100 Mrad) by P.V. Raja *et al.*[59], is subsequently introduced in the  $\gamma$ -irradiation effect model. The purpose of the  $\gamma$ -irradiation study is to validate our simulation results with the room temperature experimental and simulation work reported in the literature.

Furthermore, dominant traps induced due to 8.2 MeV High Energy Electron (HEE), 6.5 MeV proton and 1 MeV equivalent neutron irradiations are incorporated in the electron, proton and neutron-irradiated models, respectively. The 1 MeV equivalent neutron fluence is the fluence of 1 MeV neutrons producing the same damage in a detector material as induced by arbitrary particle fluence with a specific energy distribution (NIEL Scaling). The defect concentration ( $N_T$ ) is directly proportional to the incident fluence (equation (3.9)). Therefore, the  $N_T$  increases with the incident neutron fluence. The concentration of a particular deep level at higher fluence is calculated using the defect introduction rate ( $N_T/\Phi_F$ ) as defined in references [87], [117]. The *I-V* and *C-V* simulations of neutron-

irradiated Ni/4H-SiC SBD detector have been performed at room temperature (RT), and the effect on the critical device parameters is evaluated. The simulation results are based on the assumptions that at higher fluence new traps are not created or their densities are too low to affect the device characteristics.

### 5.3 SIMULATION RESULTS & DISCUSSIONS

#### 5.3.1 Characteristics of as-grown (not-irradiated) Ni/4H-SiC SBD detector

The properties of ‘traps’ introduced in the as-grown model are tabulated in Table 5.2. The simulated temperature dependent forward  $J$ - $V$ -characteristics is shown in Figure 5.2. It is observed that the forward current density ( $J_F$ ) (for elevated temperature simulations) is decreasing at higher bias voltages. The reduction in the  $J_F$  with temperature can be attributed to the increasing series resistance ( $R_S$ ) of the SBD diode with temperature. The diminishing linear region of  $\ln(J)$ - $V$  plot (inset Figure 5.2) is also consistent with the increase in the  $R_S$  [118]. The forward characteristics of the SiC-SBD are in good agreement with the result reported in the literature [57], [73], [119].

**Table 5.2 Trap signatures introduced in as-grown Ni/4H-SiC SBD detector model [59].**

<b>E.LEVEL (<math>E_c-E_t</math>) (eV)</b>	<b>DENSITY (<math>N_T</math>) (<math>\text{cm}^{-3}</math>)</b>	<b>SIGN (<math>\sigma_n</math>) (<math>\text{cm}^2</math>)</b>	<b>Possible defects</b>
0.63	$1 \times 10^{13}$	$5 \times 10^{-16}$	$Z_{1/2}$
1.55	$1.5 \times 10^{13}$	$2 \times 10^{-18}$	$\text{EH}_{6/7}$
E.LEVEL, DENSITY, SIGN, are the Silvaco parameters of TRAP statement for trap energy location in band-gap, the density of traps and electron capture cross-section, respectively.			

Figure 5.3 shows the reverse characteristics at different temperatures (300–523 K). It is observed that the reverse leakage current density ( $J_R$ ) has increased many folds at a higher temperature. This high  $J_R$  will undoubtedly limit the application of SiC-based SBD at elevated temperatures. Therefore, specific techniques must be employed such as guard rings (GR), junction termination extension (JTE), mesa structure, etc., for reducing the reverse current [120], [121].

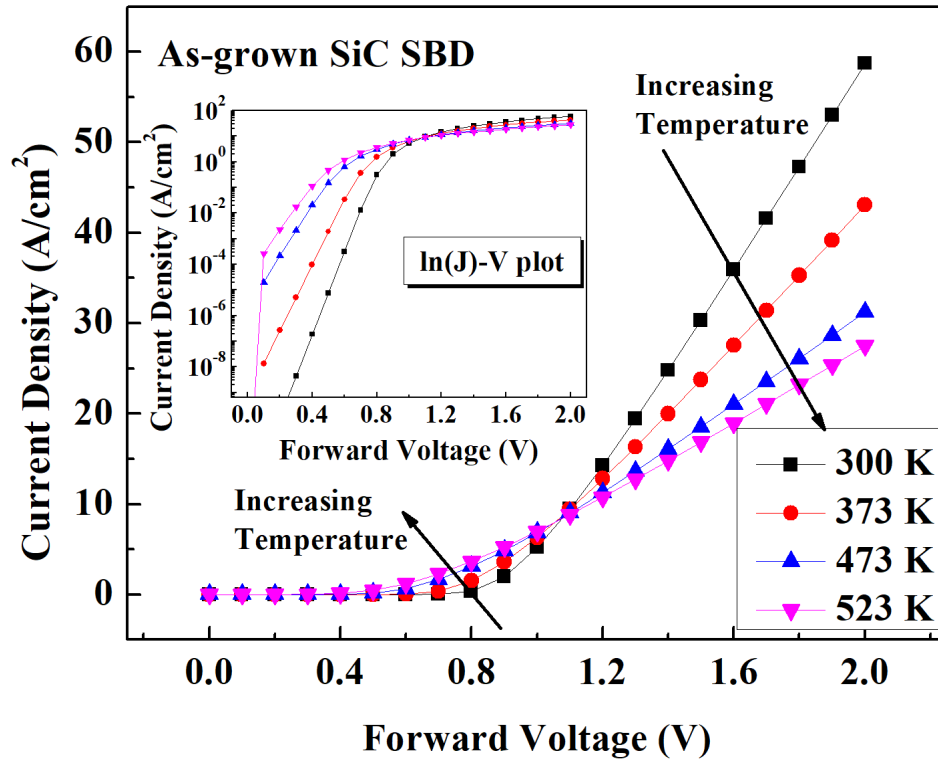


Figure 5.2 Simulated forward  $J$ - $V$ - $T$ -characteristics of as-grown Ni/4H-SiC-based SBD. (Inset: forward  $\ln(J)$ - $V$ - $T$  curve).

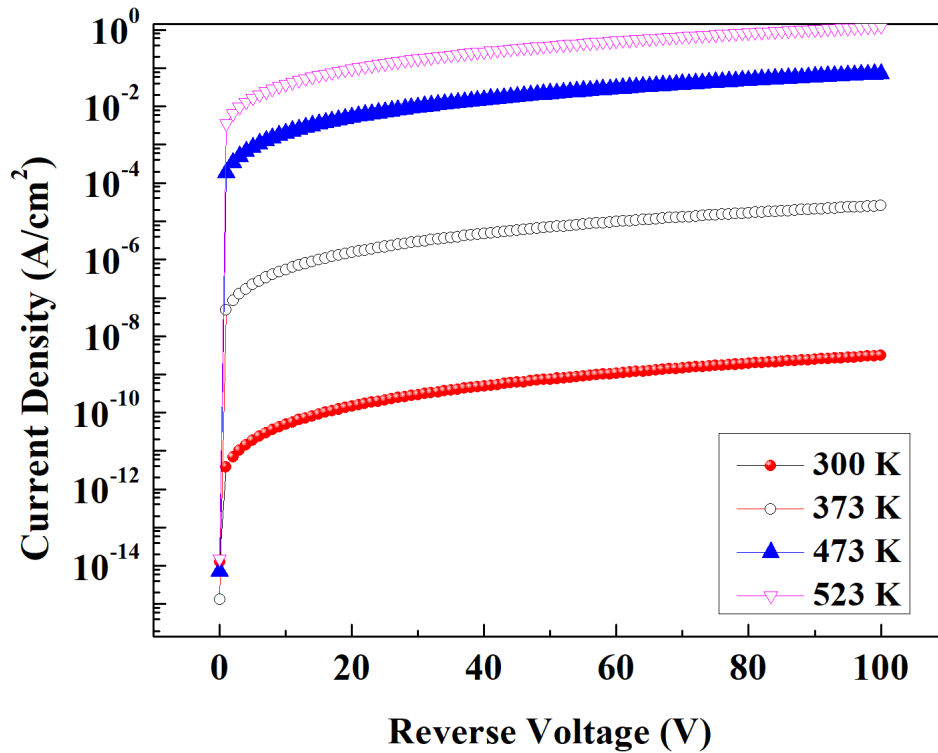


Figure 5.3 Simulated reverse  $J$ - $V$ - $T$ -characteristics of as-grown Ni/4H-SiC-based SBD.

The  $C$ - $V$ -characteristics is plotted as  $(1/C^2)$ - $V$  curve (not shown) and the effective doping concentration ( $\sim 7.8 \times 10^{14} \text{ cm}^{-3}$ ) is estimated using equation (2.16). The other device parameters such as:  $\phi_B$ ,  $\eta$ ,  $V_{bi}$ , etc., are also calculated and summarized in Table 5.7. It is found that the  $\phi_{B_{CV}}$  decreases with temperature (from 1.28 eV to 1.18 eV), because, as the temperature increases, the conduction band moves downwards, relative to the Fermi-level [73]. The discrepancy observed in the values of  $\phi_B$  obtained from the  $I$ - $V$  and  $C$ - $V$  measurements is also reported in the literature and is attributed to the barrier inhomogeneities\* present at metal and SiC interface [74].

### 5.3.2 Characteristics of Gamma-irradiated (dose=100 Mrad) Ni/4H-SiC SBD detector

A three-level defect model as described by P.V. Raja *et al.*, [59] is applied for simulating the  $\gamma$ -irradiated Ni/4H-SiC SBD detector. The properties of  $\gamma$ -ray (dose = 100 Mrad) induced trap levels is tabulated in Table 5.3. The simulated reverse  $J$ - $V$ -characteristics before and after the  $\gamma$ -irradiation of Ni/4H-SiC-based SBD detector at RT is shown in Figure 5.4. It is found that  $J_R$  has decreased after the  $\gamma$ -irradiation. This behavior is in contrary to the irradiation effects reported for the Si-based detectors [12], [122], but it is in good agreement with the experimental and simulation results reported in the literature for SiC-based devices [53], [59], [123]–[125]. This quality evinces the radiation hardness of SiC material. The leakage current density at  $-100 \text{ V}$  bias for non-irradiated and  $\gamma$ -irradiated SBD in the work of P.V. Raja *et al.*, [59] is  $\sim 3.3 \text{ nA/cm}^2$  and  $\sim 2 \text{ nA/cm}^2$ , respectively, whereas in our simulation it is  $\sim 3.1 \text{ nA/cm}^2$  and  $\sim 1.98 \text{ nA/cm}^2$  for non-irradiated and  $\gamma$ -irradiated SBD, respectively. The reduction in  $J_R$  after the  $\gamma$ -irradiation can be attributed to the considerable decrease in the electric field at the Ni-Schottky contact and the SiC interface (see Figure 5.5) [59].

---

\* Structural defects, chemical contaminations, dangling bonds at the semiconductor surface, as well as metal-induced gap states, and damages caused by metal deposition process can form interface states, which could result in non-ideal electrical behaviors.

**Table 5.3 Trap signatures introduced in gamma-irradiated (dose = 100 Mrad) Ni/4H-SiC SBD detector model [59].**

<b>E.LEVEL (<math>E_c-E_t</math>) (eV)</b>	<b>DENSITY (<math>N_T</math>) (cm<sup>-3</sup>)</b>	<b>SIGN (<math>\sigma_n</math>) (cm<sup>2</sup>)</b>	<b>Possible defects</b>
0.63	$2 \times 10^{14}$	$5 \times 10^{-16}$	Z <sub>1/2</sub>
1.55	$1.8 \times 10^{14}$	$2 \times 10^{-18}$	EH <sub>6/7</sub>
0.89	$0.4 \times 10^{14}$	$4 \times 10^{-18}$	RD <sub>1/2</sub>
E.LEVEL, DENSITY, SIGN, are the Silvaco parameters of TRAP statement for trap energy location in band-gap, the density of traps and electron capture cross-section, respectively.			

The forward  $J$ - $V$ -characteristics is shown in Figure 5.6. It is evident from the figure that the current density has been reduced after the  $\gamma$ -irradiation. It is due to the increase in  $R_S$  (from 55  $\Omega$  to 229  $\Omega$ ) of SBD after the irradiation (linear region of the forward  $\ln(J)$ - $V$  curve becomes smaller). The decreasing forward current density is consistent with the irradiation-induced increase in  $R_S$  [57], [117].

The  $(I/C^2)$ - $V$  plot (Figure 5.7) of Ni/4H-SiC SBD detector reveals that the effective doping concentration ( $N_{eff}$ ) has reduced to  $\sim 4.84 \times 10^{14} \text{ cm}^{-3}$  from the as-grown value of  $7.8 \times 10^{14} \text{ cm}^{-3}$ . After the creation of acceptor type deep levels in  $n$ -type SiC, the electrons are transferred from the conduction band to the deep levels resulting in compensation of donor doping concentration by the acceptor type defects [87]. The carrier removal rate due to  $\gamma$ -irradiation is estimated to be  $\sim 1.5 \times 10^{-3} \text{ cm}^{-1}$ . The decreasing  $N_{eff}$  in the  $\gamma$ -irradiated SBD is also causing the reduction in the electric field ( $E_{field}$ ) at the Ni/4H-SiC interface (Figure 5.5) since the  $E_{field}$  is directly proportional to the square-root of  $N_{eff}$  [59]. The SBD device parameters before and after the  $\gamma$ -irradiation are calculated from the  $J$ - $V$  and  $C$ - $V$  simulations and are listed in Table 5.7. The barrier-height has increased to the value of 2.03 eV from the pre-irradiation value of 1.28 eV. The ideality factor has deteriorated, whereas  $V_{bi}$ ,  $E_f$ ,  $\Delta\phi_{bl}$  etc., have increased following the  $\gamma$ -irradiation.

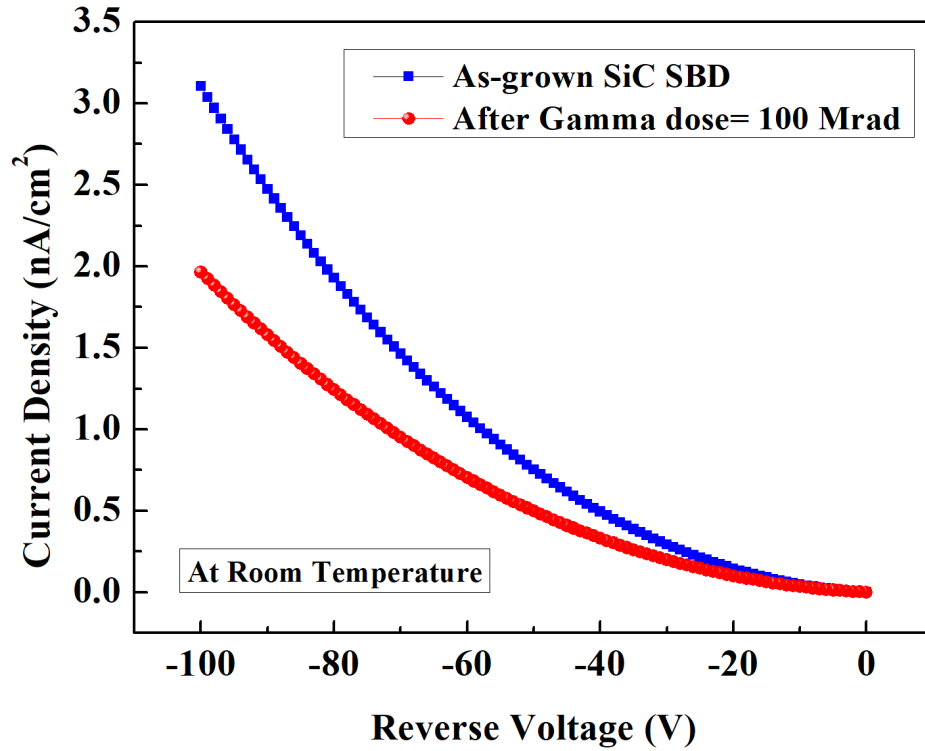


Figure 5.4 Reverse  $J$ - $V$ -characteristics of Ni/4H-SiC-based SBD prior to and after the gamma irradiation of dose equivalent to 100 Mrad.

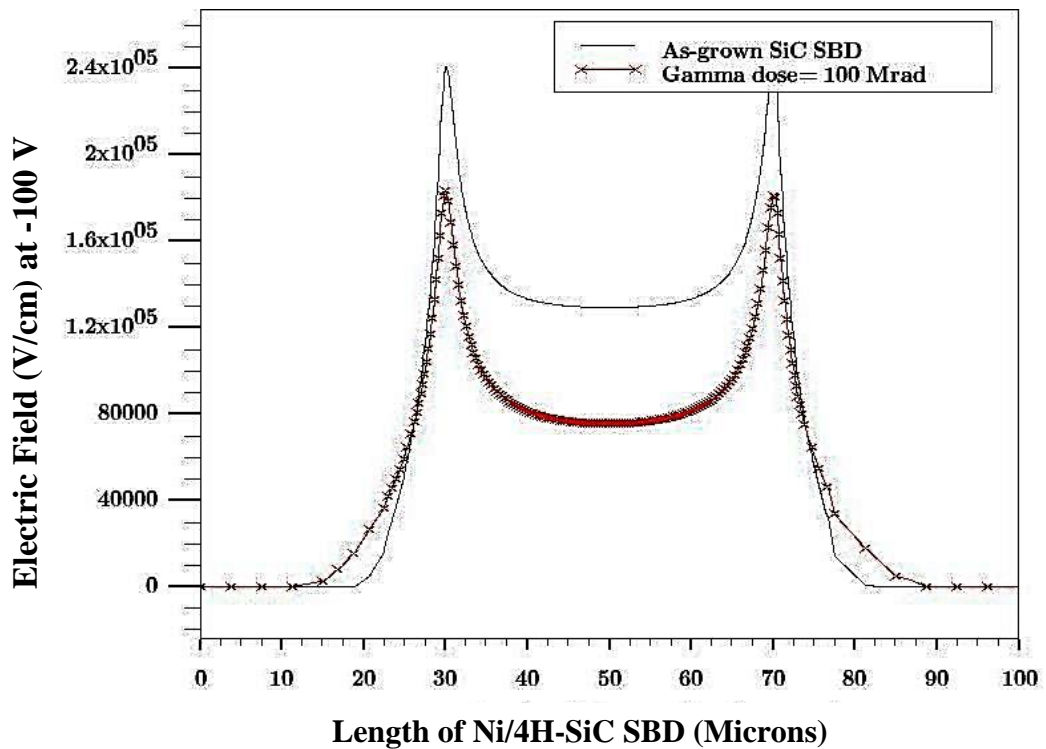


Figure 5.5 Electric field strength at the Ni-Schottky contact and SiC interface of the SBD prior to and after the  $\gamma$ -irradiation (dose = 100 Mrad), obtained from the outline of Electric-Field contour from the simulated structure.

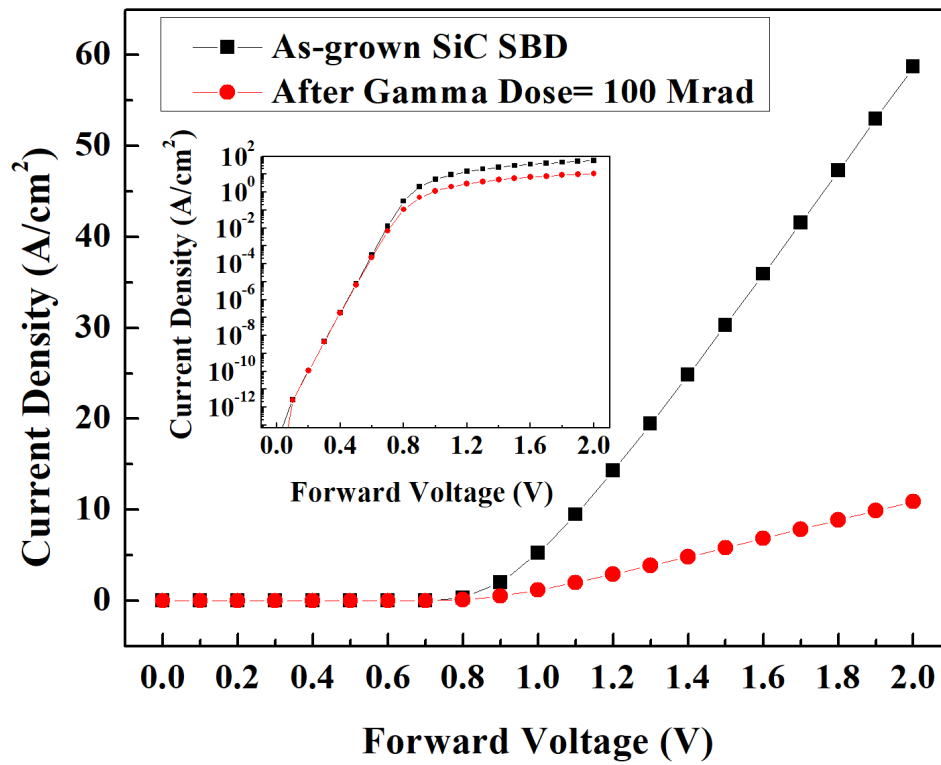


Figure 5.6 Simulated forward  $J$ - $V$ -characteristics of Ni/4H-SiC-based SBD prior to and after the  $\gamma$ -irradiation (dose=100 Mrad). (Inset: Reverse  $\ln(J)$ - $V$  plot).

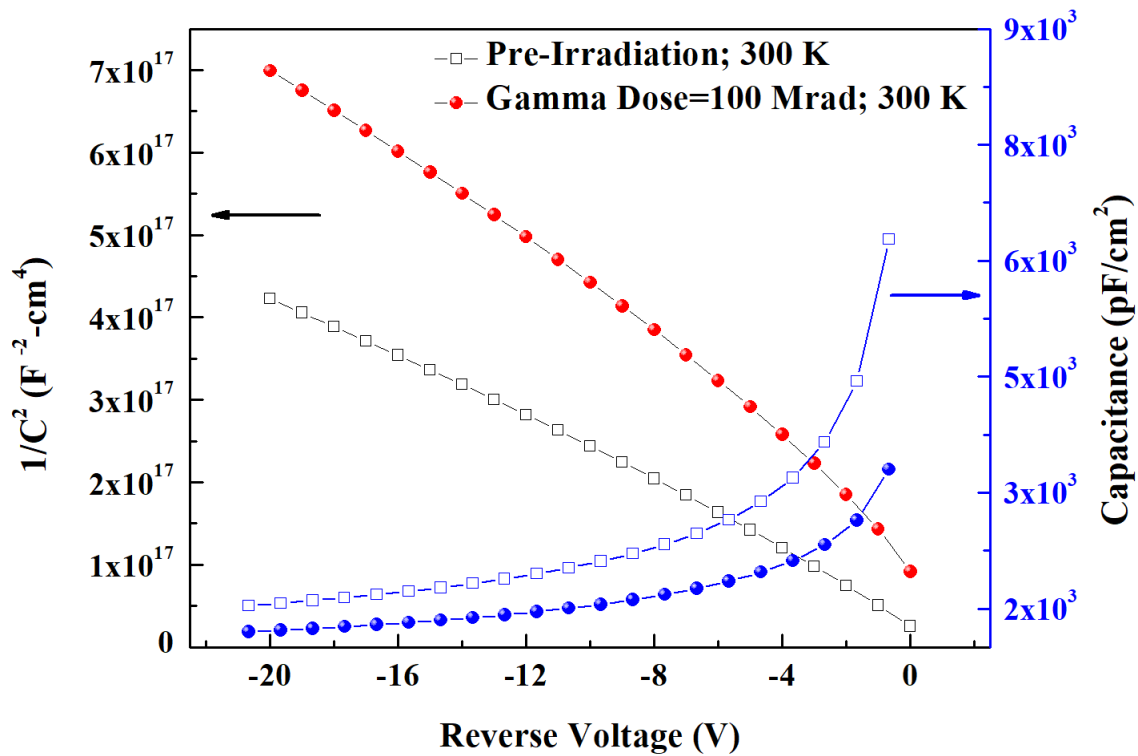


Figure 5.7 Simulated  $(1/C^2)$ - $V$  and  $C$ - $V$ -characteristics of Ni/4H-SiC SBD prior to and after the  $\gamma$ -irradiation.



### 5.3.3 Characteristics of 8.2 MeV Electron-irradiated Ni/4H-SiC SBD detector

The deep-level signatures as identified by Castaldini *et al.*, [55] after the 8.2 MeV High Energy Electron (HEE)-irradiation (fluence =  $9.5 \times 10^{14} \text{ cm}^{-2}$ ) are introduced in the electron-irradiation effect model. The attributes of the electron-irradiated deep-levels are tabulated in Table 5.4. The density of each deep-level at higher fluence is estimated according to the introduction rate of each trap, and the effect on the device characteristics is predicted. The simulated forward  $J$ - $V$ -characteristics before and after the electron-irradiation of Ni/4H-SiC-based SBD detector at RT is shown in Figure 5.8. It can be observed from the figure that the forward current density has been reduced following the electron-irradiation. It is due to the increase in  $R_S$  (from  $55 \Omega$  to the order of  $M\Omega$ s) of SBD after the irradiation. This may be due to the introduction of acceptor type deep-levels at various positions in the band-gap, which is causing trapping of free charge carriers and eventually increasing the resistance of the bulk. The decrease in the linear region of the forward  $\ln(J)$ - $V$  curve reflects the increase in  $R_S$ . The reduction in the  $J_F$  was also evident in the  $\gamma$ -irradiated SiC-based devices simulated in the previous section. The device parameters such as  $\eta$ ,  $\phi_B$ , and  $R_S$  are estimated from the forward  $J$ - $V$  and are tabulated in Table 5.7.

**Table 5.4 Properties of traps introduced in 8.2 MeV electron-irradiated SiC-based SBD (Fluence =  $9.5 \times 10^{14} \text{ electrons/cm}^2$ ) [55].**

E.LEVEL ( $E_c - E_t$ ) (eV)	DENSITY ( $N_T$ ) ( $\text{cm}^{-3}$ )	SIGN ( $\sigma_n$ ) ( $\text{cm}^2$ )	Introduction rate $\eta_r = N_T/\Phi_F$ ( $\text{cm}^{-1}$ )
0.15	$1.4 \times 10^{13}$	$6 \times 10^{-16}$	$\sim 0$
0.23	$5.5 \times 10^{13}$	$9 \times 10^{-16}$	0.06
0.33	$6.9 \times 10^{14}$	$7 \times 10^{-16}$	0.73
0.39	$4.0 \times 10^{14}$	$2 \times 10^{-15}$	0.42
0.65	$4.2 \times 10^{14}$	$1 \times 10^{-16}$	0.44
0.75	$2.6 \times 10^{14}$	$6 \times 10^{-15}$	0.27
0.89	$4.6 \times 10^{13}$	$7 \times 10^{-15}$	0.09

E.LEVEL, DENSITY, SIGN, are the Silvaco parameters of TRAP statement for trap energy location in band-gap, the density of traps and electron capture cross-section, respectively. The  $\sim 0$  introduction rate means that  $N_T$  is constant at higher fluence.

Figure 5.9 shows the reverse  $J$ - $V$ -characteristics of SiC-based SBD before and after the irradiation of electrons. The reverse characteristics revealed that the leakage current ( $J_R$ ) is decreasing after the irradiation. The results are consistent with the previous simulation results. The reduction in  $J_R$  is due to the considerable decrease in the electric field along the Schottky contact interface with SiC [59]. The electric field at the Schottky contact interface is directly proportional to the square root of the effective doping concentration ( $N_{eff}$ ).

In order to determine the effect of irradiation on the  $N_{eff}$ , the  $C$ - $V$ -simulations are performed. Figure 5.10 shows the simulated  $C$ - $V$ -characteristics of the SiC-based SBD before and after the energetic electron irradiation. The  $N_{eff}$  value, calculated from the  $(1/C)^2$ - $V$  plot for the electron irradiated SBD (Figure 5.10), has decreased to the value of  $\sim 7.06 \times 10^{14} \text{ cm}^{-3}$  from the pre-irradiation value of  $7.8 \times 10^{14} \text{ cm}^{-3}$  after the electron irradiation of fluence equivalent to  $9.5 \times 10^{14} \text{ electrons/cm}^2$ . The change in  $N_{eff}$  is due to the compensation of donors by the irradiation-induced acceptor-type deep-levels in SiC band-gap. The flat  $C$ - $V$ -characteristics after the fluence of  $10^{16} \text{ electrons/cm}^2$  reveals that the donor density in the SiC-SBD epitaxial layer is completely compensated and therefore, the  $n$ -type SiC has become an intrinsic semiconductor. The reduction in the doping concentration also caused the electric field to reduce at Ni and the SiC interface, which is the reason for the decrease in the reverse current at higher irradiation fluence of the electron. The carrier removal rate due to the electron irradiation in 4H-SiC is estimated as:  $0.74 \text{ cm}^{-1}$ . It is in good agreement with the value reported in the literature ( $1.67 \text{ cm}^{-1}$  for electron irradiated 4H-SiC [126]) and also lower than the value for Si-based devices [87]. The device parameters calculated from the electrical characteristics after the irradiation are tabulated in Table 5.7. Since the simulated  $C$ - $V$  response was flat after the radiation fluence greater than  $1 \times 10^{16} \text{ electrons/cm}^2$ ; the device parameters could not be estimated. Also, the ideality factor of the 4H-SiC SBD becomes too large to offer any reliable estimation.

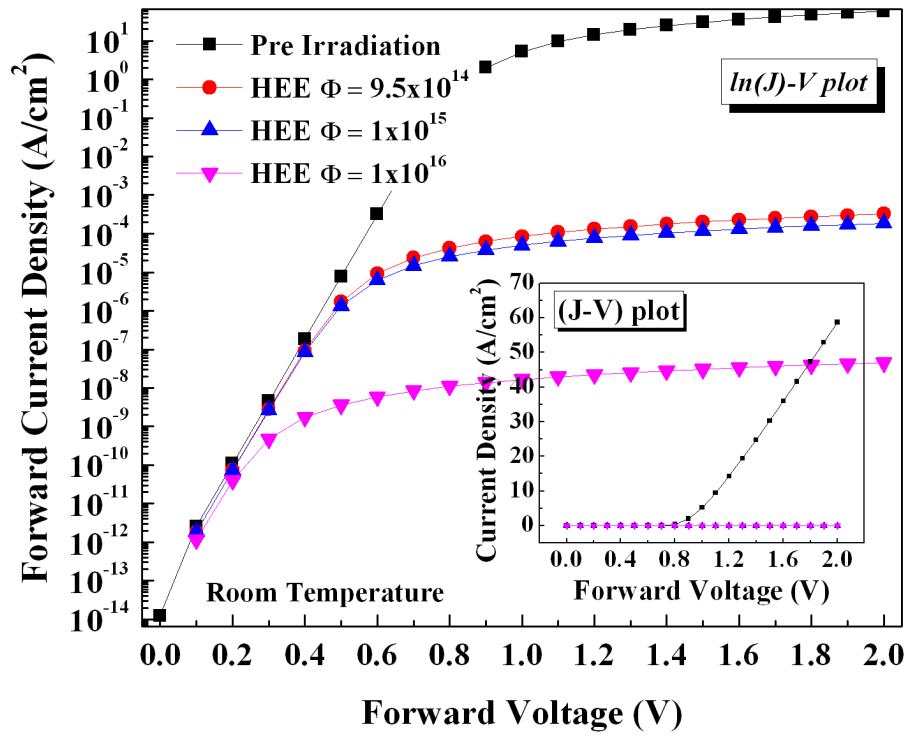


Figure 5.8 Forward characteristics ( $\ln J-V$  plot) of Ni/4H-SiC SBD before and after the 8.2 MeV high energy electron (HEE) irradiations at various fluence levels.

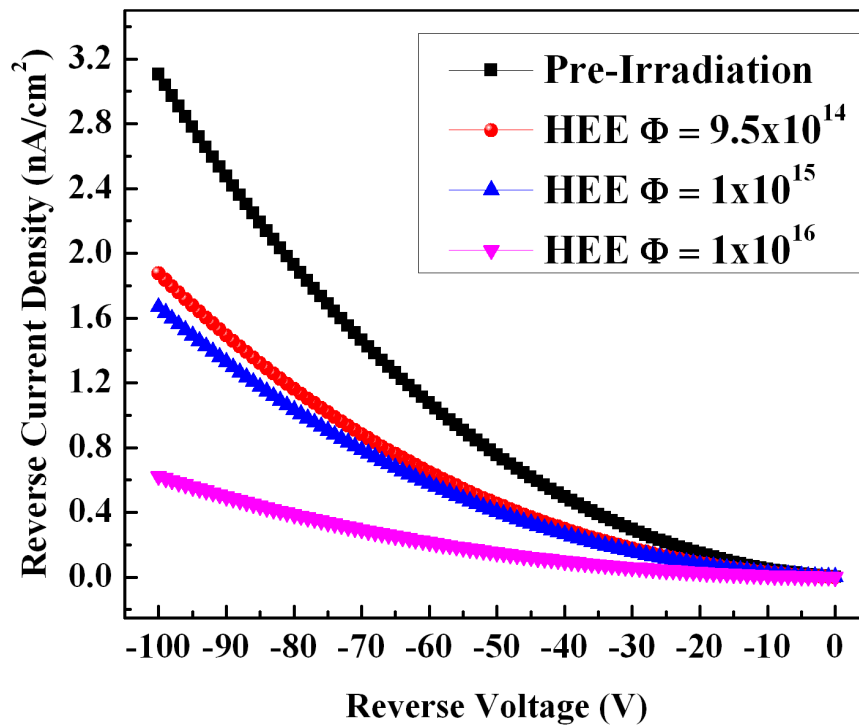
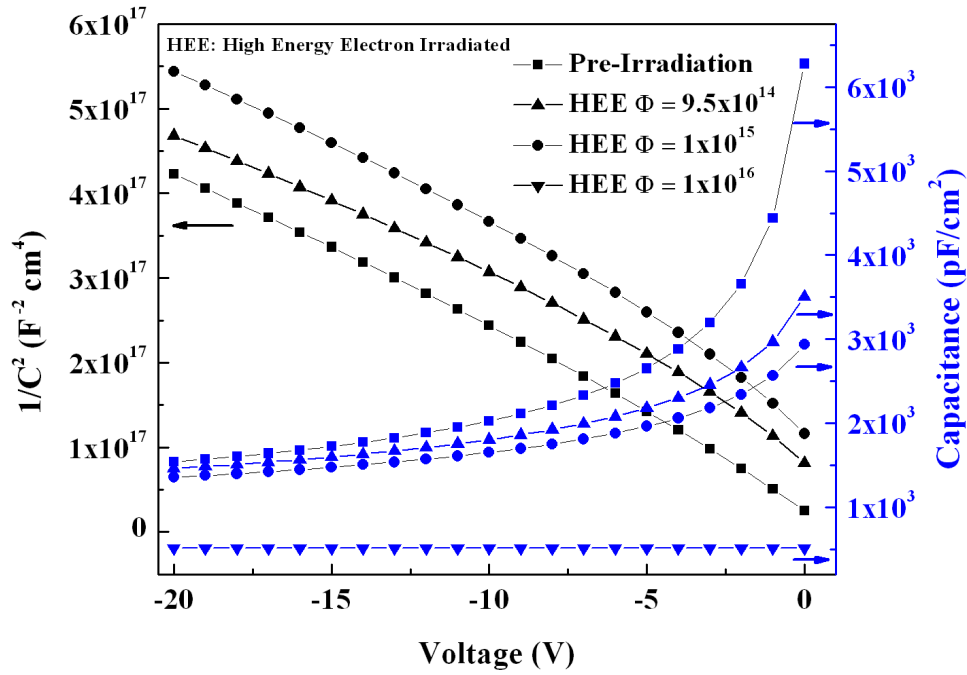


Figure 5.9 Reverse characteristics of Ni/4H-SiC SBD before and after the 8.2 MeV high energy electron irradiations at different fluence levels.



**Figure 5.10** Simulated  $C$ - $V$ -characteristics of Ni/4H-SiC SBD before and after the 8.2 MeV high energy electron (HEE) irradiations at different fluence levels. Due to flat  $C$ - $V$ -curve at the fluence of  $10^{16}$  electrons/cm<sup>2</sup>, the  $(1/C^2)$ - $V$  plot for that fluence level could not be estimated.

### 5.3.4 Characteristics of 6.5 MeV proton-irradiated Ni/4H-SiC SBD detector

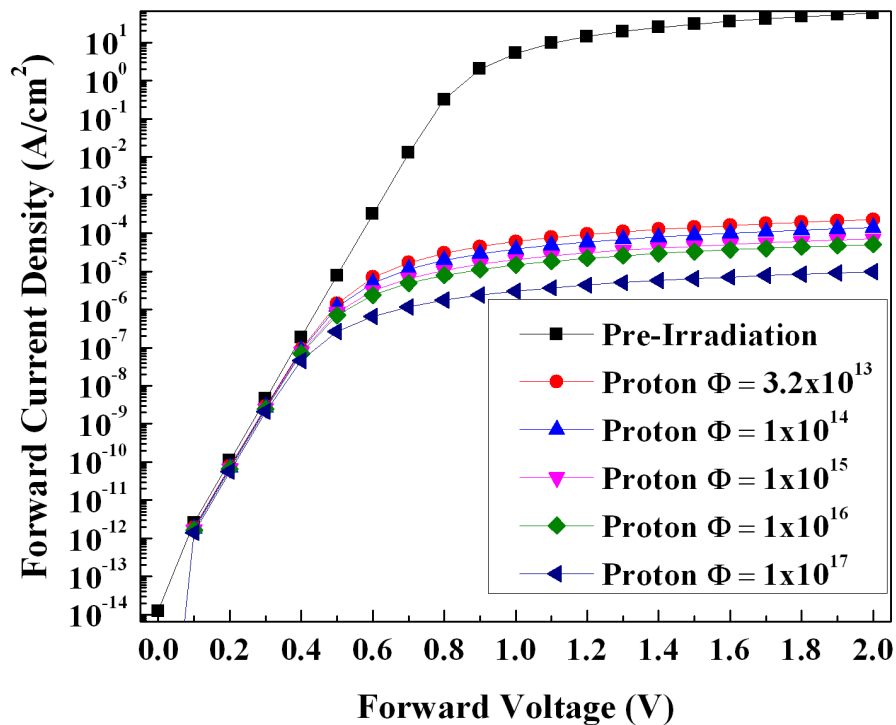
Table 5.5 shows the properties of deep-levels identified in 6.5 MeV proton irradiated Ni/4H-SiC. These levels are incorporated in proton-irradiated SiC model. Figure 5.11 represents the forward  $J$ - $V$ -characteristics, and Figure 5.12 shows the reverse characteristic of Ni/4H-SiC-based SBD before and after the proton irradiation. It can be observed that forward current is decreasing in this case as well. It is due to the increase in the  $R_S$  as described in the previous section. The reduction in the reverse current is due to the considerable decrease in the effective doping concentration ( $N_{eff}$ ). To determine the effect of irradiation on the  $N_{eff}$ , the  $C$ - $V$ -simulations are performed. Figure 5.13 shows the simulated  $C$ - $V$ -characteristics of the SiC-based SBD before and after the irradiation of 6.5 MeV energetic protons. The  $N_{eff}$  after the proton irradiation with fluence =  $3.2 \times 10^{13}$  protons/cm<sup>2</sup> is estimated to be  $6.03 \times 10^{14}$  cm<sup>-3</sup> from the  $(1/C)^2$ - $V$  curve of Figure 5.13. The change in  $N_{eff}$  is due to the compensation of donors by the irradiation-induced acceptor-type

deep-levels in SiC band-gap. The flat C-V-characteristics after the fluence  $10^{17}$  protons/cm<sup>2</sup> reveals that the donor density in the SiC-SBD epilayer is almost completely compensated and therefore, the *n*-type SiC has become intrinsic.

**Table 5.5 Properties of traps introduced in 6.5 MeV proton-irradiated SiC-based SBD (Fluence =  $3.2 \times 10^{13}$  protons/cm<sup>2</sup>) [55].**

E.LEVEL ( $E_c - E_t$ ) (eV)	DENSITY ( $N_T$ ) (cm <sup>-3</sup> )	SIGN ( $\sigma_n$ ) (cm <sup>2</sup> )	Introduction rate $\eta_r = N_T / \Phi_F$ (cm <sup>-1</sup> )
0.18	$1.0 \times 10^{13}$	$2 \times 10^{-14}$	$\sim 0$
0.20	$6.3 \times 10^{13}$	$7 \times 10^{-18}$	3.2
0.40	$1.3 \times 10^{14}$	$1 \times 10^{-15}$	4.1
0.72	$3.5 \times 10^{14}$	$2 \times 10^{-14}$	11.0
0.76	$1.1 \times 10^{14}$	$1 \times 10^{-14}$	3.5
1.09	$7.7 \times 10^{14}$	$5 \times 10^{-13}$	2.4

E.LEVEL, DENSITY, SIGN, are the Silvaco parameters of TRAP statement for trap energy location in band-gap, the density of traps and electron capture cross-section, respectively. The  $\sim 0$  introduction rate means that  $N_T$  is constant at higher fluence



**Figure 5.11 Forward characteristics ( $\ln J$ - $V$  plot) of Ni/4H-SiC SBD before and after the 6.5 MeV proton irradiations at various fluence levels.**

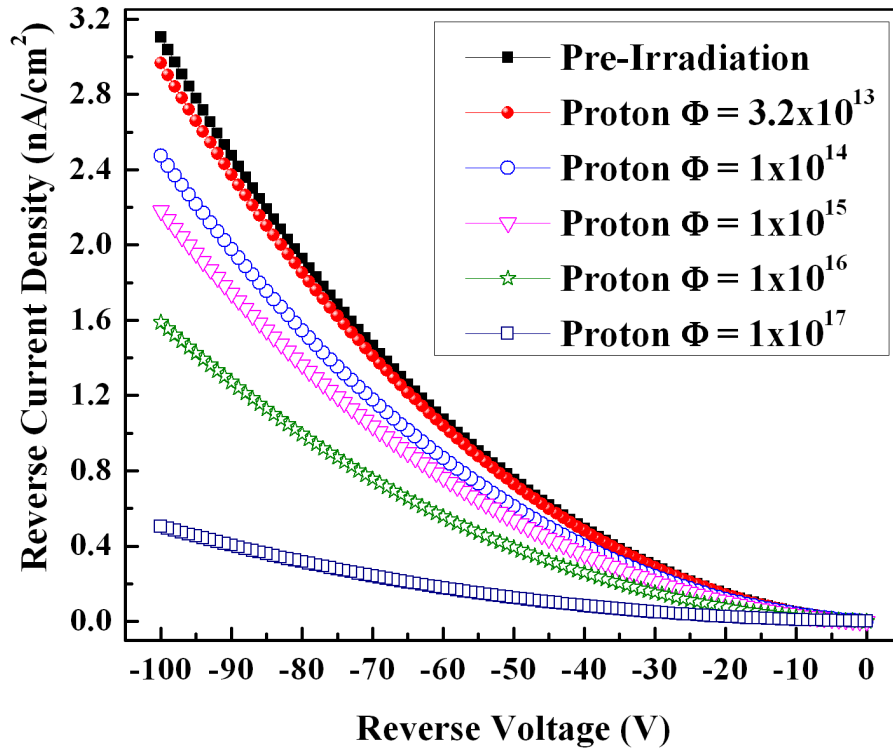


Figure 5.12 Reverse characteristics of Ni/4H-SiC SBD before and after the 6.5 MeV proton irradiations at different fluence levels.

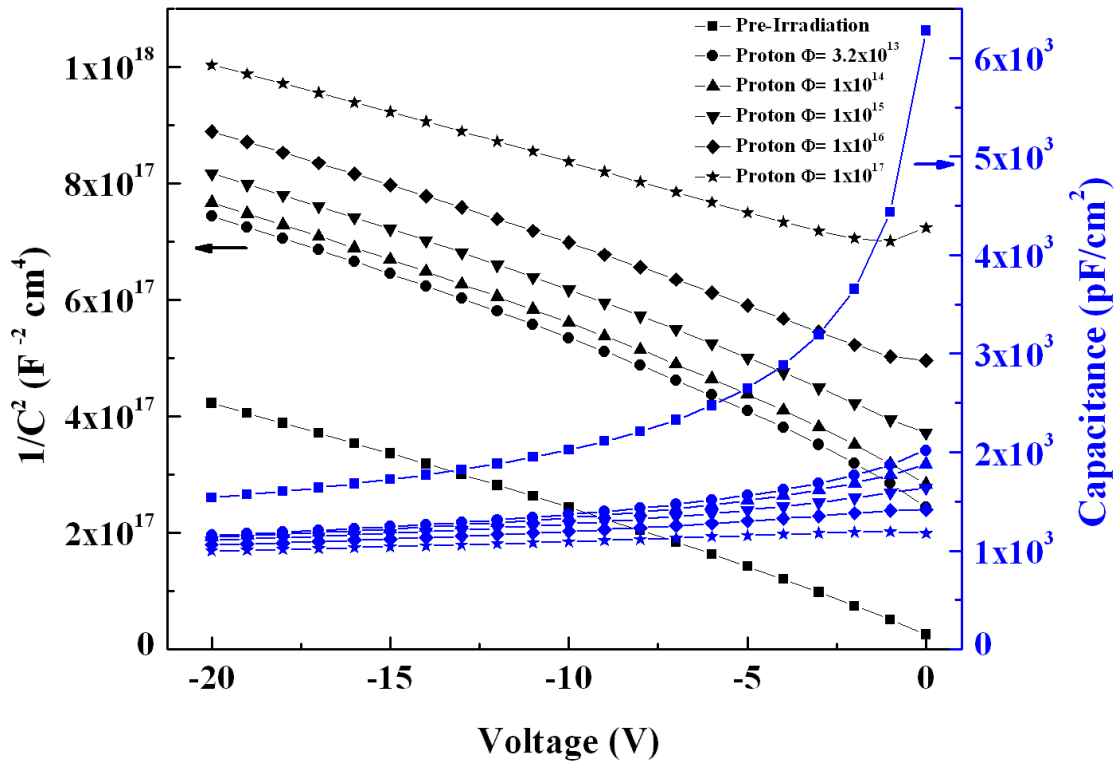


Figure 5.13 Simulated C-V-characteristics of Ni/4H-SiC SBD before and after the 6.5 MeV proton irradiations at different fluence levels.

The carrier removal rate after the proton-irradiation in 4H-SiC is estimated as:  $5.53 \text{ cm}^{-1}$ , which is less than the carrier removal rate reported for the proton-irradiated Si ( $\sim 200 \text{ cm}^{-1}$ ) [87]. The device parameters such as  $\eta$ ,  $\phi_B$ ,  $R_S$ ,  $V_{bi}$ , *etc.*, are estimated from the forward and reverse  $J$ - $V$ -characteristics of 4H-SiC SBD and tabulated in Table 5.7.

### 5.3.5 Characteristics of Neutron-irradiated Ni/4H-SiC SBD detector

A two-level defect model has been incorporated for the simulation of 1 MeV equivalent neutron irradiation induced effects on the electrical characteristics of SiC-based SBD. These two defect levels (traps) are prominent with high introduction rate ( $\eta_r$ ) in SiC devices which are subjected to neutron fluence higher than  $10^{14}$  neutrons/cm<sup>2</sup> [57], [58], [78], [87], [117], [118]. These levels are also extremely stable against high-temperature annealing [29], [56]. Therefore, these trap levels are going to affect the device characteristics at elevated temperatures. The properties of the trap levels defined in 1 MeV equivalent neutron irradiated SiC-SBD after the fluence of  $\sim 1 \times 10^{11}$  neutrons/cm<sup>2</sup> and their introduction rates are tabulated in Table 5.6. For simulating the device at higher fluence, the density of defect level ( $N_T$ ) is calculated from the introduction rate.

**Table 5.6 Trap signatures introduced in 1 MeV equivalent neutron-irradiated Ni/4H-SiC SBD detector model at the fluence of  $1 \times 10^{11}$  neutrons/cm<sup>2</sup> [29], [56], [58].**

E.LEVEL ( $E_c - E_t$ ) (eV)	DENSITY ( $N_T$ ) (cm <sup>-3</sup> )	SIGN ( $\sigma_n$ ) (cm <sup>2</sup> )	Introduction rate $\eta_r = N_T / \Phi_F$ (cm <sup>-1</sup> )	Possible defects
0.63	$1.5 \times 10^{13}$	$5 \times 10^{-16}$	4.0	$Z_{1/2}$
1.55	$2 \times 10^{13}$	$3 \times 10^{-17}$	1.4	$EH_{6/7}$

E.LEVEL, DENSITY, SIGN, are the Silvaco parameters of TRAP statement for trap energy location in band-gap, the density of traps and electron capture cross-section, respectively.

Figure 5.14 shows the forward  $J$ - $V$ -characteristics at various neutron fluences. It can be observed that up to the fluence of  $10^{13}$  neutrons/cm<sup>2</sup>, there is a minimal effect on the forward characteristics. At fluence higher than  $10^{14}$  neutrons/cm<sup>2</sup>,  $J_F$  has reduced significantly. It is due to the dramatic increase in the bulk resistivity after the neutron

irradiation. It is also found that the  $J_F$  has diminished to the orders of nanoamperes at around the fluence of  $10^{16}$  neutrons/cm<sup>2</sup>. Figure 5.15 shows the simulated  $J_F$  and  $J_R$  as a function of neutron fluence, estimated at +2 V and −100 V respectively. It can be observed that the current density is decreasing in both forward as well as reverse bias after the neutron irradiation. A point worth to note here is that at higher fluence, the current-density in forward bias is approaching towards the order of current density in reverse bias. In literature, Nava *et al.*, [57] have also reported the same current-density in both of the bias polarization at fluence higher than  $8 \times 10^{14}$  n/cm<sup>2</sup>. In that report, the authors have reported equal current densities at forward and reverse bias of +2V and −200 V, respectively.

The simulated reverse  $J$ - $V$ -characteristics at various neutron fluences has been illustrated in Figure 5.16. The  $J_R$  is found to decrease with increasing neutron fluence, contrary to the neutron-irradiated Si-based devices. The simulated  $(I/C^2)$ - $V$  curve is plotted in Figure 5.17 for determining the  $\phi_{BCV}$ , and  $N_{eff}$  after various neutron fluences on Ni/4H-SiC SBD. The doping concentration has reduced to  $5.5 \times 10^{14}$  cm<sup>-3</sup> after irradiation with  $10^{14}$  n/cm<sup>2</sup> from the pre-irradiation value of  $7.8 \times 10^{14}$  cm<sup>-3</sup>. The change in  $N_{eff}$  is due to the compensation of donors by the neutron irradiation generated acceptor-type trap levels. The flat  $C$ - $V$ -characteristics after the fluence of  $10^{16}$  n/cm<sup>2</sup> suggest that the donor density in the SiC-SBD epitaxial layer is almost completely compensated and thus the  $n$ -type SiC has become intrinsic. The reduction in doping concentration also caused the electric field to reduce at Ni and SiC interface (similar to the Figure 5.5 for  $\gamma$ -irradiated SBDs), which is the reason for the reduction in the reverse current at higher neutron fluences. The carrier removal rate after the neutron-irradiation in 4H-SiC is estimated to be  $\sim 2.5$  cm<sup>-1</sup> which is in good agreement with the value reported in the literature (4.5 cm<sup>-1</sup>) and also lower than the value for Si-based devices [87].



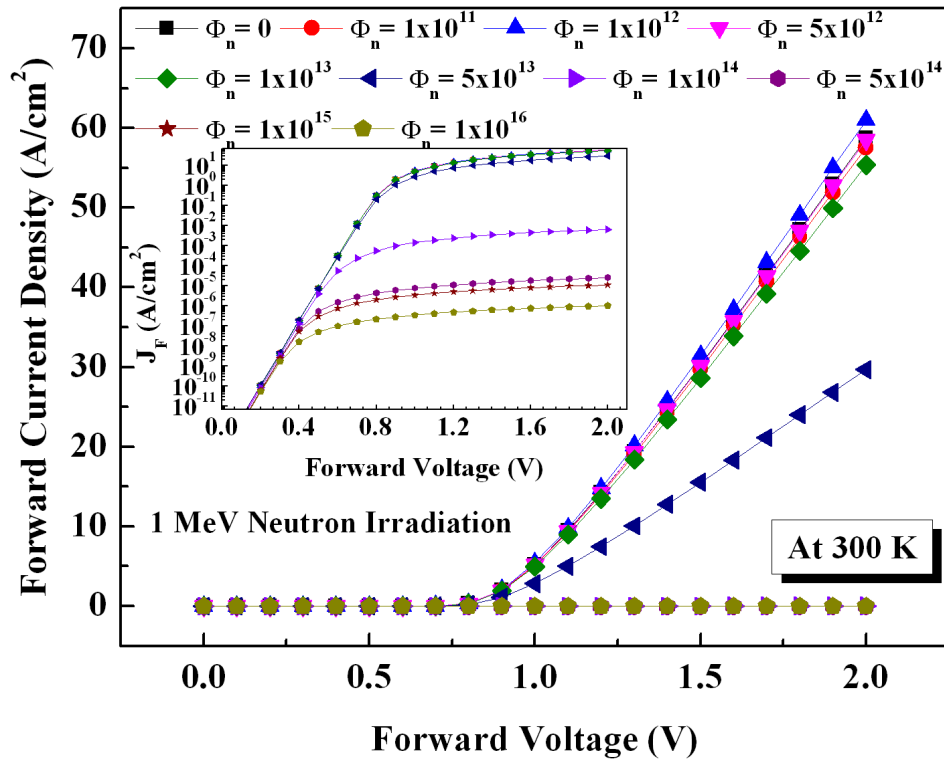


Figure 5.14 Simulated forward  $J$ - $V$ -characteristics of Ni/4H-SiC SBD prior to and after the neutron irradiation of various fluences ( $0, 10^{11} - 10^{16}$  neutrons/cm<sup>2</sup>) (Inset:  $\ln(J)$ - $V$  plot).

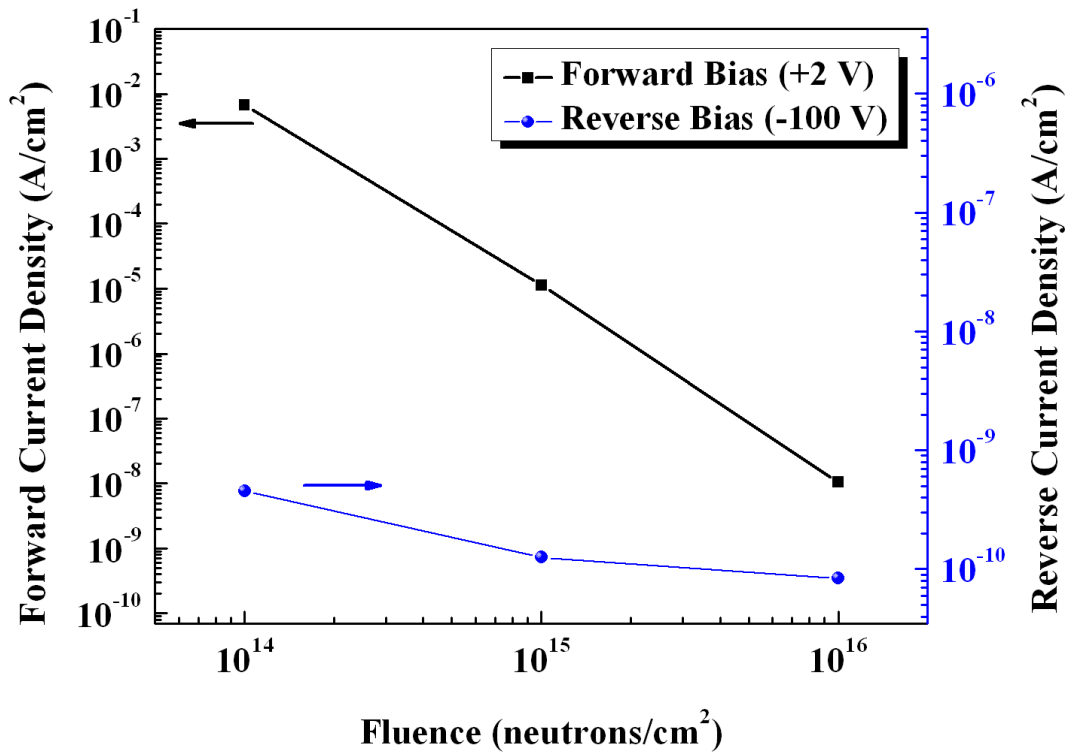


Figure 5.15 Simulated forward and reverse current density as a function of neutron fluence, calculated at +2 V and -100 V, respectively.

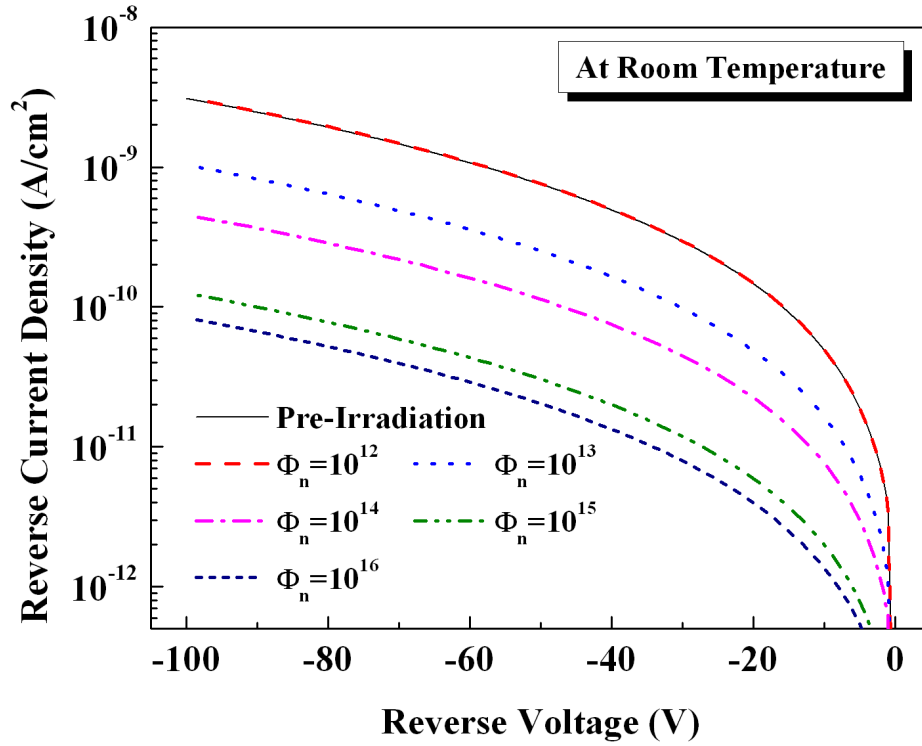


Figure 5.16 Simulated reverse  $J$ - $V$ -characteristics of Ni/4H-SiC SBD prior to and after the neutron irradiation at various fluences ( $\Phi_n = 10^{12} - 10^{16}$  neutrons/cm<sup>2</sup>).

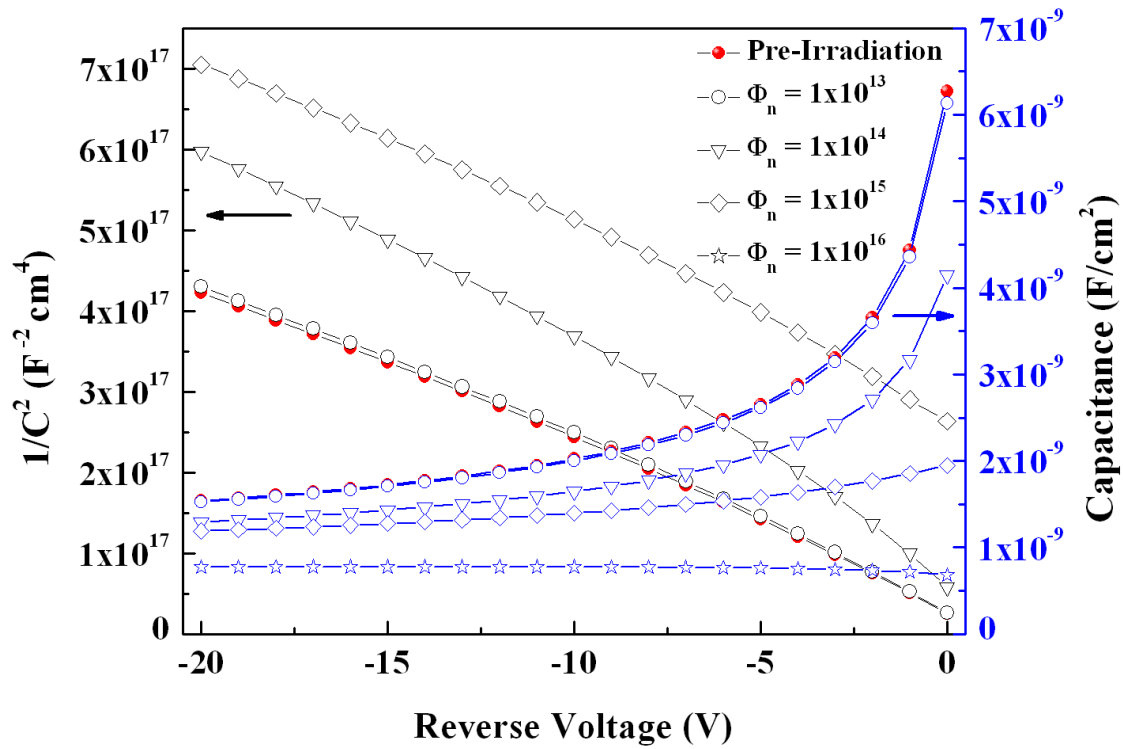


Figure 5.17 Simulated  $(1/C^2)$ - $V$  and  $C$ - $V$ -characteristics of Ni/4H-SiC SBD prior to and after the neutron-irradiation of various fluences. Due to flat  $C$ - $V$ -curve at the fluence of  $10^{16}$  n/cm<sup>2</sup>, the  $(1/C^2)$ - $V$  plot for that fluence level could not be estimated.

The device parameters calculated from the  $I$ - $V$ ,  $C$ - $V$  data after the neutron irradiation are tabulated in Table 5.7. Since the simulated  $C$ - $V$  response was flat after the neutron fluence greater than  $5 \times 10^{15}$  neutrons/cm<sup>2</sup>, the device parameters could not be estimated. Also, the ideality factor becomes so large to offer any reliable estimation. However, Figure 5.18 shows the improvement in breakdown characteristics of SiC-based SBD after the neutron irradiation which is a point worth noting. Due to this the detector under irradiation may be biased at higher reverse biased in order to compensate the decrease in the depletion region caused due to irradiation.

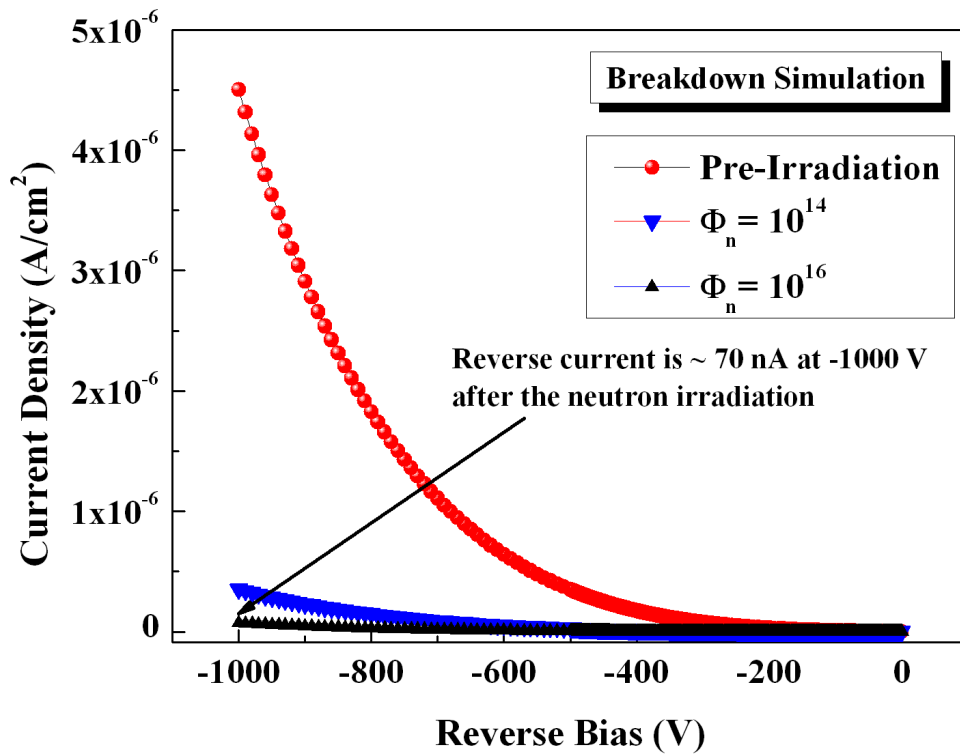


Figure 5.18 The breakdown simulation of Ni/4H-SiC SBD before and after the neutron irradiations.

#### 5.4 SUMMARY

In this chapter, Silvaco TCAD simulations are carried out to evaluate the ageing of SiC-based SBD detectors that are subjected to heavy irradiations. The device simulation at various fluences of 8.2 MeV electrons, 6.5 MeV protons and 1 MeV equivalent neutrons reveal that the forward and reverse leakage current density decreases considerably after the

fluence of  $1 \times 10^{14}$  particles/cm<sup>2</sup>. After high fluence ( $> 5 \times 10^{15}$  particles/cm<sup>2</sup>), flat C-V characteristics are obtained which suggest that n-type SiC has become intrinsic due to the compensation of donors.

As a result of this study, it is recommended to expose the SiC-based SBD neutron detectors below the fluence of  $5 \times 10^{15}$  particles/cm<sup>2</sup> for reliable device behavior.

**Table 5.7 Device parameters determined from the I-V & C-V simulations of the Ni/4H-SiC SBD.**

		I-V- Simulations			C-V-Simulations				
Device Parameters		$\phi_{B_{IV}}$ (eV)	$\eta$	$R_s$ ( $\Omega$ )	$V_{bi}$ (V)	$E_f$ (eV)	$\Delta\phi_{bl}$ (eV)	$\phi_{B_{CV}}$ (eV)	$N_{eff}$ (cm <sup>-3</sup> ) $\times 10^{14}$
	Temp (K)								
Pre-irradiation	300	0.95	2.44	55	0.999	0.236	0.0157	1.28	7.8
	373	1.03	2.49	69	0.897	0.304	0.0153	1.25	7.42
	473	1.20	2.54	88	0.748	0.4	0.0146	1.19	7.41
	523	1.29	2.57	97	0.682	0.449	0.0143	1.18	7.38
	Dose (Mrad)	At Room temperature							
Gamma	100	1.19	2.46	229	1.774	0.270	0.0163	2.03	4.84
	Fluence ( $\Phi_F$ )	At Room temperature							
8.2 MeV Electron	$9.5 \times 10^{14}$	1.04	3.68	$2.26 \times 10^6$	0.82	0.235	0.0151	1.11	7.06
	$1 \times 10^{15}$	1.03	3.85	$3.77 \times 10^6$	1.16	0.237	1.0160	1.38	6.92
	$1 \times 10^{16}$	0.98	11.01	$8.38 \times 10^9$	-	-	-	-	-
6.5 MeV Proton	$3.2 \times 10^{13}$	1.03	3.79	$3.16 \times 10^6$	1.75	0.242	0.0170	1.98	6.03
	$1 \times 10^{14}$	1.02	3.94	$4.9 \times 10^6$	1.89	0.241	0.0174	2.11	5.9
	$1 \times 10^{15}$	1.02	4.19	$9.5 \times 10^6$	3.41	0.240	0.0205	3.63	4.32
	$1 \times 10^{16}$	1.01	4.31	$12.3 \times 10^6$	3.69	0.238	0.0213	3.91	3.75
	$1 \times 10^{17}$	0.99	5.12	$55.8 \times 10^6$	-	-	-	-	-
1 MeV equivalent Neutron	$1 \times 10^{12}$	1.19	2.38	53	0.988	0.235	0.0158	1.2	7.6
	$1 \times 10^{15}$	1.06	5.09	$4.6 \times 10^7$	9.753	0.239	0.0271	9.96	4.68
	$1 \times 10^{16}$	1.04	6.87	$4.21 \times 10^8$	-	-	0.031	-	-

\*\*\*\*\*

# 6

## SUMMARY, CONCLUSIONS AND FUTURE DIRECTIONS

---

### 6.1 SUMMARY & CONCLUSIONS

Neutron detectors are an inevitable component of a Neutron Flux Monitoring System (NFMS) in a nuclear power plant. They measure neutron flux at various core locations by which various signals such as absolute power, rate of change of power (period), change in reactivity are generated to enable control of the reactor power and also to initiate safety actions on crossing threshold. Hence, a reliable and fast acting neutron flux monitoring system is necessary for ensuring core safety at all states of its operation. The state-of-the-art gas-filled neutron detectors such as fission chambers,  $^{10}\text{B}$  and  $\text{BF}_3$  proportional counters, and  $^{10}\text{B}$  based Compensated Ion Chambers (CICs) are generally deployed for this purpose.

In a pool type sodium cooled fast reactor such as the Indian 500 MWe Prototype Fast Breeder Reactor (PFBR), it is very challenging to monitor neutron flux over ten decades spanning from shutdown to full power with a single detector system. Also, due to thick radial and axial in-vessel shielding, the neutron flux is highly attenuated at the ex-core and ex-vessel detector locations and hence a combination of detectors working in different modes (pulse mode, Campbell mode and pulse mode with linear count rate meters) are used. The presence of harsh environments such as high temperature ( $\sim 500^\circ\text{C}$ ), high gamma dose (100 Mrad), and high neutron fluxes ( $\sim 10^{15} \text{ n/cm}^2/\text{s}$ ) within the vessel, necessitates the design of harsh environment detectors such as high-temperature fission chambers (HTFCs).

The evolving safety requirements for the next generation reactor design demands improved reliability of the safety systems. To increase the reliability, the inclusion of diverse neutron detectors in the design of NFMS is envisaged. The alternative to the existing gas-filled detectors could be the detectors based on scintillators or semiconductors. The scintillators are not considered for this study as they cease to withstand the harsh-environment of fast reactors and are poor in terms of gamma-discrimination. Hence, a detailed & systematic survey has been carried out for semiconductor based detectors. Literature has shown the potential of a wide band-gap semiconductor, i.e., Silicon Carbide (SiC) for harsh environment monitoring. The wide band-gap of SiC ( $E_g = 3.25$  eV for 4H-SiC), which is approximately three times that of Si ( $E_g = 1.1$  eV), and low intrinsic carrier concentration make SiC-based devices suitable for high-temperature operations in comparison to Si-based devices. Moreover, SiC can be used in direct as well as indirect conversion configurations to detect the neutrons. However, in indirect configuration, it offers better efficiency. In indirect conversion, SiC-based diode is coated with neutron-sensitive converter material, which generates charged particles upon interaction with neutrons. These charged particles are subsequently detected in the semiconductor depletion region.

Towards the development of a SiC-based fast neutron detector, the following aspects are to be studied and resolved:

- a) The planar structure has an inevitable geometrical limitation because the probability of neutron interaction in a planar structure depends strongly on the thickness of the neutron sensitive converter layer. The probability of the neutron interaction increases with the thickness of the converter, but at the same time, it reduces the probability of resultant secondary charged particles to reach the active (depletion) region of the semiconductor (due to continuous energy loss in the

matter). Therefore, for each converter material, there is an optimum thickness at which maximum number of reaction products would reach in the semiconductor depletion region. The optimum thickness of the converter is not viable to determine through experiments.

- b) The neutron interactions with matter depend on incident neutron's energy. Therefore, the optimum thickness for a particular neutron source may not provide maximum efficiency for other neutron sources.
- c) The neutron field is generally accompanied with several background radiations such as  $\gamma$ -rays. The discrimination of these radiations is essential for reliable counts and it is done by applying Low-Level Discriminator (LLD). The LLD also eliminates several low energy charged particles which are generated due to neutron interactions. Hence, the effect of discrimination on neutron detection efficiency needs to be quantified. Furthermore, the efficiency offered by the semiconductor detectors is too low for reliable and consistent monitoring. Thus, further studies are needed to enhance the efficiency of this planar SiC-based detector.
- d) The semiconductor device characteristics degrade at high doses of radiation. The parameters that are affected due to irradiation are: a) increase in the leakage current of the device, b) increase in the depletion voltage, c) decrease in effective doping concentration which leads to type inversion, d) degradation of charge collection properties of the device, etc. Hence, it is prudent to examine the electrical performance of SiC-based device with increasing fluence. This study would help in determining its useful life and possible location for deployment.

The present research is focused on addressing the above mentioned potential areas.

Following are the significant achievements of this research work:

- A planar detector is modeled using a Monte-Carlo tool GEANT4 for optimizing the thicknesses of various neutron sensitive converters for several energy neutron sources. The modeled detector is benchmarked against the published simulation and experimental results for HDPE converter. The simulation results showed an excellent agreement with the literature.
- The reported optimized thicknesses for HDPE converter material corresponding to 2.5 MeV D-D neutron source and neutrons of  $^{239}\text{Pu}$ -Be spectrum are not sufficient for efficiently detecting the wide energy neutron spectrum of a typical fast reactor. Therefore, HDPE thickness is further optimized for several mono-energetic neutron sources. Based on the simulations, a 400  $\mu\text{m}$  thick HDPE is proposed to be coated as a converter on SiC for fast neutron flux monitoring in ex-vessel location of the fast reactors where temperature is  $< 90\text{ }^{\circ}\text{C}$ . The simulation revealed that the maximum efficiency of  $\sim 0.112\%$  can be achieved. The effect of background discrimination on neutron detection efficiency shows the trade-off, i.e., for achieving higher discrimination one has to accept lower efficiency and vice versa. To enhance the efficiency, a stacked detector configuration is propounded. The efficiency is enhanced up to  $\sim 1.04\%$  and  $\sim 3.85\%$  with 10 and 50 stacked layers, respectively. However, fabrication of the stacked detector and signal generation need further detailed study.
- For in-vessel locations, where temperature and neutron flux is very high, a novel LiH-SiC-based detector is proposed for the first time. LiH has a high hydrogen content (12.68 wt. % H in LiH) and very high melting point ( $688\text{ }^{\circ}\text{C}$ ). Further,  $^7\text{Li}$ -isotope, which is in abundance, is entirely transparent to the neutrons. Therefore, majority of the neutrons will interact with the hydrogen content of the LiH and will generate recoil



protons, which will be collected in SiC active region to form the detector signal. The thickness of LiH is optimized with the help of GEANT4. The maximum efficiency of  $\sim 0.1\%$  is achieved with 500  $\mu\text{m}$  thick LiH. The stacked structure of LiH-SiC-based detector can achieve maximum neutron detection efficiency of 0.93% with 10 layers in the stack and 3.25% with 50 stacked layers.

- Another important work performed using the device simulation tool TCAD for assessing the degradation in the performance of the SiC-based Schottky Barrier Diodes (SBDs) with increasing fluence. The electrical characteristics of  $n$ -type Ni/4H-SiC-based SBDs are simulated before and after the irradiation of several particles viz., gamma (dose = 100 Mrad), 8.2 MeV electron, 6.5 MeV proton and 1 MeV equivalent neutron sources. The forward and reverse currents of 4H-SiC-SBD are observed to be decreasing following the particle irradiation. The reduction in the forward current density can be attributed to the increase in the series resistance whereas the reduction in reverse current is due to the compensation of doping concentration by the acceptor-type trap level generated in SiC band-gap by the impinging radiation particles. Another important consequence of the increase in fluence of irradiation is the transformation of diode properties from a rectifying to ohmic one, which was inferred from the progressive decrease in gap between the forward and reverse currents. The quantitative behavior of diodes in terms of ideality factor shows that its properties have been degraded drastically with the increase in neutron fluence beyond  $5 \times 10^{15} \text{ n/cm}^2$ . The results are highly promising for the development of SiC-based neutron detectors for applications in fast reactors.

*To conclude, a novel LiH-SiC-based stacked neutron detector has been optimized and the effects of irradiation on the SiC device characteristics have been assessed for its applications in the harsh environment of fast reactors.*

### 6.2 SCOPE FOR THE FUTURE WORK

The following studies are recommended before the fabrication of the detector:

- The first important aspect is the development of the coating techniques for several converter materials such as HDPE, LiH on the SiC-based devices.
- The effect of converter coating on the device performance has to be studied.
- In GEANT4 simulations, the effect of temperature on neutron interaction cross-section is not included. At elevated temperatures, due to Doppler Effect, neutron cross-section reduces which results in lower detection efficiency. Similarly, the dead layer effect also to be included.
- Another device configuration such as SiC-based PiN diode could also be explored as a detector.
- Finally, the most important work that can be taken up is the fabrication of a prototype detector and experimental validation of the simulation results.

\*\*\*\*\*

# REFERENCES

- [1] G. E. Bacon and K. Lonsdale, "Neutron diffraction," *Reports on Progress in Physics*, vol. 16, no. 1, pp. 1–61, Jan. 1953.
- [2] D. F. C. Morris, "Neutron-Activation Analysis," *Metallurgical Reviews*, vol. 7, no. 1, pp. 241–281, Jan. 1962.
- [3] Kavita Nedunchezian, "Boron Neutron Capture Therapy - A Literature Review," *Journal Of Clinical And Diagnostic Research*, 2016.
- [4] P. Vontobel, E. H. Lehmann, R. Hassanein, and G. Frei, "Neutron tomography: Method and applications," *Physica B: Condensed Matter*, vol. 385–386, pp. 475–480, Nov. 2006.
- [5] S. Glasstone, *Nuclear Reactor Engineering: Reactor Design Basics*, 4th Edition edition., vol. 1, 2 vols. New Delhi: cbspd, 2004.
- [6] P. Rinard, "Neutron interactions with matter," in *Passive Nondestructive Assay of Nuclear Materials*, Nuclear Regulatory Commission, 1991, pp. 357–377.
- [7] "DOE Fundamentals Handbook: Nuclear Physics And Reactor Theory." U.S. Department of Energy.
- [8] M. Sivaramakrishna, C. P. Nagaraj, K. Madhusoodanan, and P. Chellapandi, "Neutron Flux Monitoring System in Prototype Fast Breeder Reactor," *International J. of Engg. and Innovative Technology (IJEIT)*, vol. 3, no. 10, 2014.
- [9] G. F. Knoll, *Radiation Detection and Measurement*, 4th Edition edition. John Wiley & Sons, 2010.
- [10] P. Chellapandi, P. R. V. Rao, and P. Kumar, "Fast reactor programme in India," *Pramana - J Phys*, vol. 85, no. 3, pp. 525–538, Sep. 2015.
- [11] P. Puthiyavinayagam *et al.*, "Development of fast breeder reactor technology in India," *Progress in Nuclear Energy*, vol. 101, pp. 19–42, Nov. 2017.
- [12] M. Bruzzi, "Radiation damage in silicon detectors for high-energy physics experiments," *IEEE Transactions on Nuclear Science*, vol. 48, no. 4, pp. 960–971, Aug. 2001.
- [13] D. Passeri, P. Ciampolini, G. M. Bilei, and F. Moscatelli, "Comprehensive modeling of bulk-damage effects in silicon radiation detectors," *IEEE Transactions on Nuclear Science*, vol. 48, no. 5, pp. 1688–1693, Oct. 2001.
- [14] H. J. Ziock *et al.*, "Temperature dependence of radiation damage and its annealing in silicon detectors," in *IEEE Conference on Nuclear Science Symposium and Medical Imaging*, Orlando, FL, USA, 1992, pp. 813–815.
- [15] E. Barberis *et al.*, "Temperature effects on radiation damage to silicon detectors," *Nucl. Instrum. Methods Phys. Res. A*, vol. 326, no. 1–2, pp. 373–380, Mar. 1993.

- [16] S. Seshadri, A. R. Dulloo, and F. H. Ruddy, "An advanced SiC nuclear radiation detector," 1997, pp. 114–115.
- [17] F. P. Doty, "Boron nitride solid state neutron detector," US6727504 B1, 27-Apr-2004.
- [18] D. E. Holcomb, B.-S. Moon, D. W. Miller, and J. W. Talnagi, "Aluminum Nitride as an Alternative Local Power Range Monitoring Technology," in *IAEA Technical Meeting*, 2005.
- [19] D. S. McGregor, R. T. Klann, H. K. Gersch, and Y. H. Yang, "Thin-film-coated bulk GaAs detectors for thermal and fast neutron measurements," *Nucl. Instrum. Methods Phys. Res. A*, vol. 466, no. 1, pp. 126–141, 2001.
- [20] P. Mulligan, J. Wang, and L. Cao, "Evaluation of freestanding GaN as an alpha and neutron detector," *Nucl. Instrum. Methods Phys. Res. A*, vol. 719, pp. 13–16, Aug. 2013.
- [21] S. Seshadri, A. R. Dulloo, F. H. Ruddy, J. G. Seidel, and L. B. Rowland, "Demonstration of an SiC neutron detector for high-radiation environments," *IEEE Transactions on Electron Devices*, vol. 46, no. 3, pp. 567–571, Mar. 1999.
- [22] F. Franceschini and F. H. Ruddy, *Silicon Carbide neutron detectors*. INTECH Open Access Publisher, 2011.
- [23] F. H. Ruddy, A. R. Dulloo, J. G. Seidel, M. K. Das, S.-H. Ryu, and A. K. Agarwal, "The fast neutron response of 4H silicon carbide semiconductor radiation detectors," *IEEE Transactions on Nuclear Science*, vol. 53, no. 3, pp. 1666–1670, Jun. 2006.
- [24] R. W. Flammang, J. G. Seidel, and F. H. Ruddy, "Fast neutron detection with silicon carbide semiconductor radiation detectors," *Nucl. Instrum. Methods Phys. Res. A*, vol. 579, no. 1, pp. 177–179, Aug. 2007.
- [25] T. Madi Filho, M. M. Hamada, F. Shiraishi, and C. H. de Mesquita, "Development of neutron detector using the surface barrier sensor with polyethylene (n, p) and  $^{10}\text{B}$  (n,  $\alpha$ ) converters," *Nucl. Instrum. Methods Phys. Res. A*, vol. 458, no. 1, pp. 441–447, 2001.
- [26] E. Omotoso, "Electrical characterization of process- and radiation-induced defects in 4H-SiC," PhD Thesis, University of Pretoria, 2016.
- [27] A. T. Paradzah, "Electrical characterisation of particle irradiated 4H-SiC," M.S. Dissertation, University of Pretoria, 2014.
- [28] Sei-Hyung Ryu, A. K. Agarwal, R. Singh, and J. W. Palmour, "1800 V NPN bipolar junction transistors in 4H-SiC," *IEEE Electron Device Letters*, vol. 22, no. 3, pp. 124–126, Mar. 2001.
- [29] T. Kimoto and J. A. Cooper, *Fundamentals of Silicon Carbide Technology: Growth, Characterization, Devices, and Applications*. Singapore: John Wiley & Sons Singapore Pte. Ltd, 2014.

- 
- [30] G. L. Harris and Institution of Electrical Engineers, Eds., *Properties of silicon carbide*. London: INSPEC, the Inst. of Electrical Engineers, 1995.
- [31] P. G. Neudeck, "Progress in silicon carbide semiconductor electronics technology," *Journal of Electronic Materials*, vol. 24, no. 4, pp. 283–288, Apr. 1995.
- [32] Ajay Kumar and M S Aspalli, "SiC: An Advanced Semiconductor Material For Power Devices," *International Journal of Research in Engineering and Technology*, vol. 03, no. 03, pp. 248–252, May 2014.
- [33] Cyril Buttay, Christophe Raynaud, Hervé Morel, Mihai Lazar, Gabriel Civrac, and Dominique Bergogne, "High-temperature behavior of SiC power diodes," in *Proceedings of the 2011 14th European Conference on Power Electronics and Applications*, Birmingham, 2011.
- [34] M. Nakagawa, S. Mori, Y. Nanen, M. Aketa, H. Asahara, and T. Nakamura, "Investigation of thermal runaway of reverse-biased silicon carbide schottky barrier diode," in *2017 IEEE International Meeting for Future of Electron Devices, Kansai (IMFEDK)*, Kyoto, Japan, 2017, pp. 90–91.
- [35] C. Bodeker, T. Vogt, D. Silber, and N. Kaminski, "Investigation of the thermal runaway of silicon carbide diodes during blocking operation," in *2015 17th European Conference on Power Electronics and Applications (EPE'15 ECCE-Europe)*, Geneva, 2015, pp. 1–10.
- [36] T. Funaki, T. Kimoto, and T. Hikiyara, "High-temperature characteristics of SiC Schottky barrier diodes related to physical phenomena," *IEICE Electronics Express*, vol. 5, no. 6, pp. 198–203, 2008.
- [37] Alexandra R. Zelaski, "Development of a Silicon Carbide Schottky Diode Detector for Use in Determining Actinide Inventories based on Alpha Particle Spectroscopy," The Ohio State University, 2011.
- [38] S. E. Saddow and A. Agarwal, Eds., *Advances in silicon carbide processing and applications*. Boston: Artech House, 2004.
- [39] S. Sharafat, R. H. Jones, A. Kohyama, and P. Fenici, "Status and prospects for SiC-SiC composite materials development for fusion applications," *Fusion Engineering and Design*, vol. 29, pp. 411–420, Mar. 1995.
- [40] F. H. Ruddy, A. R. Dulloo, J. G. Seidel, S. Seshadri, and L. B. Rowland, "Development of a silicon carbide radiation detector," *IEEE Transactions on Nuclear Science*, vol. 45, no. 3, pp. 536–541, Jun. 1998.
- [41] A. R. Dulloo, F. H. Ruddy, J. G. Seidel, J. M. Adams, J. S. Nico, and D. M. Gilliam, "The thermal neutron response of miniature silicon carbide semiconductor detectors," *Nucl. Instrum. Methods Phys. Res. A*, vol. 498, no. 1–3, pp. 415–423, Feb. 2003.
- [42] S. Sciortino *et al.*, "Effect of heavy proton and neutron irradiations on epitaxial 4H-SiC Schottky diodes," *Nucl. Instrum. Methods Phys. Res. A*, vol. 552, no. 1–2, pp. 138–145, Oct. 2005.
-

- [43] F. H. Ruddy and J. G. Siedel, "Effects of Gamma Irradiation on Silicon Carbide Semiconductor Radiation Detectors," presented at the 2006 IEEE Nuclear Science Symposium, San Diego, CA, 2006, pp. 583–587.
- [44] F. H. Ruddy and J. G. Seidel, "The effects of intense gamma-irradiation on the alpha-particle response of silicon carbide semiconductor radiation detectors," *Nucl. Instrum. Methods Phys. Res. B*, vol. 263, no. 1, pp. 163–168, Oct. 2007.
- [45] F. H. Ruddy and J. G. Williams, "Power Monitoring In Space Nuclear Reactors Using Silicon Carbide Radiation Detectors," in *Proceedings of the Space Nuclear Conference*, San Diego, 2005, p. 8.
- [46] J. H. HA *et al.*, "4H-SiC PIN-type Semiconductor Detector for Fast Neutron Detection," in *Progress in Nuclear Science and Technology, Vol. 1, p.237-239 (2011)*, vol. 1.
- [47] J. H. Ha, S. M. Kang, S. H. Park, H. S. Kim, N. H. Lee, and T.-Y. Song, "A self-biased neutron detector based on an SiC semiconductor for a harsh environment," *Applied Radiation and Isotopes*, vol. 67, no. 7–8, pp. 1204–1207, Jul. 2009.
- [48] A. Lo Giudice *et al.*, "Performances of 4H-SiC Schottky diodes as neutron detectors," *Nucl. Instrum. Methods Phys. Res. A*, vol. 583, no. 1, pp. 177–180, Dec. 2007.
- [49] C. Manfredotti *et al.*, "SiC detectors for neutron monitoring," *Nucl. Instrum. Methods Phys. Res. A*, vol. 552, no. 1–2, pp. 131–137, Oct. 2005.
- [50] K. Sedláčková, B. Zaťko, A. Šagátová, and V. Nečas, "Monte Carlo simulations of the particle transport in semiconductor detectors of fast neutrons," *Nucl. Instrum. Methods Phys. Res. A*, vol. 709, pp. 63–67, May 2013.
- [51] H. Ohyama *et al.*, "Radiation damage of SiC Schottky diodes by electron irradiation," *Journal of Materials Science: Materials in Electronics*, vol. 16, no. 7, pp. 455–458, 2005.
- [52] A. A. Lebedev *et al.*, "Radiation Hardness of Silicon Carbide," *Materials Science Forum*, vol. 433–436, pp. 957–960, 2003.
- [53] F. Nava *et al.*, "Radiation tolerance of epitaxial silicon carbide detectors for electrons, protons and gamma-rays," *Nucl. Instrum. Methods Phys. Res. A*, vol. 505, no. 3, pp. 645–655, Jun. 2003.
- [54] J. Wu *et al.*, "Effect of neutron irradiation on charge collection efficiency in 4H-SiC Schottky diode," *Nucl. Instrum. Methods Phys. Res. A*, vol. 735, pp. 218–222, Jan. 2014.
- [55] A. Castaldini, A. Cavallini, L. Rigutti, F. Nava, S. Ferrero, and F. Giorgis, "Deep levels by proton and electron irradiation in 4H-SiC," *Journal of Applied Physics*, vol. 98, no. 5, p. 053706, Sep. 2005.
- [56] A. A. Lebedev, "Deep level centers in silicon carbide: A review," *Semiconductors*, vol. 33, no. 2, pp. 107–130, Feb. 1999.

- 
- [57] F. Nava, A. Castaldini, A. Cavallini, P. Errani, and V. Cindro, "Radiation Detection Properties of 4H-SiC Schottky Diodes Irradiated Up to  $10^{16}$  n/cm<sup>2</sup> by 1 MeV Neutrons," *IEEE Transactions on Nuclear Science*, vol. 53, no. 5, pp. 2977–2982, Oct. 2006.
  - [58] P. V. Raja, J. Akhtar, C. V. S. Rao, S. Vala, M. Abhangi, and N. V. L. N. Murty, "Spectroscopic performance studies of 4H-SiC detectors for fusion alpha-particle diagnostics," *Nucl. Instrum. Methods Phys. Res. A*, vol. 869, pp. 118–127, Oct. 2017.
  - [59] P. Vigneshwara Raja and N. V. L. Narasimha Murty, "Thermally stimulated capacitance in gamma irradiated epitaxial 4H-SiC Schottky barrier diodes," *Journal of Applied Physics*, vol. 123, no. 16, p. 161536, Apr. 2018.
  - [60] Samuel Glasstone and Alexander Sesonske, *Nuclear Reactor Engineering: Reactor Systems Engineering, 4th Edition, Vol. 2*, 4th edition. Springer, 1994.
  - [61] N. Tsoulfanidis, *Measurement and Detection of Radiation*. Hemisphere Publishing Corporation, 1983.
  - [62] "Sigma Periodic Table Browse." <https://www.nndc.bnl.gov/sigma/>.
  - [63] H. Klein and F. D. Brooks, "Scintillation detectors for fast neutrons," in *Proceedings of the Conference FNDA2006, International Workshop on Fast Neutron Detectors, University of Cape Town, South Africa*, 2006.
  - [64] "Photomultiplier Tubes (PMT)." <https://www.sense-pro.org/lll-sensors/pmt>.
  - [65] P. J. Sellin and J. Vaitkus, "New materials for radiation hard semiconductor detectors," *Nucl. Instrum. Methods Phys. Res. A*, vol. 557, no. 2, pp. 479–489, Feb. 2006.
  - [66] A. Owens and A. Peacock, "Compound semiconductor radiation detectors," *Nucl. Instrum. Methods Phys. Res. A*, vol. 531, no. 1–2, pp. 18–37, Sep. 2004.
  - [67] H. Spieler, *Semiconductor Detector Systems*. Oxford, New York: Oxford University Press, 2005.
  - [68] A. N. Caruso, "The physics of solid-state neutron detector materials and geometries," *Journal of Physics: Condensed Matter*, vol. 22, no. 44, p. 443201, Oct. 2010.
  - [69] M. B. Patil, *Basic electronic devices and circuits*. Delhi: PHI Learning, 2013.
  - [70] S. M. Sze and K. K. Ng, *Physics of Semiconductor Devices*, 3 edition. Hoboken, N.J: Wiley-Interscience, 2006.
  - [71] M. S. Tyagi, *Introduction to semiconductor materials and devices*. New York: Wiley, 1991.
  - [72] D. K. Schroder, *Semiconductor material and device characterization*, 3rd ed. [Piscataway, NJ] : Hoboken, N.J: IEEE Press ; Wiley, 2006.
-

- [73] J. H. Zhao, K. Sheng, and R. C. Lebron-Velilla, "Silicon Carbide Schottky Barrier Diode," *International Journal of High Speed Electronics and Systems*, vol. 15, no. 04, pp. 821–866, Dec. 2005.
- [74] S. K. Gupta, N. Pradhan, C. Shekhar, and J. Akhtar, "Design, Fabrication, and Characterization of Ni/4H-SiC (0001) Schottky Diodes Array Equipped With Field Plate and Floating Guard Ring Edge Termination Structures," *IEEE Transactions on Semiconductor Manufacturing*, vol. 25, no. 4, pp. 664–672, Nov. 2012.
- [75] S. K. Cheung and N. W. Cheung, "Extraction of Schottky diode parameters from forward current-voltage characteristics," *Applied Physics Letters*, vol. 49, no. 2, pp. 85–87, Jul. 1986.
- [76] C. Nyamhere, "Characterization of process and radiation induced defects in Si and Ge using conventional deep level transient spectroscopy (DLTS) and Laplace-DLTS," University of Pretoria, 2009.
- [77] T. Kimoto, N. Miyamoto, and H. Matsunami, "Performance limiting surface defects in SiC epitaxial p-n junction diodes," *IEEE Transactions on Electron Devices*, vol. 46, no. 3, pp. 471–477, Mar. 1999.
- [78] L. Liu, A. Liu, S. Bai, L. Lv, P. Jin, and X. Ouyang, "Radiation Resistance of Silicon Carbide Schottky Diode Detectors in D-T Fusion Neutron Detection," *Scientific Reports*, vol. 7, no. 1, Dec. 2017.
- [79] X. She, A. Q. Huang, O. Lucia, and B. Ozpineci, "Review of Silicon Carbide Power Devices and Their Applications," *IEEE Transactions on Industrial Electronics*, vol. 64, no. 10, pp. 8193–8205, Oct. 2017.
- [80] M. Mannan, "Defect Characterization of 4H-SiC by Deep Level Transient Spectroscopy (DLTS) and Influence of Defects on Device Performance," PhD Thesis, University of South Carolina, Columbia, 2005.
- [81] T. Dalibor *et al.*, "Deep Defect Centers in Silicon Carbide Monitored with Deep Level Transient Spectroscopy," *physica status solidi (a)*, vol. 162, no. 1, pp. 199–225, Jul. 1997.
- [82] C. Hemmingsson *et al.*, "Deep level defects in electron-irradiated 4H SiC epitaxial layers," *Journal of Applied Physics*, vol. 81, no. 9, pp. 6155–6159, May 1997.
- [83] N. T. Son *et al.*, "Negative- U System of Carbon Vacancy in 4 H -SiC," *Physical Review Letters*, vol. 109, no. 18, Oct. 2012.
- [84] K. Danno and T. Kimoto, "Deep level transient spectroscopy on as-grown and electron-irradiated p-type 4H-SiC epilayers," *Journal of Applied Physics*, vol. 101, no. 10, p. 103704, May 2007.
- [85] P. B. Klein *et al.*, "Lifetime-limiting defects in n- 4H-SiC epilayers," *Applied Physics Letters*, vol. 88, no. 5, p. 052110, Jan. 2006.



- 
- [86] J. P. Doyle, M. O. Aboelfotoh, B. G. Svensson, A. Schöner, and N. Nordell, "Characterization of electrically active deep level defects in 4H and 6H SiC," *Diamond and Related Materials*, vol. 6, no. 10, pp. 1388–1391, Aug. 1997.
- [87] A. A. Lebedev, "Radiation Resistance of SiC and Nuclear-Radiation Detectors Based on SiC Films," *Semiconductors*, vol. 38, no. 2, p. 125, 2004.
- [88] R. L. Harrison, C. Granja, and C. Leroy, "Introduction to Monte Carlo Simulation," presented at the Nuclear Physics Methods And Accelerators In Biology And Medicine: Fifth International Summer School on Nuclear Physics Methods and Accelerators in Biology and Medicine, Bratislava (Slovakia), 2010, pp. 17–21.
- [89] Consuelo Guardiola, "Novel silicon sensore for neutron detection," Universitat Autònoma de Barcelona, Barcelona, 2012.
- [90] A. M. Conway, T. F. Wang, N. Deo, C. L. Cheung, and R. J. Nikolic, "Numerical Simulations of Pillar Structured Solid State Thermal Neutron Detector: Efficiency and Gamma Discrimination," *IEEE Transactions on Nuclear Science*, vol. 56, no. 5, pp. 2802–2807, Oct. 2009.
- [91] S. Agostinelli *et al.*, "Geant4—a simulation toolkit," *Nucl. Instrum. Methods Phys. Res. A*, vol. 506, no. 3, pp. 250–303, Jul. 2003.
- [92] Geant4 Collaboration, "Book For Application Developers." 08-Dec-2017.
- [93] Geant4 Collaboration, "Use Cases - Reference Physics Lists | geant4.web.cern.ch." <https://geant4.web.cern.ch/node/302>.
- [94] J. Apostolakis *et al.*, "Geometry and physics of the Geant4 toolkit for high and medium energy applications," *Radiation Physics and Chemistry*, vol. 78, no. 10, pp. 859–873, Oct. 2009.
- [95] "Silvaco TCAD." <https://www.silvaco.com/products/tcad.html>.
- [96] "Atlas User Manual." Silvaco.
- [97] D. Stefanakis and K. Zekentes, "TCAD models of the temperature and doping dependence of the bandgap and low field carrier mobility in 4H-SiC," *Microelectronic Engineering*, vol. 116, pp. 65–71, Mar. 2014.
- [98] K. P. Schoen, J. M. Woodall, J. A. Cooper, and M. R. Melloch, "Design considerations and experimental analysis of high-voltage SiC Schottky barrier rectifiers," *IEEE Transactions on Electron Devices*, vol. 45, no. 7, pp. 1595–1604, Jul. 1998.
- [99] G. Lutz, *Semiconductor Radiation Detectors: Device Physics*. Berlin Heidelberg: Springer-Verlag, 2007.
- [100] M. Cortesi, R. Zboray, R. Adams, V. Dangendorf, and H.-M. Prasser, "Concept of a novel fast neutron imaging detector based on THGEM for fan-beam tomography applications," *Journal of Instrumentation*, vol. 7, no. 02, p. C02056, 2012.
-

- [101] D. S. McGregor and J. Kenneth Shultis, "Reporting detection efficiency for semiconductor neutron detectors: A need for a standard," *Nucl. Instrum. Methods Phys. Res. A*, vol. 632, no. 1, pp. 167–174, Mar. 2011.
- [102] D. S. McGregor, M. D. Hammig, Y.-H. Yang, H. K. Gersch, and R. T. Klann, "Design considerations for thin film coated semiconductor thermal neutron detectors—I: basics regarding alpha particle emitting neutron reactive films," *Nucl. Instrum. Methods Phys. Res. A*, vol. 500, no. 1–3, pp. 272–308, Mar. 2003.
- [103] K. Sedláčková, B. Zat'ko, A. Šagátová, M. Pavlovič, V. Nečas, and M. Stacho, "MCNPX Monte Carlo simulations of particle transport in SiC semiconductor detectors of fast neutrons," *Journal of Instrumentation*, vol. 9, no. 05, pp. C05016–C05016, May 2014.
- [104] "ISO 8529-1:2001(en), Reference neutron radiations — Part 1: Characteristics and methods of production." <https://www.iso.org/obp/ui/#iso:std:25666:en>.
- [105] F. H. Welch, "Lithium hydride: a space age shielding material," *Nuclear Engineering and Design*, vol. 26, no. 3, pp. 444–460, 1974.
- [106] A. Kargar, E. V. V. Loef, L. Cirignano, and K. S. Shah, "Organic semiconductors for fast-neutron detection," in *2011 IEEE Nuclear Science Symposium and Medical Imaging Conference (NSS/MIC)*, 2011, pp. 4545–4549.
- [107] M. Koželj and B. Cvikl, "On the Possibilities of Neutron Detection with Organic Semiconductor Structures," presented at the 21st International Conference Nuclear Energy for New Europe, Ljubljana, 2012.
- [108] "James Ziegler - SRIM & TRIM." <http://www.srim.org/>.
- [109] V. U. Mishra, "Study of silicon detectors," University of Mumbai, 2002.
- [110] P. Gandhiraj *et al.*, "Effect of Dead Layer on the Efficiency of Planar Semiconductor Neutron Detectors," *IETE Technical Review*, vol. 33, no. 1, pp. 45–49, Jan. 2016.
- [111] M. Wiets, M. Weinelt, and T. Fauster, "Electronic structure of SiC(0001) surfaces studied by two-photon photoemission," *Physical Review B*, vol. 68, no. 12, Sep. 2003.
- [112] Tesfaye Ayalew, "Dielectric Permittivity," *SiC Semiconductor Devices Technology, Modeling, and Simulation*. [Online]. Available: <http://www.iue.tuwien.ac.at/phd/ayalew/node69.html>.
- [113] A. V. Afanasyev *et al.*, "Temperature Dependence of Minority Carrier Lifetime in Epitaxially Grown p+-p-n+ 4H-SiC Drift Step Recovery Diodes," *Materials Science Forum*, vol. 821–823, pp. 632–635, 2015.
- [114] N. G. Wright, "4H-SiC power TCAD," in *IEE Colloquium on New Developments in Power Semiconductor Devices*, London, UK, 1996, vol. 1996, pp. 6–6.

- 
- [115] Tesfaye Ayalew, “3.3.2 Mobility Degradation due to Scattering.” [Online]. Available: <http://www.iue.tuwien.ac.at/phd/ayalew/node66.html>.
  - [116] D. C. Sheridan, G. Niu, J. N. Merrett, J. D. Cressler, C. Ellis, and C.-C. Tin, “Design and fabrication of planar guard ring termination for high-voltage SiC diodes,” *Solid-State Electronics*, vol. 44, no. 8, pp. 1367–1372, Aug. 2000.
  - [117] P. Hazdra, V. Záhlava, and J. Vobecký, “Point defects in 4H-SiC epilayers introduced by neutron irradiation,” *Nucl. Instrum. Methods Phys. Res. B*, vol. 327, pp. 124–127, May 2014.
  - [118] P. Hazdra, S. Popelka, and V. Záhlava, “The Influence of Neutron Irradiation on Electrical Characteristics of 4H-SiC Power Devices,” *Materials Science Forum*, vol. 821–823, pp. 785–788, Jun. 2015.
  - [119] A. Das and S. P. Duttagupta, “TCAD simulation for alpha-particle spectroscopy using SiC Schottky diode,” *Rad. Prot. Dos.*, vol. 167, no. 4, pp. 443, Dec. 2015.
  - [120] D. Planson, M. L. Locatelli, S. Ortolland, J. P. Chante, H. Mitlehner, and D. Stephani, “Periphery protection for silicon carbide devices: state of the art and simulation,” *Materials Science and Engineering: B*, vol. 46, no. 1–3, pp. 210–217, Apr. 1997.
  - [121] J.-Y. Kim *et al.*, “Effect of a Guard-Ring on the Leakage Current in a Si-PIN X-Ray Detector for a Single Photon Counting Sensor,” *IEICE Transactions on Electronics*, vol. E91-C, no. 5, pp. 703–707, May 2008.
  - [122] P. Vigneshwara Raja, C. V. S. Rao, and N. V. L. Narasimha Murty, “Numerical simulation of  $^{60}\text{Co}$ -gamma irradiation effects on electrical characteristics of n-type FZ silicon X-ray detectors,” *Nucl. Instrum. Methods Phys. Res. B*, vol. 379, pp. 23–27, Jul. 2016.
  - [123] F. Nava, E. Vittone, P. Vanni, P. G. Fuochi, and C. Lanzieri, “Radiation tolerance of epitaxial silicon carbide detectors for electrons and  $\gamma$ -rays,” *Nucl. Instrum. Methods Phys. Res. A*, vol. 514, no. 1–3, pp. 126–134, Nov. 2003.
  - [124] S. M. Kang, J. H. Ha, S. H. Park, H. S. Kim, S. D. Chun, and Y. K. Kim, “Study of the current–voltage characteristics of a SiC radiation detector irradiated by Co-60 gamma-rays,” *Nucl. Instrum. Methods Phys. Res. A*, vol. 579, no. 1, pp. 145–147, Aug. 2007.
  - [125] D. C. Sheridan, Gilyong Chung, S. Clark, and J. D. Cressler, “The effects of high-dose gamma irradiation on high-voltage 4H-SiC Schottky diodes and the SiC-SiO<sub>2</sub> interface,” *IEEE Transactions on Nuclear Science*, vol. 48, no. 6, pp. 2229–2232, Dec. 2001.
  - [126] E. Omotoso *et al.*, “The influence of high energy electron irradiation on the Schottky barrier height and the Richardson constant of Ni/4H-SiC Schottky diodes,” *Materials Science in Semiconductor Processing*, vol. 39, pp. 112–118, Nov. 2015.

\*\*\*\*\*